ABSTRACT

Investigation of Waterjet-Workpiece Interaction
By
Hung-Yuan Li

The objective of this research is to develop new knowledge related to the fundamental physical phenomena of waterjet machining of ductile materials, and to use this knowledge to construct a numerical analysis model. The resulting knowledge will enable enhancement of waterjet cutting efficiency.

Experimental study of fundamental mechanisms and the acquisition of the data detailing micro- and macro-scale phenomena which occur during the machining process is carried out. It is shown that the material damage mechanism associated with waterjet machining is erosion cavitation which initiates ultrasonic stress wave propagation in the workpiece. Fatigue, an important element in producing material erosion, is enhanced by this high frequency stress and reduces the material endurance limit. Experimental results validate the existence of these stress waves. The frequency is 3 MHz in the case studies.

The acquired information is used to construct a detailed description of the phenomena using finite element numerical modeling and continuum damage mechanics. Numerical results are in good agreement with the experimental results.

The resulting models may be used to optimize the jet generation and jet-workpiece interaction with particular focus on the improvement of nozzle design, integration of kinetic, chemical, and thermal energies for material shaping, and use of high speed percussive jets. With these new technologies and techniques, enhancement of material machining will be feasible.

INVESTIGATION OF WATERJET-WORKPIECE INTERACTION

By

Hung-Yuan Li

A Dissertation
Submitted to the Faculty of
New Jersey Institute of Technology
in Partial Fulfillment of the Requirements for the Degree of
Doctor of Philosophy
Mechanical and Industry Engineering Department
May 1992

APPROVAL PAGE

Investigation of Waterjet-Workpiece Interaction

by

Hung-Yuan Li

Dr. Ernest S. Geskin, Dissertation Advisor
Professor of Mechanical and Industrial Engineering, NJIT

Dr. Raj S. Sodhi, Committee Member
Professor of Mechanical and Industrial Engineering, NJIT

Dr. Avraham Harnoy, Committee Member
Associate Professor of Mechanical and Industrial Engineering, NJIT

Dr. Nouri Levy, Committee Member
Associate Professor of Mechanical and Industrial Engineering, NJIT

Dr. Eugene I. Gordon, Committee Member
Distinguished Professor of Electrical Engineering, NJIT

BIOGRAPHICAL SKETCH

Author: Hung-Yuan Li

Degree: Doctor of Philosophy in Mechanical Engineering

Date: May, 1992

Undergraduate and Graduate Education:

- Doctor of Philosophy,
  New Jersey Institute of Technology, Newark, NJ, May, 1992
- Master of Science in Mechanical Engineering,
  New Jersey Institute of Technology, Newark, NJ, May, 1988
- Bachelor of Science in Mechanical Engineering,
  National Taipei Institute of Technology, Taipei, Taiwan, May, 1983

Position held:

Teaching Assistant, Department of Mechanical Engineering
New Jersey Institute of Technology, Newark, New Jersey
January 1987 - May 1992

This thesis is dedicated to

My Dear Parents
And My Whole Family

ACKNOWLEDGEMENT

TABLE OF CONTENTS

LIST OF TABLES

LIST OF FIGURES

CHAPTER 1

INTRODUCTION

Shaping of material is a key part of almost any significant manufacturing process. Choice of materials, cost of manufacture, functionality, quality, and environment impact, all depend strongly on the ability to shape materials in a manufacturing environment.

During the last few decades, the principle breakthroughs in material processing were brought about by the development of casting, forming, and material deposition. Now the most important advance in the area of processing of structural, electronic, photonic and biological materials can be expected in material removal. Material removal is the only technology which orthogonalizes the control of material properties and geometry. Thus it simultaneously enables generation of components with special geometry, for example, ultra-precision parts with exotic shapes, as well as parts of materials with special properties.

Thermodynamic analysis of material removal technology and common sense indicate that the ideal tool for material shaping is a high energy beam, having infinitely small cross-section, precisely controlled depth and direction of penetration, and no effect on the generated subsurface. In addition, production of the beam should be relatively inexpensive and free of environmental impact. No such beam exists currently.

A high energy beam of considerable practical and theoretical interest, and close to meeting these requirements in several important attributes, is a narrow, cylindrical stream or jet of high velocity water, "the waterjet" or WJ. As compared to a laser, less subsurface damage is induced by WJ machining which removes material by plastic deformation or erosion. The machining mechanism of the laser is based on localized melting and vaporization or ablation, which causes significant subsurface modification. In other respects, however, WJ has significant practical limitations.

1

The principal physical shortcoming of WJ is the low efficiency of energy transfer between the jet and the workpiece. The beam energy of the WJ is comparable with that of a laser used for machining, however, the energy absorption by the workpiece and the cutting efficiency in the two cases are quite different. Because of insufficient energy transfer, WJ is only able to penetrate through comparatively soft materials.

The energy transfer is improved dramatically by the addition of abrasive particles into the water flow, producing the abrasive water jet. Efficient energy transfer between a moving particle and the workpiece enables the use of AWJ for the shaping of practically any technologically interesting material. However, AWJ is a mixture of water and particles and this imposes a number of important limitations and inconveniences on the technology. The energy transfer between the water flow and particles results in significant energy dissipation. The loss of available energy reduces the process efficiency. The rate of surface generation by AWJ is substantially lower than that of conventional or laser machining. The addition of the particles into the water jet increases the flow diameter which is larger than the diameter of the mixer (focusing tube). Larger flow diameter increases the material loss and the size of the generated kerf. The addition of abrasives to the water also introduces environmental problems. Because of these limitations, WJ and AWJ machining are utilized by industry usually only when other technologies do not assure a desired product specification, that is, they are the technology of last resort. Nevertheless, there is an increasing need for last resort solutions and AWJ has been adopted by industry and is becoming more widely used for shaping of hard-to-machine materials. It is being viewed increasingly as conventional rather than non-traditional technology. Improvement of the WJ and AWJ technology based on the research to be described, will result in the creation of a new conventional technology which will approach the ideal.

Basic understanding of the mechanism of the material destruction by the water stream is required for the improvement of this technology as well as the technology of

High Pressure WaterJet Systems can be operated at

a pressure of 1,000 psi at a flow of 5 gpm	a pressure of 1,000 psi at a flow of 1,000 gpm	a pressure of 2-20,000 psi at a flow of 2-20 gpm	a pressure of 10,000 psi at a flow of 10 - 50 gpm	a pressure of 30-60,000 psi at a flow of 1-2 gpm	a pressure of 30-100,000 psi at a flow of 10-20 gpm	a pressure up to 1,000,000 psi at a flow of varied volume
for use in	for use in	for use in	for use in	for use in	for use in	for use in
Car Wash & Cleaning	Coal Mining	Industrial Cleaning	Mining Cutting Crushing	Industrial Cutting & Machining	Water Cannon Rupture	Exotic Applications

With Potential Improvement by

Polymeric Additives	Cavitation Bubble Collapse	Abrasive Injection	Hydromechanical Cutting

Figure 1.1 Classification of Continuous Fluid Jet Applications Base On Pressure and Flow

abrasive waterjet (AWJ) machining.

The applications of high pressure, pure WJ technology have two different directions. The first application is in the manufacturing process. The success of this technology has been traced back to the 1970's, when the jet was pressurized to 20-30 ksi and used in cutting soft material. Working pressure of WJ at a maximum of 50 ksi has proved to be able to cut a variety of relatively soft materials at a high cutting rate. WJ has also been found efficient in the applications of cleaning, mining [1,2] and cutting of woods or textile products [3].

In the beginning of the 1980's, it was found that the addition of abrasive particles to the jet will increase the cutting capability so that almost any type of material can be processed [4]. The jet developed through the entraining of the solid particles is called an abrasive water jet, AWJ. During this process, abrasive particles are injected into the down stream of a pure water jet, which guides the particles into a mixing chamber and integrates them with a pure WJ stream. In the mixing chamber, particles are accelerated and the kinetic energy of the jet is increased. The increasing of the energy is contributed to the high cutting rate [5,6,7].

A number of research studies have been performed in order to find new applications of WJ cutting, to determine the WJ properties, and to improve the performance of WJ. Computer Integrated Manufacturing, CIM, technology has extended the areas and applications of WJ cutting[8]. With the assistance of CIM, materials consumption can be reduced and a more accurate shape can be achieved. A general classification of continuous fluid jet applications is shown in Figure 1.1 [9].

1.1 Description of WJ System

In considering of the system layout and characteristic functions, there are basically three major components in a WJ cutting system, the water preparation unit, the water distribution

unit, and the work station. The schematic of the system is shown in Fig, 1.2.

1.1.1 Preparation Unit

The major functions of this unit are to supply continuous pure water and pressurize the water to required pressure value. This unit includes booster pump, filter, water softener, prime mover, intensifier, accumulator and control valves.

To ensure a continuous supply of water into high pressure intensifier, the booster pump serves to give water an initial pressure up to 180 psi. The water has to be free from contamination, such as iron and calcium dissolved solids, which will damage the system components and the orifice in the work station unit. This is done by the low pressure filter and softener.

A hydraulic driven oil intensifier is used to develop the water pressure up to 60 ksi from the booster pump. There are two circuits in this component. An oil circuit is a closed loop while a water circuit is an open one. The oil pressure developed by a rotary pump is used to drive this intensifier. This intensifier is a double-acting reciprocating compressor. The oil circuit and water circuits are separated to prevent contamination.

The water is then discharged from the intensifier to an accumulator where the pressure can get stablized, since an estimated value of water compressibility of 12% at 55000 psi suggests an non-uniform discharge from the intensifier. Pressure gauges are mounted on a rupture disk to monitor the oil and water pressure separately.

1.1.2 High Pressure Water Distribution Unit

The high pressure water discharged from the accumulator is carried away to the work station through this unit which includes a series of pipes, joints and fittings. The number of joints, elbows, and the length of the pipe determines the pressure drop on this unit. The main advantage of this unit is to centralize the water preparation unit with respect to one or more work stations.
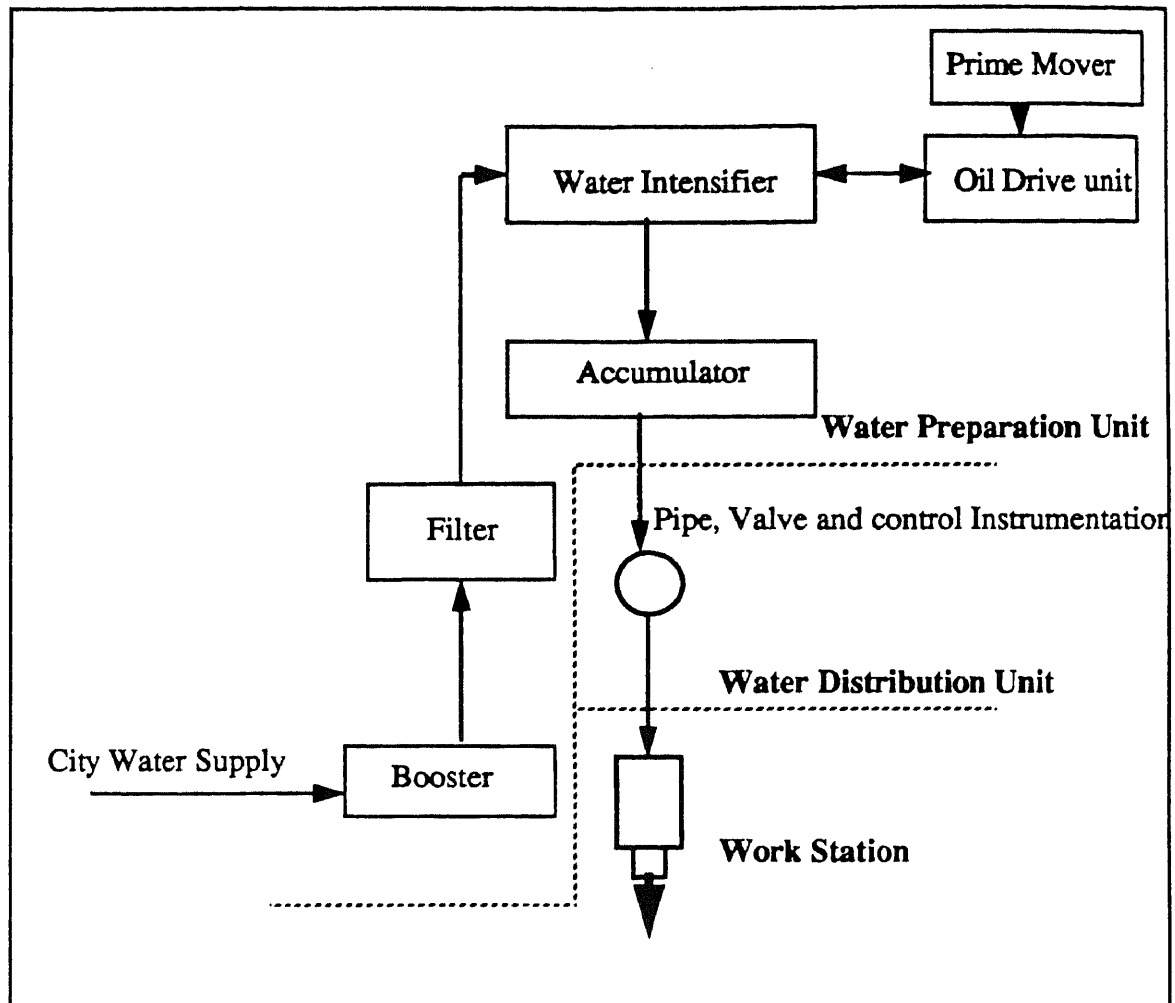
Figure 1.2 The system schematic of Water jet System.

1.1.3 Work Station

This unit is composed of a variety of components and serves as the actual cutting operation plateform. Depending on the applications, several major components can be included:

Nozzle assembly: The huge pressure head of water is converted to kinetic energy in this component. The complexity of this assembly mainly depends on the application of WJ or AWJ.

For WJ, the high pressure water first passes through a small diameter sapphire

nozzle diameter and is accelerated up to 700 m/sec. This high velocity WJ impinges on material and creates damage on the surface.

In the application of AWJ, abrasive particles enter the nozzle assembly and mix with liquid flow in the mixing chamber. The quality of the mixing is dependent on the entrance method and entrance geometry. A single port and side entrance model is most commonly used.

Work place and traverse mechanism: In the case of material shaping, either the jet or the work piece has to be movable. There are several ways to enable this movement:

i. Robots.
ii. CNC controlled X-Y positioning table.
iii. Manual movement mechanism.
iv. On line production unit.

The accuracy of the material shaping is mainly dependent on the movement mechanism.

1.2 Types of Water Jet

There are two types of pure WJ which can be generated according to its loading characteristics.

1.2.1 Continuous WJ

A constant water pressure prior to expansion is supplied. Current pumping technology limits the pressure to 55-60 ksi. A jet at this pressure will cut most rocks and soft materials but barely damage non-permeable materials, such as metals.

At the beginning of the interaction between jet and solid surface, the pressure rises to a maximum peak pressure and lasts for a very short period. This maximum pressure peak may be calculated by the water hammer effect. After this pressure peak, a stagnation pressure is applied on material surface and is a typical loading for the interaction on the

material surface.

A general theory of continuous WJ interaction on a material surface was given by Hashish [11]. In this work, a control volume of WJ-Workpiece interaction was assumed to determine the hydrodynamic forces acting on the solid boundary and a Bingham material model was applied to describe the stress-strain relationship in the time-dependent material model. However, this work is more applicable to brittle materials such as rocks than ductile materials since the threshold pressure of brittle material is mostly constant while the pressure is affected by the plastic deformation in ductile materials.

Crow [12] assumed that grains of rock materials protruding from the surface being swept by the jet would be subjected to a shear stress by the jet flow. This model appears to predict accurately the cutting behavior of WJ in a limited series of tests in Wilkenson Sandstone. Unfortunately, more extensive testing in other rock types has shown that this model is inadequate to predict generally the phenomenon of rocks erosion which was the reason that the calculated value of shear stress acting on a grain is far below the shear strength of the rocks.

Rehbinder [13,14] essentially ignored the shear stress exerted on protruding grains by the flow of water over the rock surface. Instead, the forces acting on individual rock grains by the water flow through pores and grain boundaries were examined. This model suggested that the material threshold pressure was approximately equal to the microscale tensile strength of rocks and the erosion resistance as proportional to the inverse of the average grain diameter and to the slenderness ratio of the pores in the rock.

Louis [15] attempted to relate the crack propagation of comparatively hard materials, granite and diabase, with energy release rate in the course of the fracture formation.

Przyklenk [16] studied the response of a ductile material, aluminum, under pure water jet impingement. A program, ASKA, has been developed based on reciprocating

algorithm which simulates interaction time by the loop of load steps. This model inherently ignored the material failure mechanism and only took into account the material deformation.

Curnier and Ridah [17] developed a robust WJ cutting model by the coupling of a numerical model of a small length of water jet with a continuum mechanics model. Material failure model was assumed to be cavitation erosion process. Unfortunately this model has only been applied to the process duration of 0.5 ms $(10^{-3}$second) and thus the jet length is limited to 0.1 cm.

1.2.2 Discontinuous Jet

These jets apply an impact, impulsive, force on the target and can be produced by culmination, pressure extrusion or percussive modulation. The loading on material can be characterized by a continuous following of the formation of a peak pressure which lasts for an extremely short time and a steady state pressure as a result of the water volume which also lasts only for a very short time. The maximum pressure generated by this impacting process is higher than that generated by a continuous jet. Consequently the destructive ability of these jets potentially is greater.

Vijay [18] experimentally investigated the characteristics of cavitating water jets by photography and the patterns of erosion caused by the jet on different materials such as aluminum, granite and lead. A mathematical model was also developed to correlate the material loss rate with the cavitation number.

Yamaguchi [19] empirically studied the quantitative relation of material loss rate and cavitating jet interaction period. An optimum value of stand-off distance which will maximize material loss depends on the upstream pressure and the down stream pressure of the nozzle, configuration of test cell and test liquid.

Between these two extreme types of jet is a whole spectrum of jets. These mixing loading jets can be obtained by a continuous jet containing cavitation bubbles which

explode near the working surface and droplets which impinge on the material surface. These bubbles or droplets can be a result of turbulences in the jet and the friction between the formerly continuous jet and the ambience. There are several physical models to explain the phenomenon of bubble and droplet generation [9,10].

1.3 Bubble Nucleation and Growth Model

There are two major nucleation models, both of which apply to some extent in all cases, but their significance differs between applications. There are the stationary crevice model and the entrained nuclei model [20].

In the stationary crevice model, stationary nuclei are generally assumed to be harbored in microcrevices of various shapes in an adjacent wall [21], while traveling nuclei are assumed entrained with the main stream. Entrained nuclei are primarily pertinent for cavitation. Cavitation can also be initiated from stationary nuclei in crevices in the guiding wall at the minimum pressure region.

In most simple terms [20], the bubble will be generated if

$$P_v - P_L = \frac{2\sigma}{R} \qquad (1.1)$$

where the subscript v: vapor or gas.

the subscript L: liquid.

σ: the surface tension

R: radius of bubbles.

Beyond the effect of surface tension, air or gas in the flow stream will also initiate bubble nucleation.

1.4 Material Response under Impact

An interdiscipline science dealing with the change of material state during the interaction of any moving or stable material surface is called tribology. This change may arise from many aspects of phenomena such as physical, chemical, mechanical or metallic. Impact may also be cataloged in the tribology as its characteristic performance such as sliding interaction and contact in short duration when projectiles reach target material. This phenomenon has been traditionally associated with wear.

Wear is defined as the removing or displacing of material mass or volume when the material is under a repeated loading of mechanical contact with another body or bodies. Generally, there are four types of wear mechanism [22].

1.4.1 Adhesion Wear

Adhesion may be explained by the molecular attraction existing between two relative moving materials [22]. This process involves adhesion, plastic deformation and fracture. It is also known as sliding wear. The energy of adhesion is dependent on the structure of the materials; identical materials with matching lattice structure can readily weld together if no contamination exists on the interface.

When two surfaces slide on one another, their topographic features allow only the contact of asperity peaks. These junctures (Figure 1.3), assumed to be the result of plastic deformation, represent the real area of contact and may be a very small portion of the gross contact area. When adhesive wear forms, materials are removed from the junctures. Holm [23] derived the volume of wear, W, for a slider as [23]:

$$W = \frac{ZPX}{p} \qquad (1.2)$$

where *P*: Total normal contact force.

X: Sliding distance.

Z: The number of atomic layer removed.

p: Material hardness.

Junctures: Real area
of contact where
plastic deformation
may occur.

Hard
surface

Soft Surface   Gross Contact Area
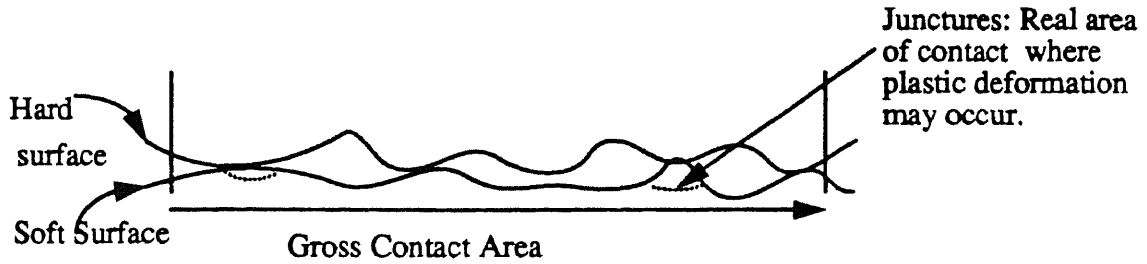
Figure 1.3 The real contact area (junctures) and apparent contact area (gross) of two

surfaces.

Archard [24] adhesive wear law was based on Equation (1.2) and assumed the

fracture of material as the result of adhesive force of two materials is stronger than the

cohesive force. A nondimensional constant, *K*, is defined as:

$$K = \frac{3pW}{Px} \qquad (1.3)$$

The value of *K* has been found to be dependent on the pressure applied and

materials. As the applied pressure gets higher, this constant is larger. Adhesion between

two similar materials also possess a larger *K* value.

1.4.2 Abrasion Wear

Abrasive wear is defined as the displacement of material from a surface by contact with

hard projectiles on a mating surface, or with hard particles, that are moving relative to the

wearing surface [22]. It acts independently of the adhesive wear. However, these two

wears are additive.

There are tree types of abrasion wear commonly defined:

Gouging abrasion involves removal of relatively coarse particles from the steel wearing surface and is similar to the removal of metal by machining or grinding with a coarse grinding wheel.

High stress grinding abrasion wear involves removal of relatively fine particles from the the wearing surfaces. The mechanism of the damage may be formed by the microscopic gouging or by a combination of local plastic flow and microcracking.

Low stress scratching abrasive wear occurs by very light rubbing contact from sharp abrasive particles. The stresses are mainly due to the velocity and are normally insufficient to cause damage.

When hard particles are involved in abrasive wear, they may be trapped between sliding surfaces and abrade one or both of the materials (Figure 1.4). A simple abrasive wear model has been developed by Rabinowicz and the amount of material abraded can be calculated as

$$W = \frac{K_{abr}PX}{3p} \qquad (1.4)$$

Unlike the K defined in adhesive wear which has a smooth increase, K_{abr} undergoes a sharp step-like change when two material hardnesses become alike. A typical plot of K_{abr} is given in Figure 1.5 [23].
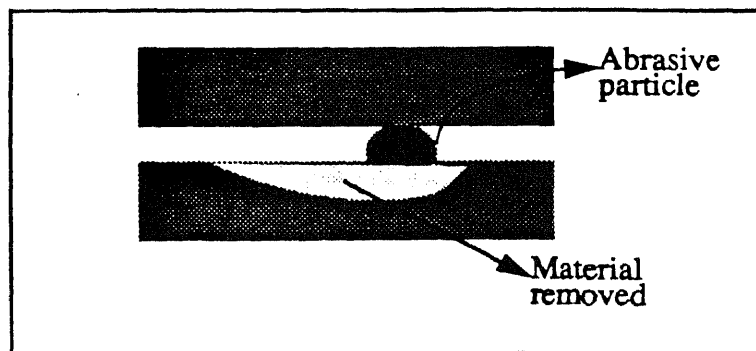
Figure 1.4 Abrasive Wear Mode
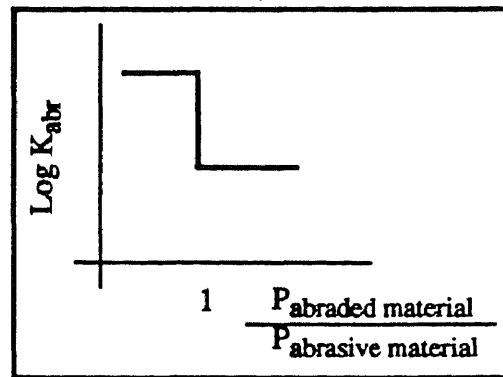
Figure 1.5 Typical K_{abr} value

Depend on the hardness ratio.

1.4.3 Surface Fatigue.

Surface fatigue is a special type of surface damage caused by cyclic contact loads, at relatively low stresses [22]. It is generally observed in a rolling-contact system. Rolling elements, subjected to repetitive cycles of a hertz-type contact stress, develop subsurface cracks which eventually lead to a spalling-type failure. This failure mechanism was found to be highly stress-dependent by Lundgren and Palmgren who empirically established a formula [25] as:

$$P^3N = constant \qquad (1.5)$$

Where N: the number of cycles to failure

P: Load

An intensive study of surface fatigue phenomena has been carried by Bayer and Ku [26]. A zero wear stage theory has been developed which describes two stages in the wear life of a sliding constant.

1.4.4 Erosion

Erosion is a destruction process of metals or other materials by the abrasive action of moving particles which may be solid particles or liquid particle [22].

If solid particles are present, the common mechanisms are abrasion mostly associated with the shallow angle of attack and the fracturing of the surface layer following work hardening and brittle cracking. An important dependence of the erosion upon the angle of attack and the hardness of the attacked surface was found by many researchers [27,28,29]. It was concluded that the erosion of soft material was found to peak at a flat angle, while hard steels wore the most under normal impingement.

Finnie introduced his erosion cutting theory in 1958 [27]. This theory assumes that a hard, angular particle, impinging upon a smooth surface at an angle of attack α, will cut into the surface, much like a sharp tool. The ductility of the material means its ability to flow plastically during the cutting process. This model successfully explained many aspects of the erosion of ductile materials under the action of streams of more or less angular particles. The volume of materials removed can be calculated from the view of energy balance. A schematic of Finnie abrasive model is shown in Figure 1.6.

The final result of this model expressing the erosion on ductile material can be approached as in Equation (1.6) and Equation (1.7)
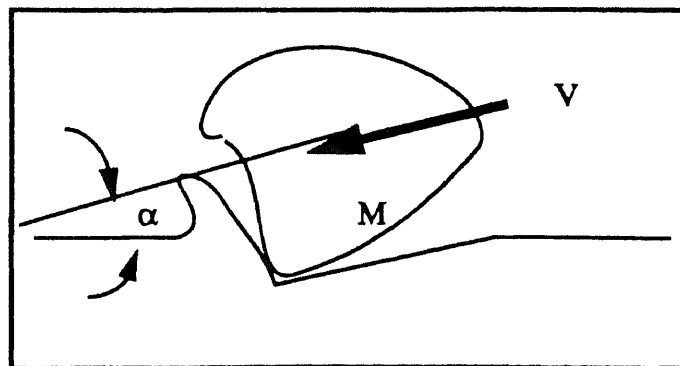
Figure 1.6 Finnie erosion model.

$$W = \frac{MV^2}{2}\frac{1}{p}(\frac{\sin 2\alpha - 3\sin \alpha^2}{2}) \qquad 0 < \alpha < \alpha_0 \qquad (1.6)$$

and

$$W = \frac{MV^2}{2}\frac{1}{p}(\frac{\cos \alpha^2}{6}) \qquad \alpha_0 < \alpha < 90 \qquad (1.7)$$

where p: the flow pressure acting on the material surface horizontally.

α: The attack angle.

α_0: A critical attack angle which will not damage material.

This model is in good agreement with the experimental results of annealed steel, SAE 1020, under copper abrasive particles impact.

The distinct erosive characteristics of ductile and brittle erosion are most pronounced in the W (α) curves. Bitter assumes that the real material can possess both behaviours and the total erosion would be the superposed effect [30,31]. This model is based on the computation of plastic energy dissipation from the impact parameters of a single erosive particle and material loss can be calculated by

$$W = \frac{1}{2}\frac{M (V\sin \alpha - K)^2}{\varepsilon} \qquad (1.8)$$

Where K : a constant for a given eroded surface materials characterized by σ_y.

ε : energy needed to remove an unit volume of material from the body surface.

Head derives a theoretical relationship based on Meyer's hardness law to describe

the elastic-plastic impact by rigid sphere on a flat surface. This model neglects the stress wave effect and analyzes the fracture process from a hypothesis assuming that the work done by the impact is totally contributed to the fracture energy.

A liquid or gaseous medium without the presence of another phase in the medium may also cause the damage. The stress created in the material may create pits on the surface, cracks on the surface and subsurface, mass loss of material and loss of optical transparency in transparent material. This damage can weaken the material significantly and render the components exposed to liquid impingement inefficient or even useless. The only criterion of this destruction process is the imposition on the surface of shear or normal stresses of sufficient magnitude to cause the material failure, either through single blow or fatigue-type effect.

Material response subjected to the impact of single droplet can provide considerable insight into the phenomena occurring at the liquid-solid interface and illuminate the process and mechanism of erosion. This process has been studied by numerous investigators experimentally. The results of these study cannot be applied directly to water jet impact which is a continuous high speed impingement.

A rotating arm test (Figure 1.7) has been used for the experimental study of pressure distribution at low velocity water jet impact [32]. This device consists of a rotating wheel, to the periphery of which the specimens to be eroded are attached. Since the highest velocity which can be attained is about 225 m/sec, it is hard to explain the rapid erosion of some of the hardened materials tested without the contribution of local cavitation as well as liquid impact.

A ballistic test (Figure 1.8) was carried out to simulate the high speed single droplet impact [33]. Water is sealed off in a chamber by a plug; a bullet fired against the latter forces a jet of water out of a narrow orifice, against the target specimen. The shape of the jet leaving the orifice depends on the water surface inside the chamber prior to shooting. A velocity of up to 2000 m/sec can be reached.

Both of these experiments present three different material loss rates with respect to the exposure time (Figure 1.9). In the first region, the so called "incubation region", material loss is not significant. After this period the rate of the weight loss is nearly constant and weight loss varies almost nearly with time. This period is called "the steady rate region". Past this region the relationship between the weight loss and the exposure time becomes more complex and is referred to "the final region".

The continuous water jet impact has been carried out by many different combinations of experimental parameters. Murai studied the relation between Aluminum mass loss and stand-off distance and claimed that two peaks existed [34]. The first peak of weight loss is generated through fracture of the circumference and/or the bottom of the penetrated pits by the stagnation pressure of the jet core. With increase of exposure time, the jet core begins to penetrate into the specimen more deeply and the stagnation pressure in the eroded pits becomes more effective in fracturing the circumference and the bottom of the hole.

Similar results to multiple droplets in a continuous jet impact have been found by Yamaguchi and Shimizu [19]. An aluminum plate is tested and tap water is fired through a 40 mm diameter nozzle in a 9.9 Mpa pressurized state.

A more complete experiment has been carried out by Erdmann [15]. Four different jet formations impinged on brittle material have been studied and the results are compatible with those of Murai and Yamaguchi.

A more complete experiment has been carried out by Erdmann [15]. Four different jet formations impinged on brittle material have been studied and the results are compatible with those of Murai and Yamaguchi.

Analytically, the dynamics of liquid drop impact (Figure 1.10) between a compressible water droplet and solid has been investigated by Huang [35], Heymann [36], Field [37] and Engle [38], etc. In the initial stage of impact, the sudden deceleration of
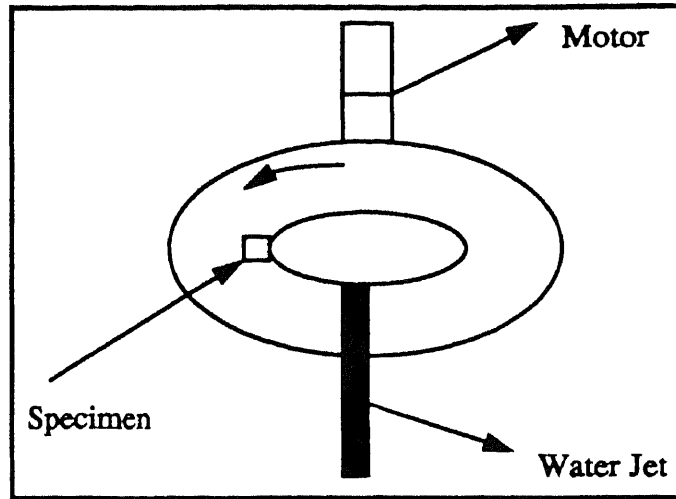
Figure 1.7 Rotating wheel test device.
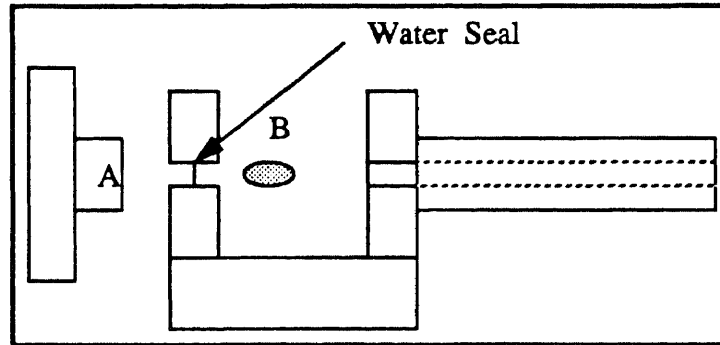
Figure 1.8 Ballistic water gun device. A: specimen; B: bullet.

the drop will establish a large pressure shock wave, often known as water hammer pressure. This pressure can be affected by the curvature of the droplet front end. Engle gives the equation as [38]:

$$P = \frac{r\rho CV}{2} \qquad (1.9)$$

where r is varied with different droplet front end and velocity of impact.

This water hammer effect will generate a high magnitude stress, which is generally believed to be the primary fracture mechanism of material.
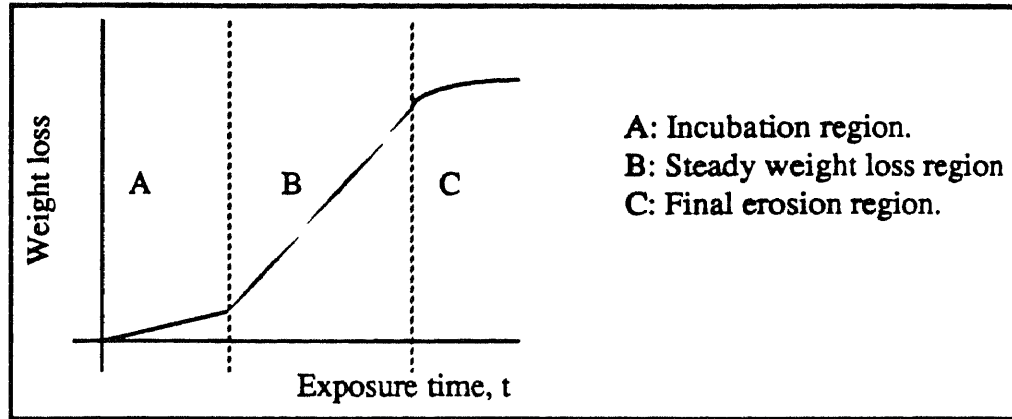
Figure 1.9 Typical liquid drop erosion mass loss history.
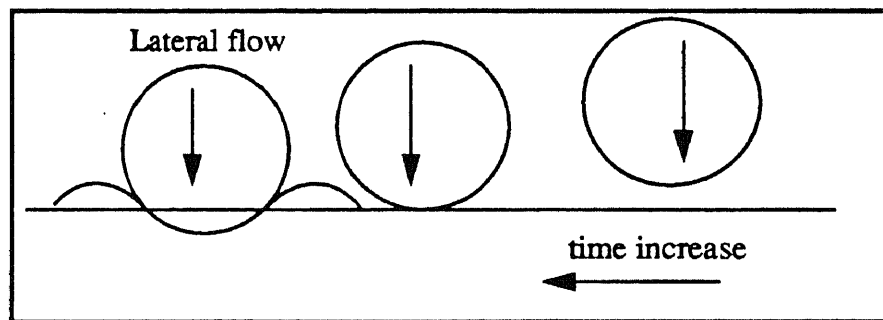
Figure 1.10 Impact of a liquid drop on an elastic surface.

CHAPTER 2

OBJECTIVES

Shaping of materials is a key part of almost any significant manufacturing process. The choice of materials, cost of manufacture, and environment impact, all depend on the ability to shape materials in a manufacturing environment. The shaping techniques that we focus on involve the use of water jet, WJ, and abrasive water jet, AWJ.

Water is a convenient and environmental medium, but WJ is not normally used in the manufacturing process, except on soft materials, because it cuts relatively slowly and inconveniently. AWJ is in fairly common use because it is capable of accurately shaping a wide range of materials, and producing minimal damage to the remaining material.

The long term goal of this work is to enhance the cutting efficiency of WJ to such an extent, by a factor of at least ten, that it becomes a desirable, application extending, alternative to AWJ. In pursuing this, a complete knowledge of WJ-workpiece interaction is needed.

The objective of this study is to determine the details of the ductile material damage in the course of pure water jet impingement. Phenomenological descriptions of the damage mechanisms are sought. These descriptions are needed to show the damage mechanism on ductile material in the course of WJ impingement. Furthermore, the damage growth of this process is simulated to predict the depth of cut and cavity formation.

The information gained will enable a full understanding of the water jet anatomy and of the material damage process under water jet interaction; also an enhancement of WJ cutting efficiency should be feasible.

CHAPTER 3

MEASUREMENT OF MOMENTUM IN THE COURSE OF WJ-WORKPIECE INTERACTION

3.1 Introduction

In the study of the mechanism of WJ cutting of ductile material, a study of the momentum developed in the impingement zone can provide substantial information of this process. Effects of the process conditions enable us to estimate the optimal range of process variables. Because of this, the magnitude of the momentum developed in the course of the WJ-workpiece interaction will enable us to understand the mechanism of WJ formation and optimize the control variables. Therefore, the objective of this study is to investigate the mechanical loading on material surface in the impingement zone.

Physically and mathematically, the momentum existing in the WJ impingement zone includes the force developed in the contact zone and pressure distribution generated in the interface. To measure the action of jet interaction, two different methods can be applied [39].

●Direct method:

The aim of the direct method is to describe the loading of a material by an electric signal. WJ loading normally consists of static and dynamic parts. However, static loading of WJ will not be sufficient to describe the loading condition on material surface because of the turbulent properties of the jet.

The dynamic part of the loading can be measured by an accelerometer, an acoustic transducer, or a force transducer. The transducer may work by piezoelectric material or by strain gauges.
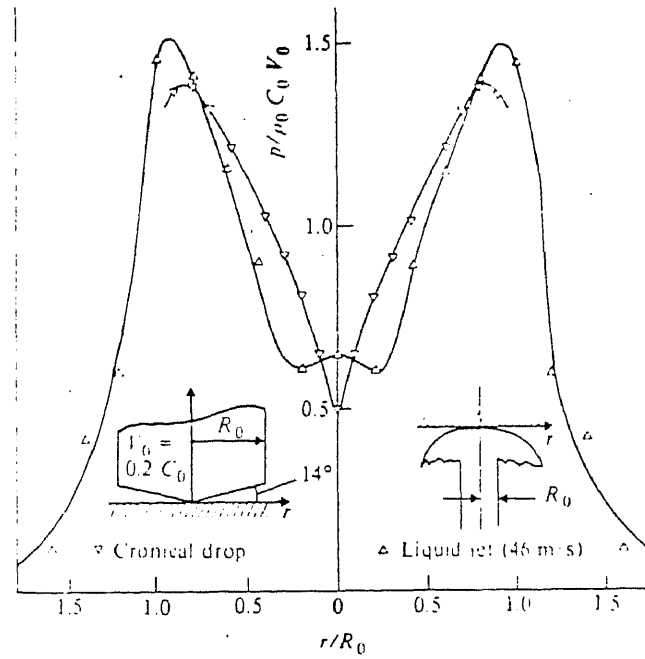
Figure 3.1. Maximum direct pressure distribution from Johnson and Vicker.
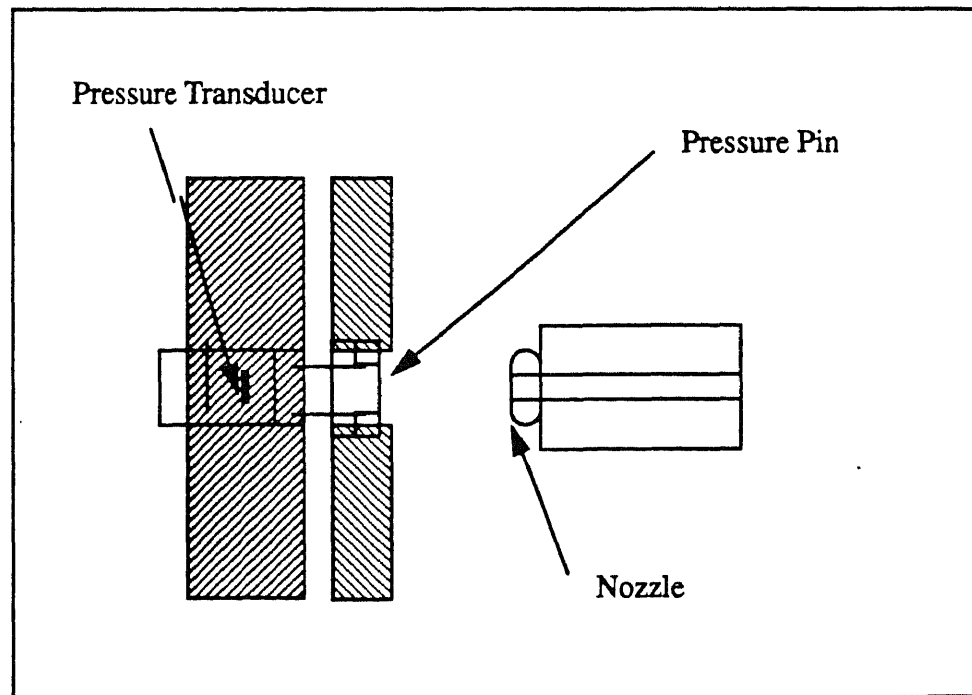
Figure 3.2 Experimental setup of Smith and Kinslow.

Between the loading and transducer, a translation unit is needed. This translation unit must be strong enough to protect the transducer from damage by the jet and adequately represent the jet impingement action.

Johnson [40] and Rochester [41] studied the impact pressure generated by a 5 cm jet at the velocity of 46 m/sec. Their results show that the maximum pressure occurred near the edge of the jet and is axisymmetric at the center which has the lowest pressure value, and the resulting material shape follows this pressure distribution.

Leach and Walker [42] studied the active loading of a 1 mm diameter jet. The pressure of the jet is controlled at 600 atm and 5000 atm, and the nozzle (sapphire) exit diameter is 1 mm. A steel plate containing a hole as 0.3 mm diameter is used as a translation unit. Strain gauges and a multichannel pen recorder are used as transducer and output device respectively. The results are verified by photography with a spark light 0.5×10^{-6} second. The translation unit can be moved in three dimensions to achieve a maximum pressure. Their results are compatible with theoretrical analysis explained in the form

$$P - P_0 = 0.5 \times \rho \times V^2 \times f(\frac{r}{R}) \qquad (3.1)$$

Smith and Kinsllow [33] used a 2.38 mm diameter jet with 6.6 mm head diameter in the speed of 64 m/s. The experimental setup includes a piezoelectric pressure transducer, a target plate with a pin inserted into a hole (Figure 3.2). The small end of the pin is 0.99 mm diameter, and the top of the pin is 3.8 mm. In order to prevent damage on the top of the pin, it has been heat treated. The output is obtained from an oscilloscope. The plate can also be moved in three dimensions in order to get maximum pressure value. However, the verification has never been presented in their report. The reported results show a constant relation between the (r/R) ratio and pressure of the jet as
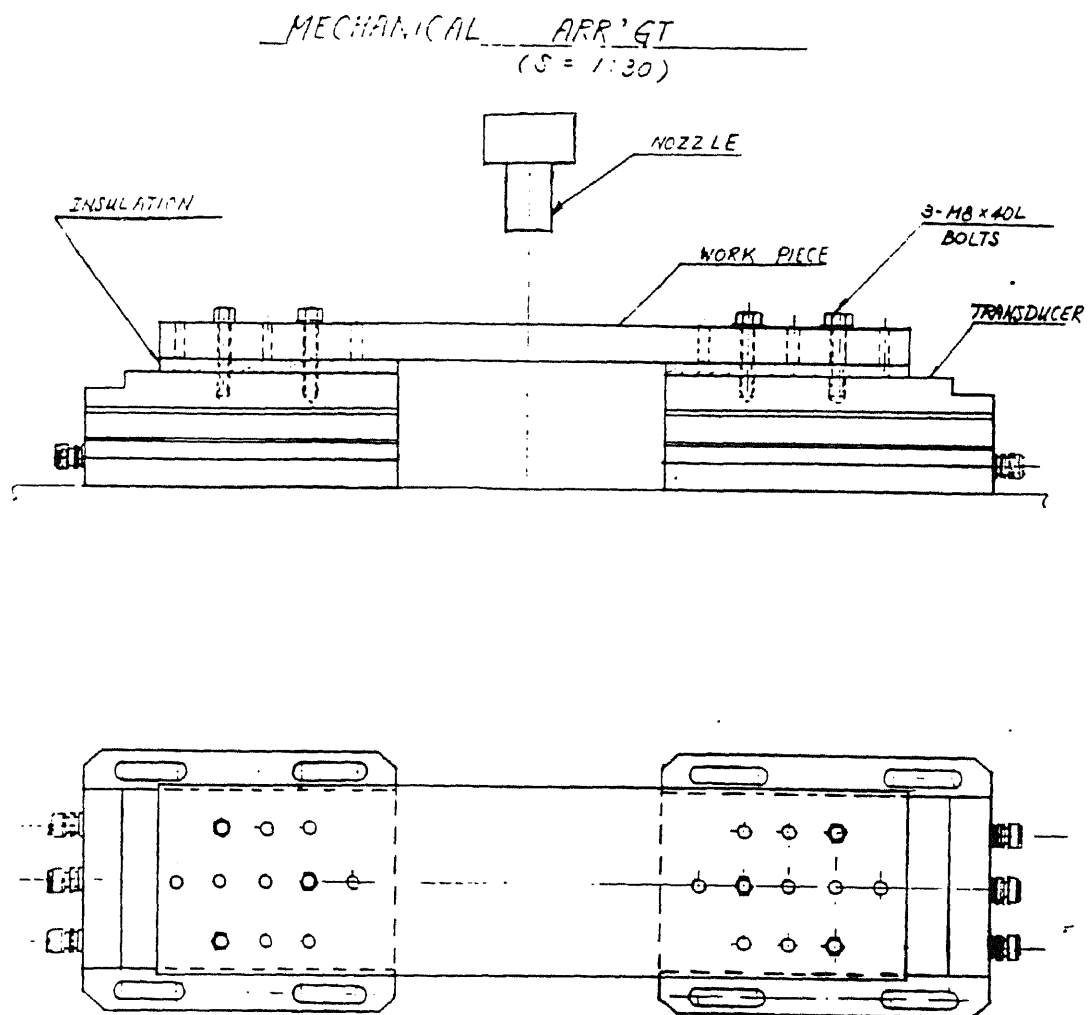
Figure 3.3 Experimental Setup.
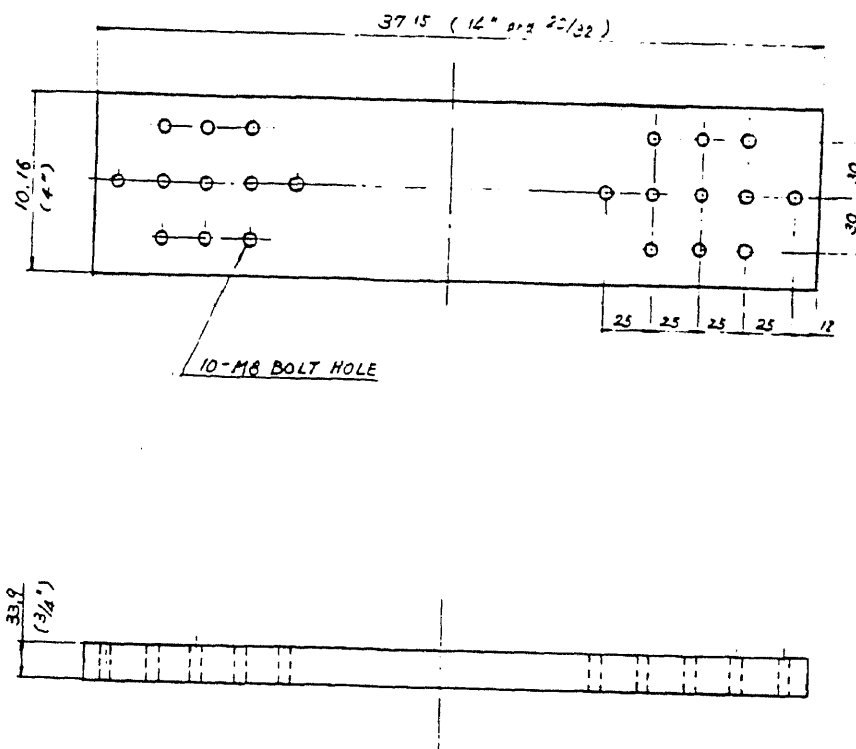
Figure 3.4. Force Translation Unit.

$$P = \beta \times \rho \times V \times C \times e^{1.22 \left(\frac{r}{R}\right)^2} \qquad (3.2)$$

Considering the dynamic variation of the jet, no reported measurement techniques can be found to be accurate both in frequency and magnitude.

●Indirect method:

The indirect method is to describe the loading of the jet by its action on model material.

This model material must be sensitive to different loading by the jet. Its behaviour must be homogeneous and reproducible, and the most important factors are the cost of the materials and availability.

Because of these demands metallic materials are most often used.

To describe the loading resulting from the jet by the reaction of the material, microscopical and macroscopic aspects have to be studied. By microscopical observations, information whether the jet loads the material statically or dynamically can be obtained. Macroscopic study can provide general information on the jet action on the material surface. The study of microscopic observation is described in Chapter 5 wheras the macroscopic study is presented in Chapter 4.

3.2 Objective

In this direct measuring experiment, intensive study of both abrasive and non-abrasive water jet cutting has been carried out. The objective of this study is to provide the information of jet action while impinged on the material surface and to determine the process variables effects on this action. It will also enable us to develop a new experimental procedure and to use this procedure for the evaluation of some basic characteristics of the WJ cutting

technology.

3.3 Experimental Apparatus and Procedures

3.3.1 Experimental Apparatus

In this experiment, great difficulties are met since the creation of a continuous liquid jet of supersonic velocity of diameter of the order of 1 mm requires a large delivery rate from the apparatus yet it seems so difficult to probe the interior of a jet of such a small diameter since the introduction of any extraneous object such as a measuring instrument will introduce a large disturbance. Therefore, an aluminum plate was used as translation unit to transport the momentum from the jet. A piezo-electric force transducer to measure the momentum distribution along the axis of the jet can provide frequency and measure dynamicity with accepted accuracy.

The sketch of the transducers setup is shown in Figure 3.3. Two identical three- components force measurement platforms were used in this study. Each multi-components transducer is assembled by stacked quartz disks loaded mechanically in a series with electrode interlayers. The force to be measured acts on the workpiece so each quartz disk will generate a certain amount of charges in the same direction as the application at that time. In our study, two Kistler three-components force measurement platforms 9257A were used. The signal was amplified in a charge amplifier which was used as a classic electrometer to enable charge alteration on quartz transducers to be measured. Each component of the charge amplifier has its own sensitivity switch and measuring range scale switch according to each measuring axis. In this study, Kistler three components charge amplifier Model# 5007 was used.

A steel plate, 14" X 4" X 0.75", shown in Figure 3.4, drilled 20 of 0.0375 inch diameter holes which was used to fix the steel plate and the insulation wood

plate on the transducers. The bottom surface of the work piece is machined flat to prevent the possible vibration.

A Fluke Model 8101A digital multimeter and a Gould two-channel recorder were used. These two are connected in parallel to charge amplifier. For future study, a digital oscilloscope connected with a computer to record the signal from the charge amplifier is recommended.

3.3.2 Experimental Procedures

The jet emanating from the combination of one of five different diameter sapphires (4/1000 inch, 5/1000 inch, 7/1000 inch, 10/1000 inch, and 14/1000 inch) and one of three different diameter carbide tubes (30/1000 inch, 43/1000 inch, and 63/1000 inch) which will be called nozzle assembly, impinges on the work piece. The nozzle is kept exactly vertical to the target plate. The plate is fixed on the transducers by six axis-symmetric position screws. Two transducers are connected to the charge amplifier in parallel.

There are three parts of this study:

1). Pure water jet force measurement.

2). Abrasive jet force measurement.

3). Jet force variation as a function of abrasive consumption.

In the first part, the forces from the interaction of jet and work piece are measured under different sapphires and carbide tubes combination with the stand-off distance changes. The measuring distance is 2.54 mm, 12.7 mm, 25.4 mm, 50.8 mm, and 76.2 mm. Sapphire and carbide tube measuring size are the same as stated before. The function can be expressed as

$$Force = f(d1, d2, Z) \qquad (3.1)$$

Where *d1*: sapphire diameter.

     d2: carbide tube diameter.

     Z: stand-off distance

In the second part, two other variables, abrasive size and abrasive flow rate, have to be considered except the sapphire size, carbide tube size, and stand-off distance. Four kinds of abrasive size, 50 HP, 80 HP, 120 HP, and 220 HP, and two flow rate grid were under inspection. The function can be expressed as

$$Force = f(d1, d2, Z, S, M) \qquad (3.2)$$

Where *S*: Abrasive mesh size

     M : Abrasive particles flow rate.

The third part will investigate the force variation according to the abrasive consumption. The abrasive consumption is a representation of the nozzle wearing condition which will affect the force. The testing point in this part is limited.

Experimental matrix is given in Table. 3.1

Table 3.1 Experimental Matrix.

Variable	Notation	Value	Unit
Stand-off Distance	Z	2.54, 12.7 25.4, 50.8, 76.2	mm

Variable	Notation	Value	Unit
Sapphire Exit Area	N	0.025, 0.051, 0.08	mm^2
Carbide Exit Area	C	0.458, 0.837, 2.011	mm^2
Abrasive Size	S	50,80,120,220	HP
Abrasive Flow Rate	m	0, 5, 10	Unit on Controller

3.4 Analysis of Experimental Results

3.4.1 Investigation of pure water jet force

In this study, the force is compared with three variables: stand-off distance, sapphire exit area, (called first stage exit area), and carbide exit area (second stage exit area). With two of these variables fixed, the relation between force and the other variable can be found. The fixed variables are defined as parameters, and the changing one is defined as a variable in all parts.

The variation of the sapphire exit area as a function of the force related to a different carbide exit area is clearly shown from Figure 3.5 to Figure 3.7. Generally, the results show that the force will increase as the sapphire exit area increases and the relation seems to be linear. This phenomenon satisfies the principle of mass and momentum conservation. At a steady state, the force of WJ impinging on material surface can be approximated by Equation 3.3 as:

$$Force = K \times m \times V \qquad (3.3)$$

K: Constant.

m: Mass flow rate of the WJ.

V: Mean velocity of the WJ.

The value of m and V are given as

$$m = A \times \rho \times V \qquad (3.4)$$
$$V = K_2 \times \sqrt{P} \qquad (3.5)$$

A; Sapphire exit area.

ρ: Density of water.

K_2: Constant.

P: Water pressure before sapphire.

Since pressure and velocity are keeping constant in this experiment, the mass flow rate will follow as a constant which leads the directly proportional relation of force and sapphire exit area.

Figure 3.5 shows the relation of the force and sapphire exit area with the carbide exit area 0.456 mm^2 (30/1000 inch diameter). In this graph, the force changes with another parameter-stand-off distance. If the maximum force is taken into account, the force drops from 38 Nt. to 1.97 Nt. between the sapphire exit area 0.099 mm^2 to 0.008 mm^2 and the extremity occurs at stand-off distance 12.7 mm, which will be discussed latter. Similarly, the relations related to the carbide exit area 0.937 mm^2 (43/1000 inch diameter) and 2.011 mm^2 (63/1000 inch diameter) are shown in Figure 3.6 and Figure 3.7 which demonstrate the same relations except that the force value decreases. These results suggest that the sapphire exit area is a primary variable of the force function since changing carbide tube will not give so much influence to force.

In comparing the force and stand-off distance, it was found that an optimal stand-off distance was consistently observed in all studies (Figure 3.8-Figure 3.10). This phenomena can be explained as the balance of WJ formation and dissipation with environment.

The carbide tube is used as a mixing chamber to integrate flow stream and abrasive particles. The influence of a carbide tube exit area to WJ force has been studied. It was shown that the approximatedly 20% force will be reduced by this mixing chamber. The result is shown in Figure 3.11.

3.4.2 Investigation of abrasive water jet force

This work involves the detailed analysis of the effect of process variables on the force developed in the impingement zone. The variables involved and their values are given in Table 3.1.

The sapphire cross section area is still a principal factor determining the force. As it follows from Figure 3.12 to Figure 3.14, the effects of other process conditions, except for the abrasive flow rate, are neglectable compared to the sapphire cross-section area.

The carbide tube exit area plays a less important role in the AWJ force. Theoretically, it is believed that a wider mixing chamber will increase the integration effect. However, in our study, this effect is not typically observed (Figure 3.15 and 3.16).

Optimal stand-off distance is also observed in this study (Figure 3.17 - Figure 3.19). The increase of force with increase of stand-off distance at low value of stand-off distance is due to the strong turbulent at the space between nozzle and work piece. When this effect is faded, the increase of stand-off distance diminishes the force. The range of the force changes, due to the change of stand-off distance, and does not exceed 3 Nt.

3.4.3 The influence of carbide wearing condition to the force

The carbide tube's inside shape will be changed by abrasive particles passing through it. It was found that when the total consumption of abrasive increases the abrasive jet force

will decrease but the pure water jet force will increase(Figure 3.20).

3.5 Conclusion

In the consideration of stress generated by the WJ-workpiece interaction, the maximum momentum generated is far below the momentum needed for the resulted stress reaching the yielding point of material. Therefore, the damage mechanism associated with WJ is not in elasto-plastic damage. Thus, a more detailed study of the material damage surface formation is needed.
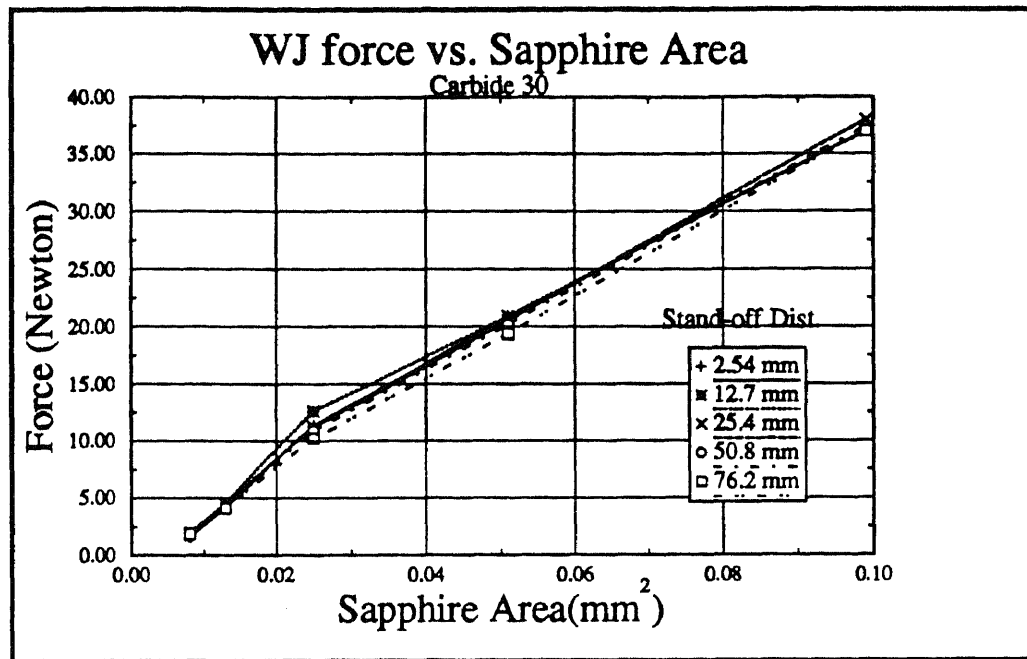
Figure 3.5
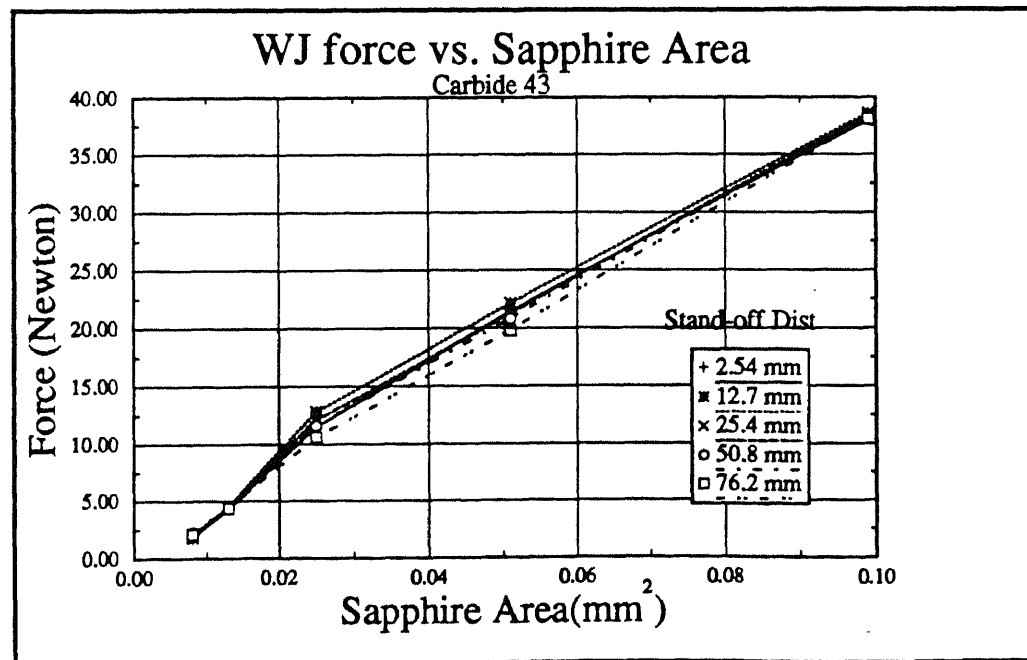
Figure 3.6
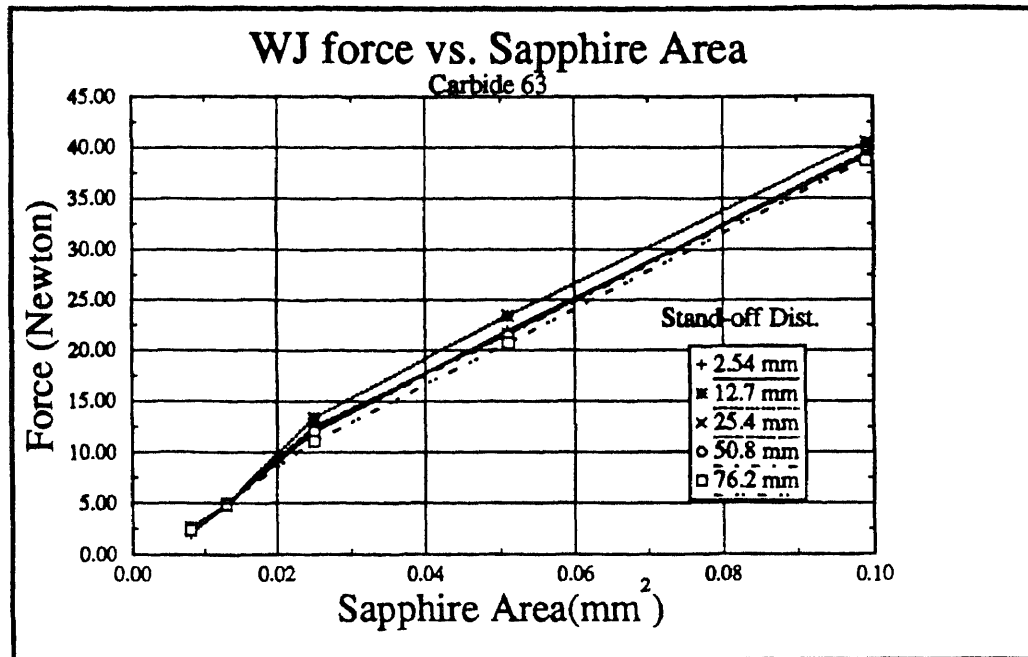
Figure 3.7
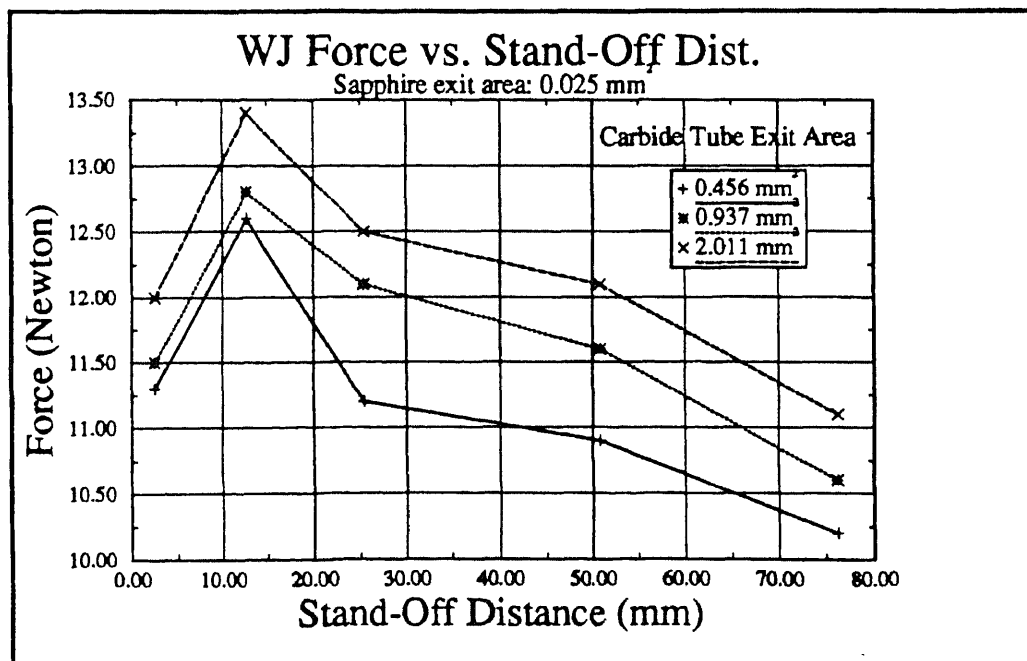
Figure 3.8
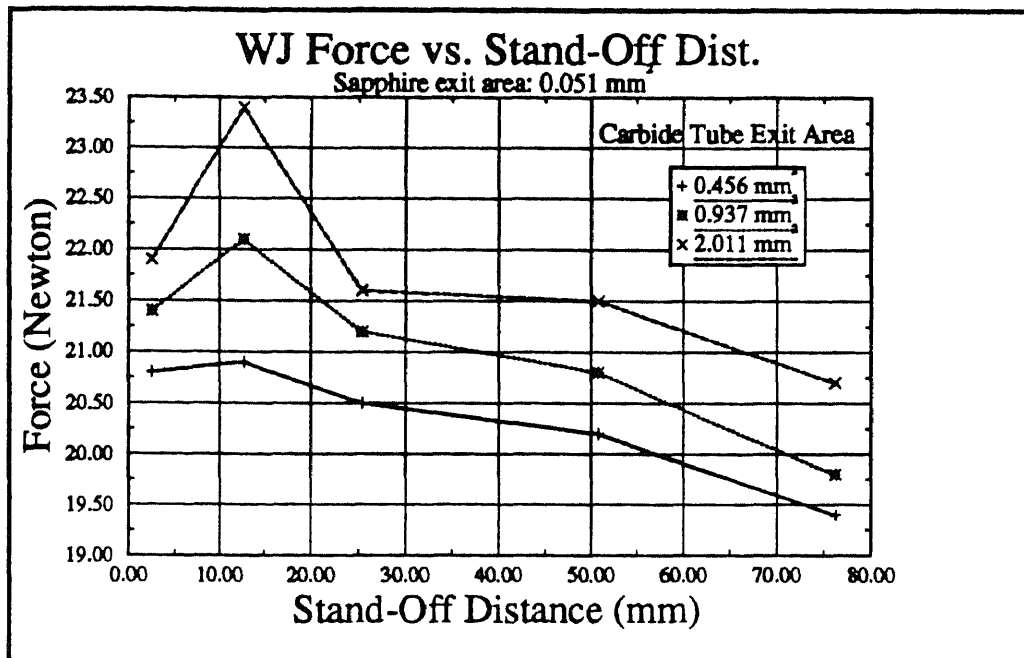
Figure 3.9
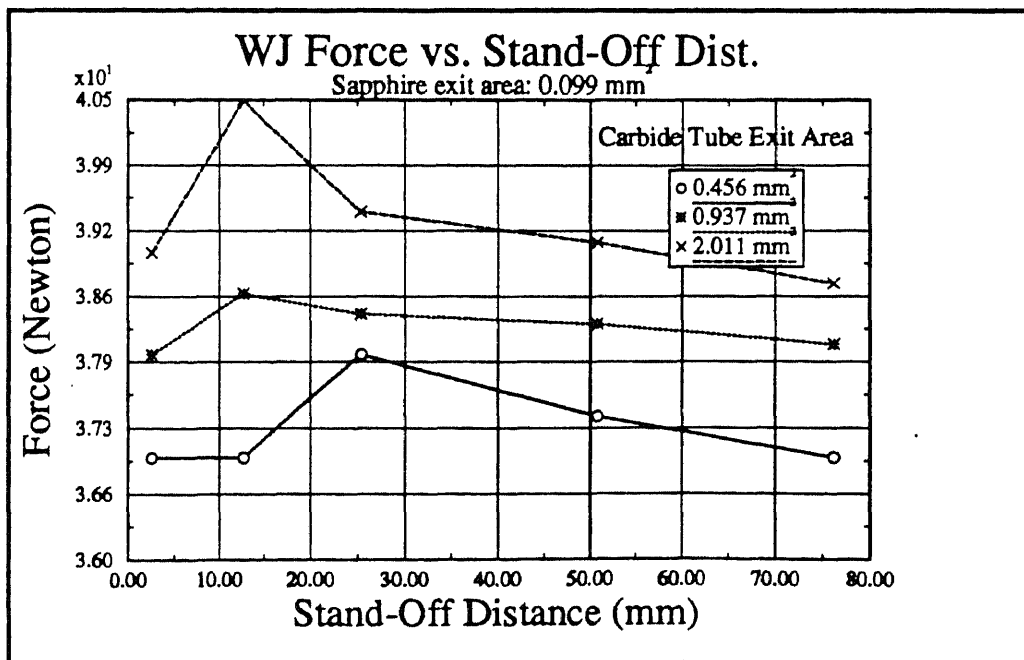
Figure 3.10

Figure 3.11

Figure 3.12

AWJ Force vs. Sapphire Exit Area

Carbide Tube: 0.456 mm², Stand-Off Dist.: 12.7 mm, Abrasive Mesh: 80

Force (Newton)

Abrasive Flow Rate
- o No Abrasive Flow
- ⚹ 109.25 g/min
- × 445 g/min

Sapphire Exit Area (mm²)

Figure 3.13

AWJ Force vs. Sapphire Exit Area

Carbide Tube: 0.456 mm², Stand-Off Dist.: 12.7 mm, Abrasive Mesh: 120

Force (Newton)

Abrasive Flow Rate
- o No Abrasive Flow
- ⚹ 118.25 g/min
- × 498.5 g/min

Sapphire Exit Area (mm²)
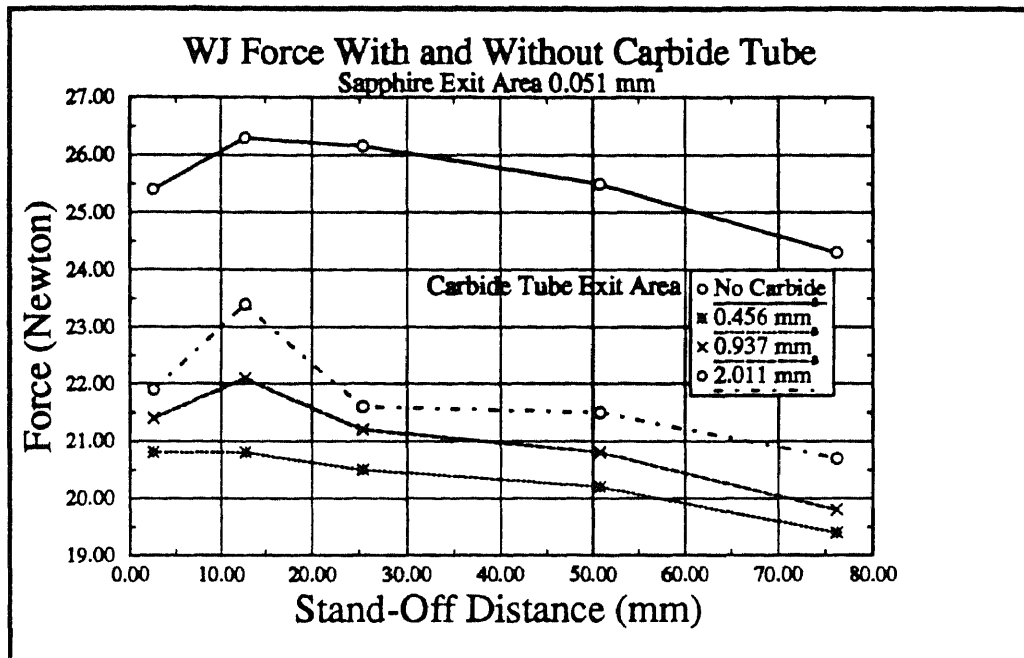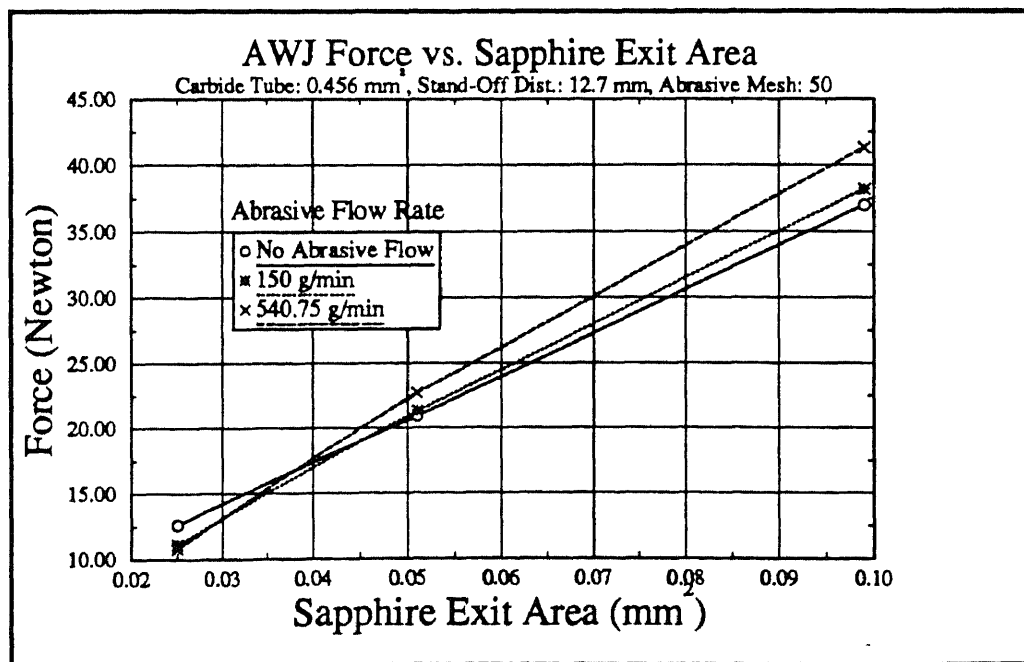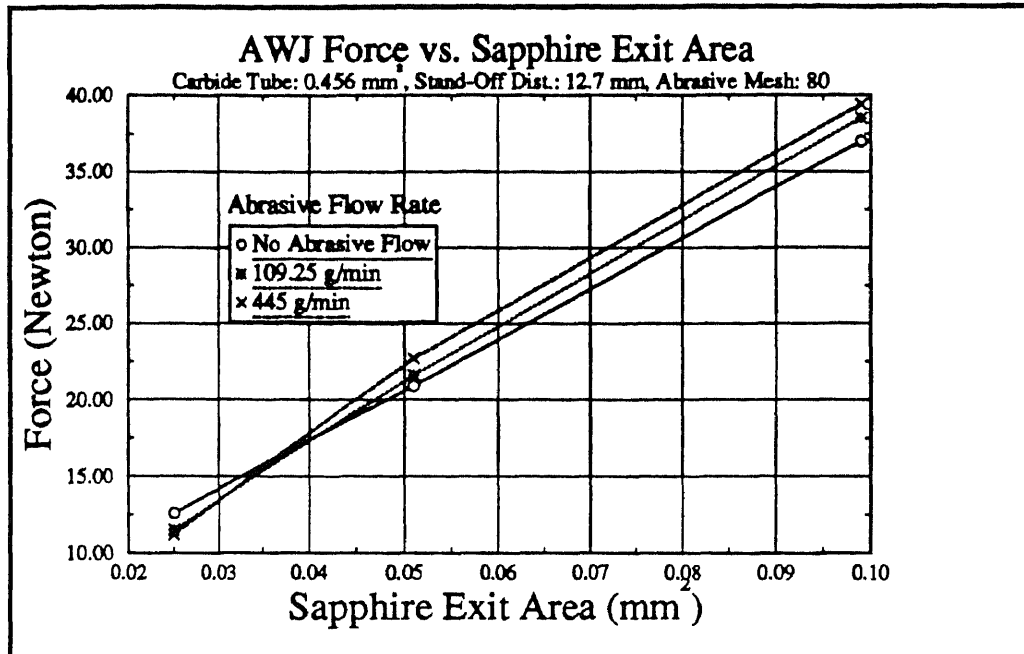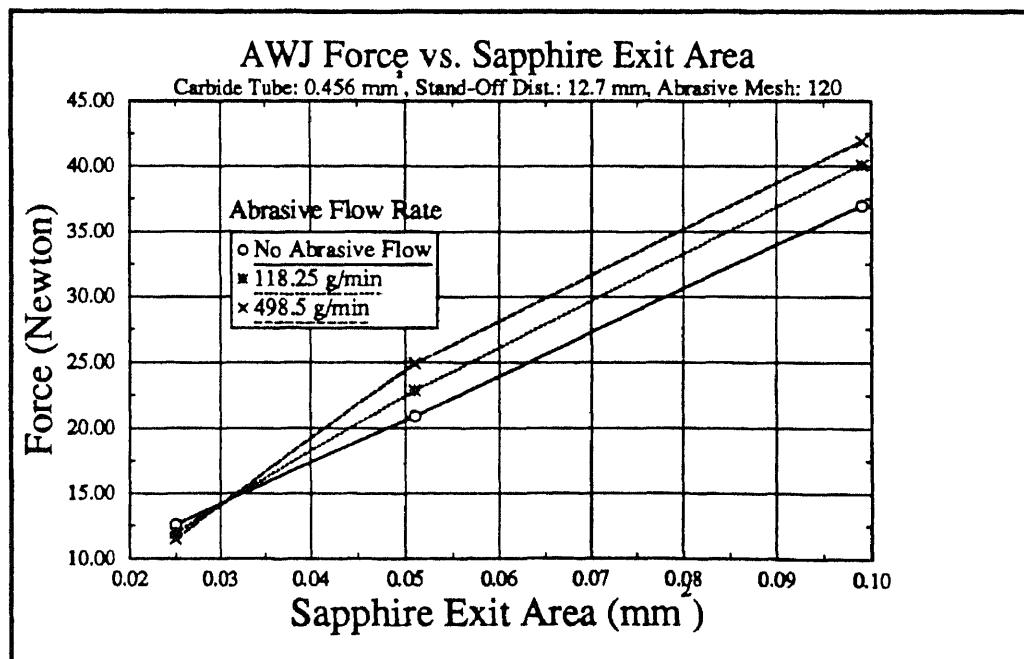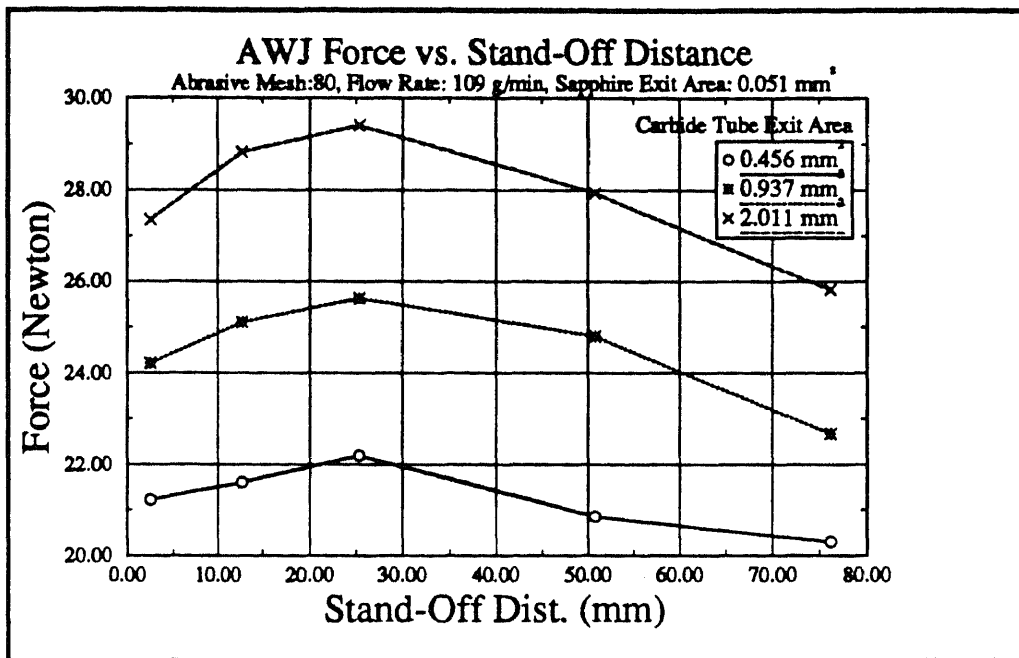
Figure 3.14
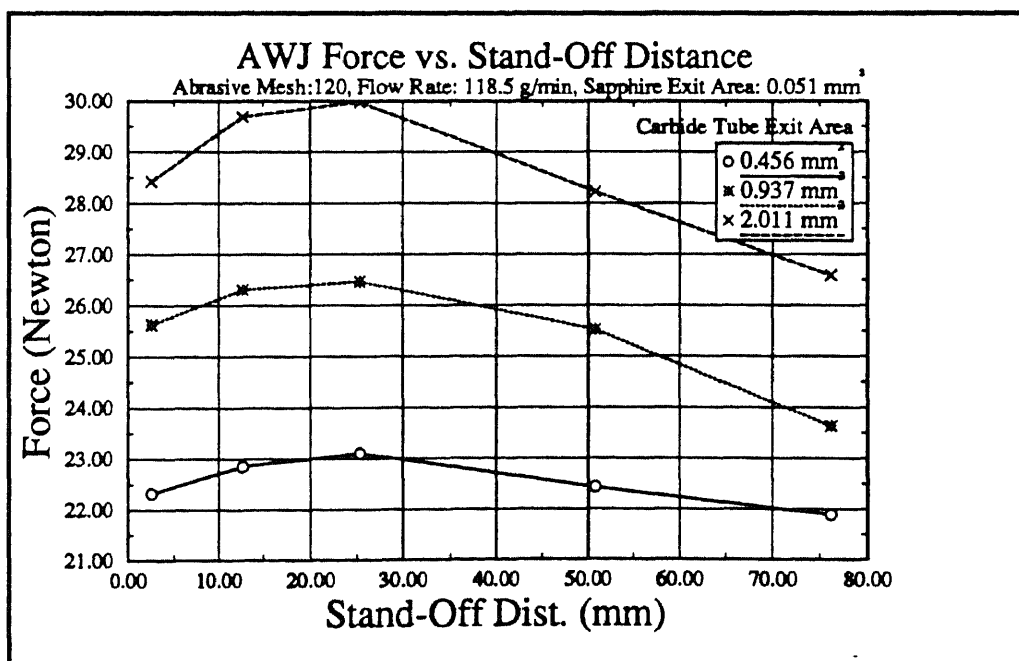
Figure 3.15

Figure 3.16
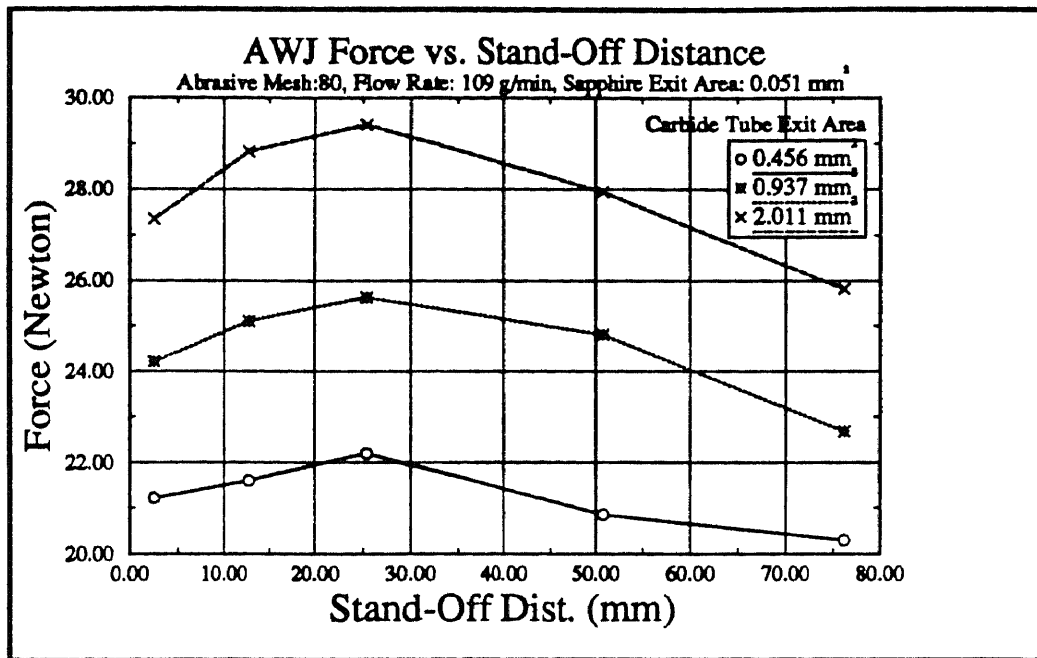
Figure 3.17
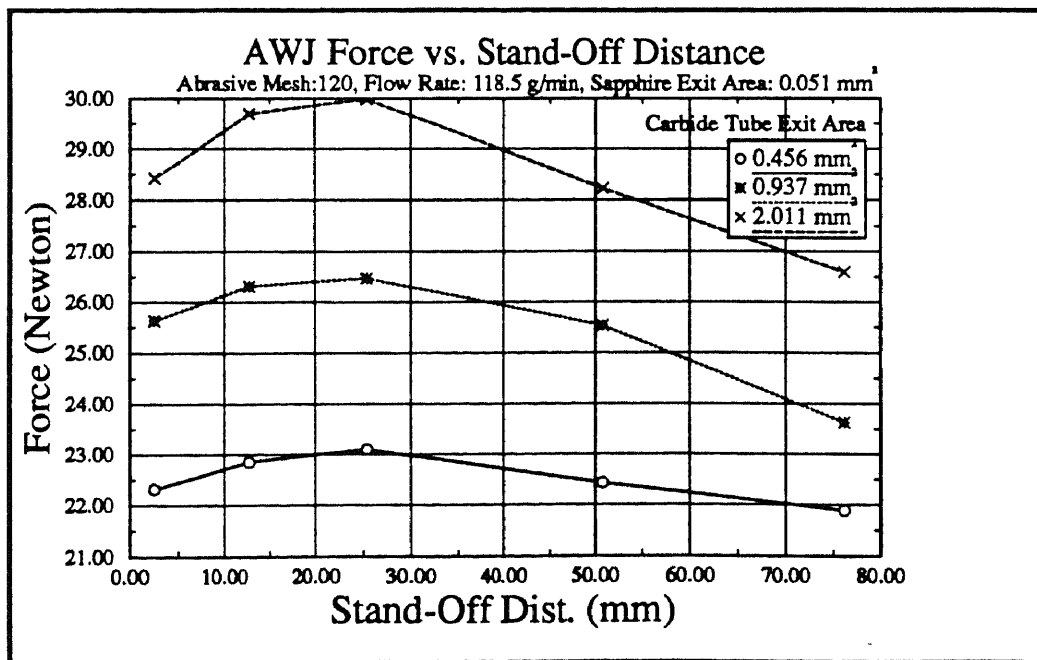
Fig, 3.18
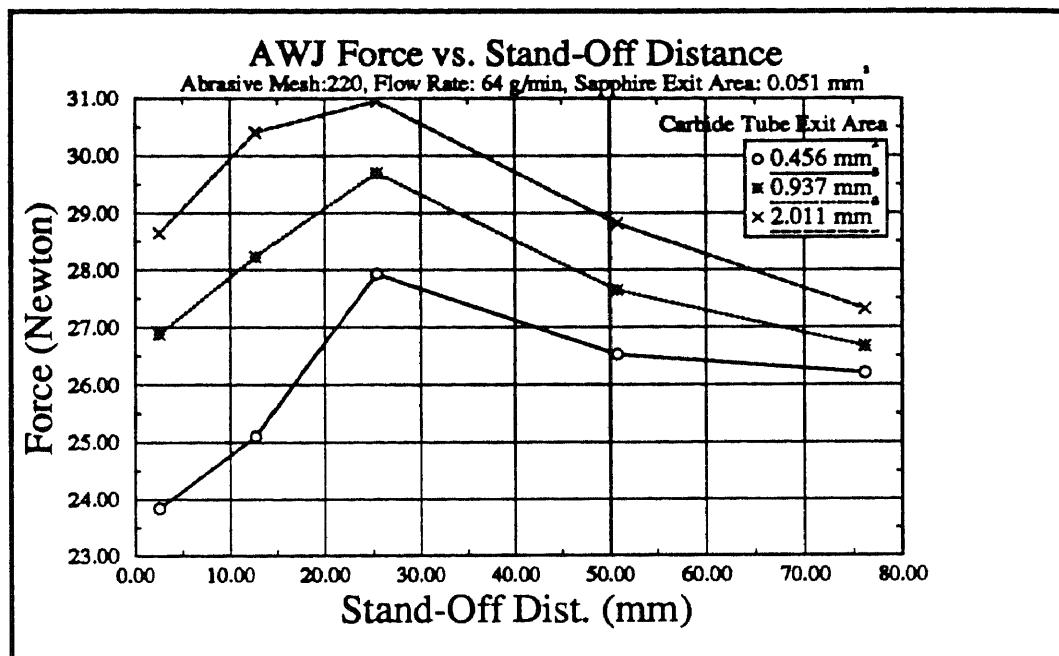
Figure 3.19
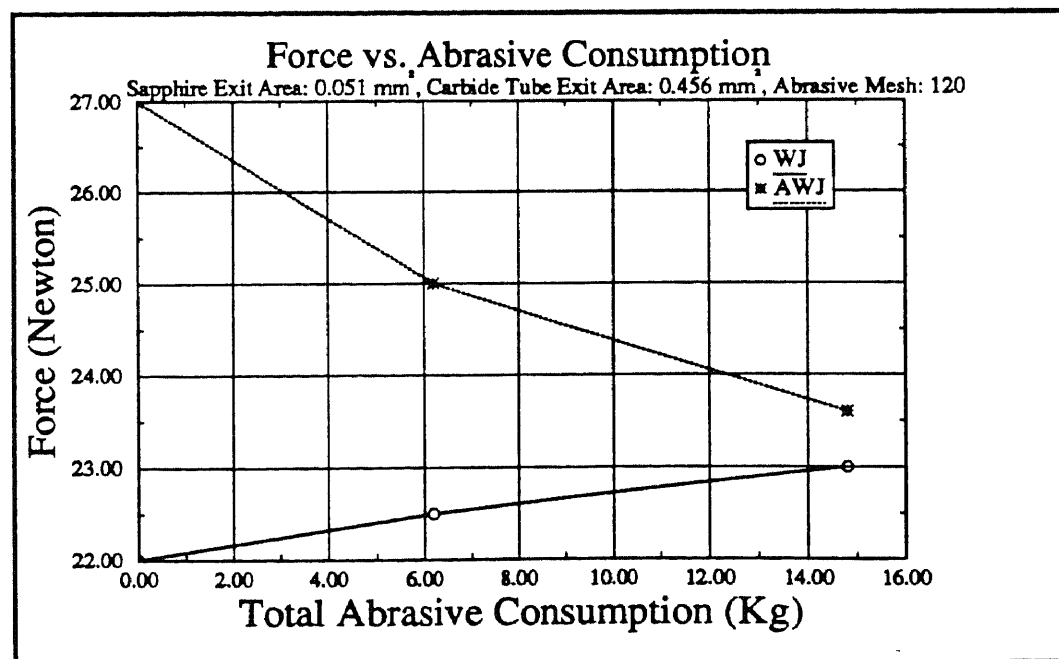
Figure 3.20

CHAPTER 4

MACROGRAPHIC STUDY OF THE GENERATED MATERIAL SURFACE

4.1 Introduction

When material is impinged upon by WJ, stresses developed on the interface will create damage to the material surface. This damage may be in the form of cracks, pits or material weight loss and is often referred to as erosion or cavitation. In order to understand the material damage mechanism and process, the response of materials to impingements must be understood. Such understanding may be gained either through experiments and testing, or through analytical models. In this study material response to the WJ impingement is carried through experimental results.

Considering a material impinged upon by WJ, properties of both the WJ and the material may vary as the result of the damage. A set of parameters which may affect the results has to be identified to accurately correlate the material damage model. According to many experimental results, the following parameters may influence the erosion process [43].

(a) Liquid parameters

    1. Density
    2. Velocity of a compressive wave
    3. Viscosity
    4. Surface tension

(b) Interface parameters

    1. Impact velocity
    2. Impact angle

(c). Material parameters

1. Density
2. Velocity of compressive wave and shear wave
3. Modulus of elasticity
4. Poisson ratio
5. Endurance limit
6. Ultimate tensile strength
7. Compressive and shear strength
8. Fracture toughness
9. Hardness
10. Grain size
11. Surface toughness
12. Curvature of surface
13. Thickness

One of the first empirical relations, obtained by Engel [38], which was based on dimensional analysis, was reported to relate the size of pits formed by impingement droplets to the above parameters. Eisenberg [44], Hammit [45], Heymann [36], and Pouchot [46] also present a wide range of test results. Each correlation simply related the damage to a variety of test parameters. A comprehensive correlation which has contained the most of the relevant parameters seems to have been beyond reach and still is so.

However, experimental evidence indicates that within a wide range of conditions, the weight loss of a material subjected to impingements of liquid jet varies with time, as shown in Figure 4.1. At the beginning of such interaction, weight loss is insignificant. After this so called incubation period, the rate of the weight loss becomes a constant. This period is called the steady rate erosion. Beyond this time frame the relationship between weight loss and exposure time becomes more complex and unpredictable. This time frame is referred as the final erosive state.

Experiments based on continuous WJ loadings have been carried out by many diffeent combinations of parameters. Murai [34] correlated the material loss of aluminum and stand-off distance. Two material loss extrema have been observed. The first extremum is due to the fracture of the circumference and bottom of the penetrated pits by the

impact pressure of the jet core zone. With increase in exposure time, the core penetrated into the material deeper and stagnation pressure in the eroded pits became more effective in fracturing material. Similar experimental results have been reported ed by Yamaguchi and Shimizu [19].

4.2 Experimental Procedure

Steel, ANSI-SAE 1080, was used for this erosion rate experiment. The size of the samples was 25.4 mm X 25.4 mm, and thickness varied from 6.35 mm to 63.5 mm. Impingement was carried out at an intensifier pressure of P=47 ksi and a nozzle diameter of 0.356 mm. The stand-off distance was varied to the values of 12.7 mm, 19.05 mm, and 25.4 mm. Interaction duraion varied from 1 to 20 seconds.

The material surface was investigated using a Video-Matrix digital microscope. This microscope has a 4 micro inches resolution for each of 3 three movement axes; and the optical resolution varied from 120 to 52 micro inches. The measurement accuracy was 0.0003 inch.

4.3 Experimental Results and Discussion

Typical erosion history profiles are shown in Figure 4.3 to Figure 4.5. The observed flatness of the cavity bottom surface of the material surface did not generally exceed 0.02 mm. The stand-off distance seems to present no effect on this flatness, although the duration of the interaction did affect the depth and volume of the material damage.

An exception of the cavity profiles appeared at a stand-off distance of 12.7 mm and an impact duration of 1 second is presented in Figure 4.2. The center of the cavity was observed to be less damaged than the boundary region. Erdmann [15] attempted to relate this to flow anatomy; impingement of droplets, which constitute the outer ring of the flow, results in more intensive material removal than the comparatively compact core zone

region. This explanation can be completed by the large amount of water droplet composed in the boundary of the jet and continuous liquid flow in the jet core zone.

Figure 4.6 to Figure 4.8 represent the volume removal history. Two regions have been defined on the material surface as the wall side region and the core zone region. The core zone region is defined as a rectangular area based on the cavity bottom, while the wall side region is the total volume removed excluding this core zone region volume. It is computed that the central part of the cavity took about 85% of the total volume removed and the other 15% was shared by the wall side volume, as shown in these graphs.

In the same interaction time base, the larger the stand-off distance is, the smaller is the core zone volume removed. This observation is compatible with the results from Chapter 3. In the wall side of the cavity, the volume removed rate is much smaller than the core zone area, which suggests that the damage rate in these two regions is different. The volume removed rate in the wall side can be almost zero. It is also noted that the volume removal rate at 25.4 mm has the smoothest growth rate. The formation of the jet and its stability may be contributed to this observation.

A summary of the depth of cut history is given in Figure 4.9. This chart demonstrates that the depth of cut is approximately directly proportional to the duration of interaction after 2 seconds. The depth of cut has an irregular jumping between 1 second and 2 seconds interaction. Mathematically, linear curve fitting equations of the cutting depth and interaction time after 2 seconds are given as:

$$d = 0.0176 \times t + 0.2018 \qquad Z = 12.7mm \qquad t \in [0, 20]$$
$$d = 0.0209 \times t + 0.2738 \qquad Z = 19.0mm \qquad t \in [0, 20]$$
$$d = 0.0218 \times t + 0.3527 \qquad Z = 25.4mm \qquad t \in [0, 20]$$

Figure 4.10 shows that, except for a brief initial period, both upper (D_t) and bottom (D_b) kerf widths were practically constant. The dynamics of material removal (i.e., constant rate of destruction and constant shape of cavity) suggest that such removal is

due to metal erosion at the region of the metal-jet interaction.

The affect of the sample thickness on the rate of material removal for various cutting speeds of a WJ is shown in Figure 4.11. The extremum at a specific thickness observed in these curves demonstrates the strong affect of the sample geometry on the rate of material removal. It is difficult to imagine any mechanism that can account for this other than that of the resonance of stress waves. Conversely, in the case of AWJ impingement, the sample thickness had no effect on the rate of the material removal (see Figure 4.12). The material destruction by AWJ is due to effects of the individual particles, and the process is localized in the vicinity of impingement and does not depend on global conditions in the solid.

4.4 Conclusion

Material damage rate increases constantly although two damage rates on the material surface were observed. The center part of the material cavity, damaged by the core of the jet, possessed a higher damage rate, while the damage rate on the wall side of the cavity was smaller. This observation implies that impact loading is not uniformly distributed across a jet.

A constant damage cavity size demonstrates that material damage growth is not affected by duration of interaction, which suggests that in the interaction the damage was in microscale.

Material damage depth will be affected by the thickness of the workpiece in the course of WJ impingement, as observed. However this effect was not observed in AWJ impingement which presented different damage mechanisms. Therefore, Microscopic Fractography study became necessary; the results of this study are present in Chapter 5.
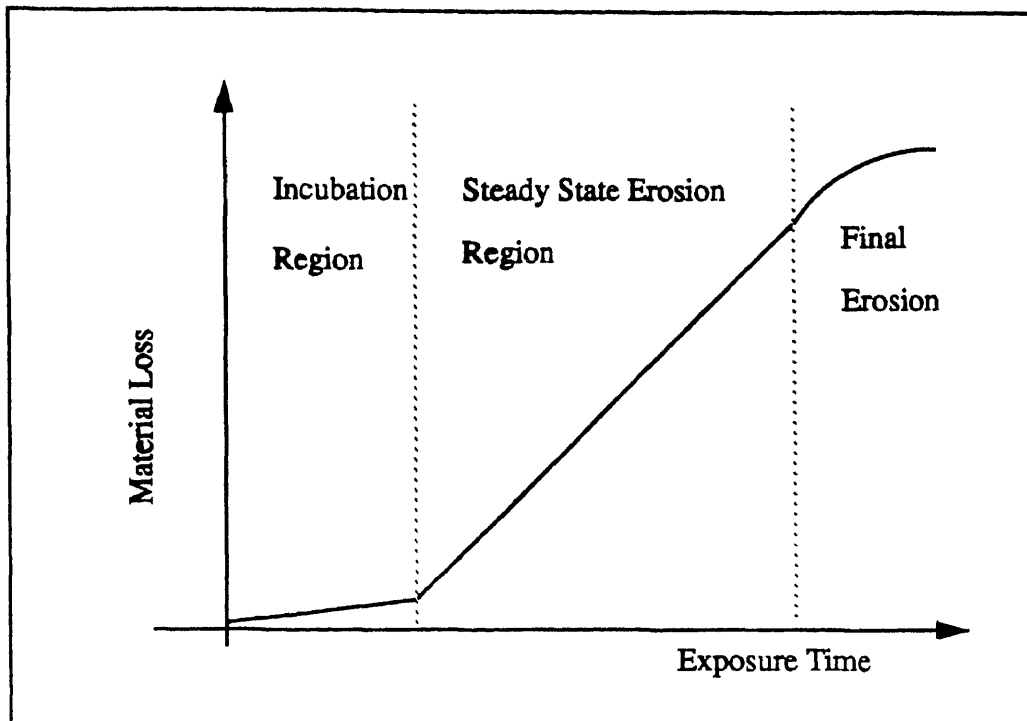
Figure 4.1. Typical erosion material loss history.
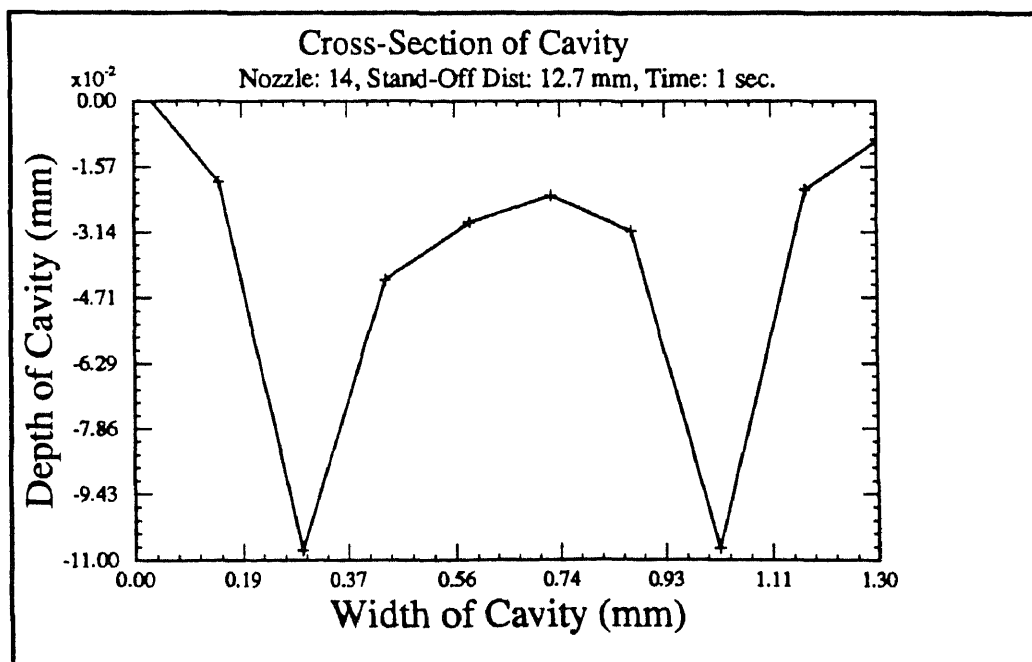
Figure 4.2. An exceptive cavity profile.

Notice that the center of the cavity has less damage than the wall side of it.
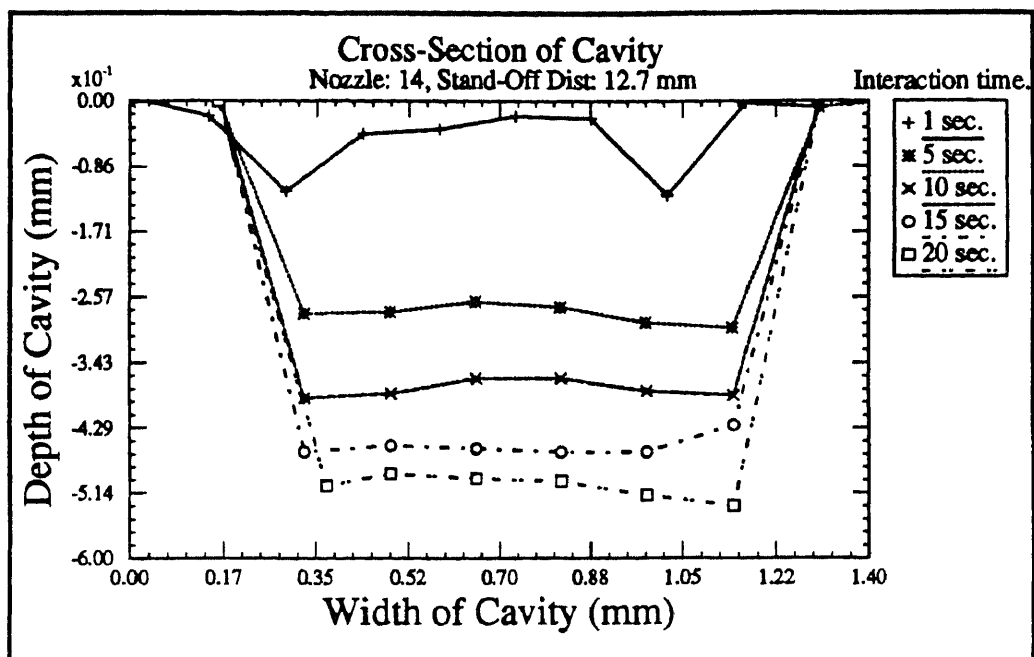
Figure 4.3. Cavity profile growth history.

Notice the jumping between 1 second and 2 seconds.
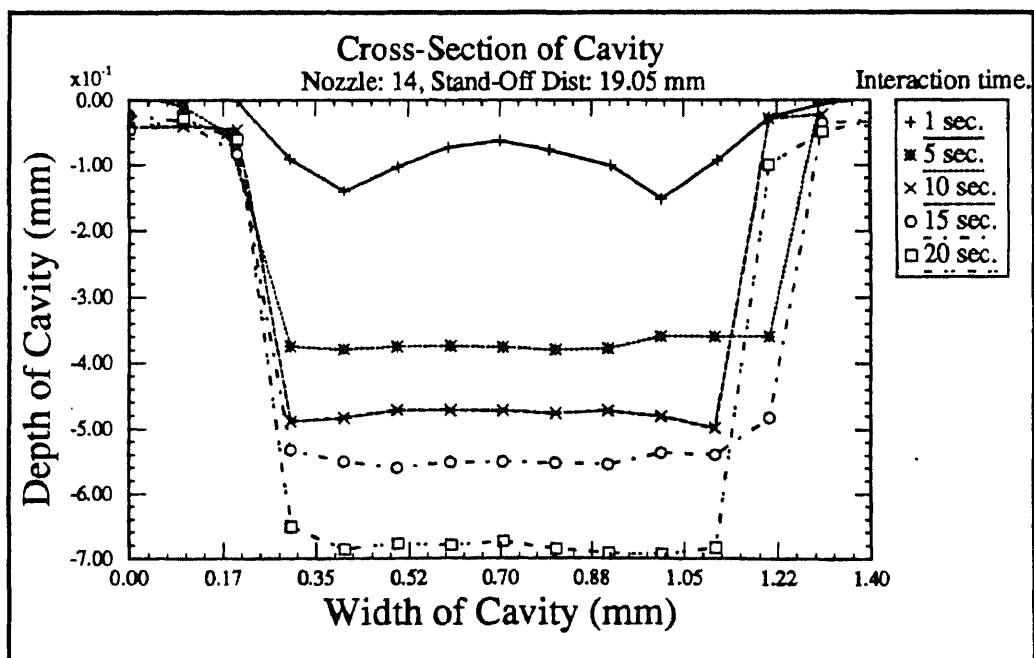
Figure 4.4. Cavity profile growth history.

Notice the jumping between 1 second and 2 seconds.
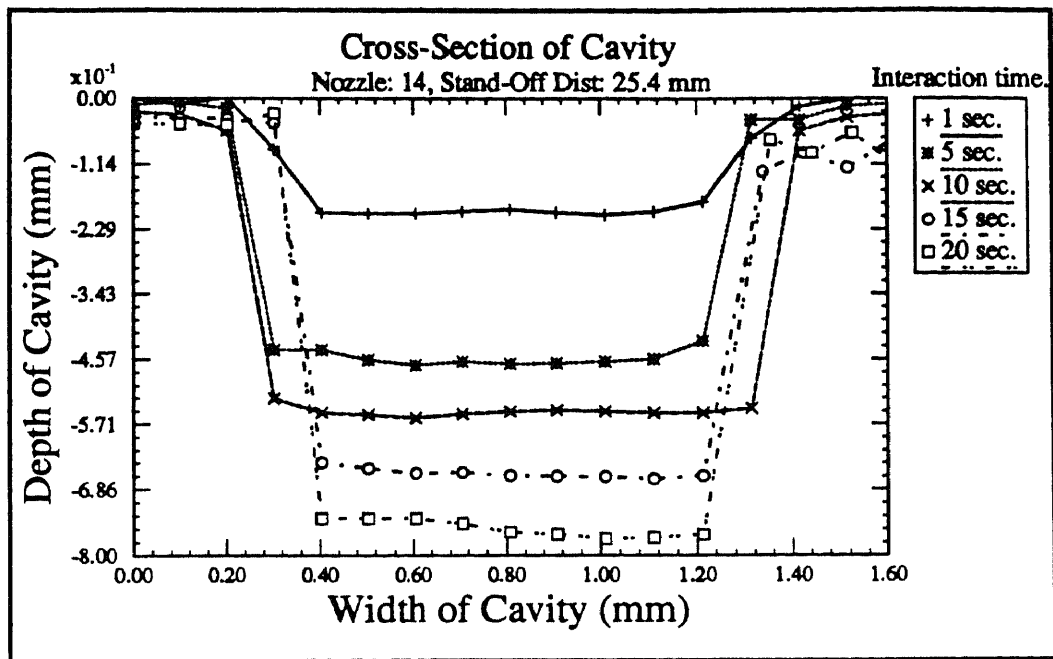
Figure 4.5. Cavity profile growth history.

Notice the jumping between 1 second and 2 seconds.
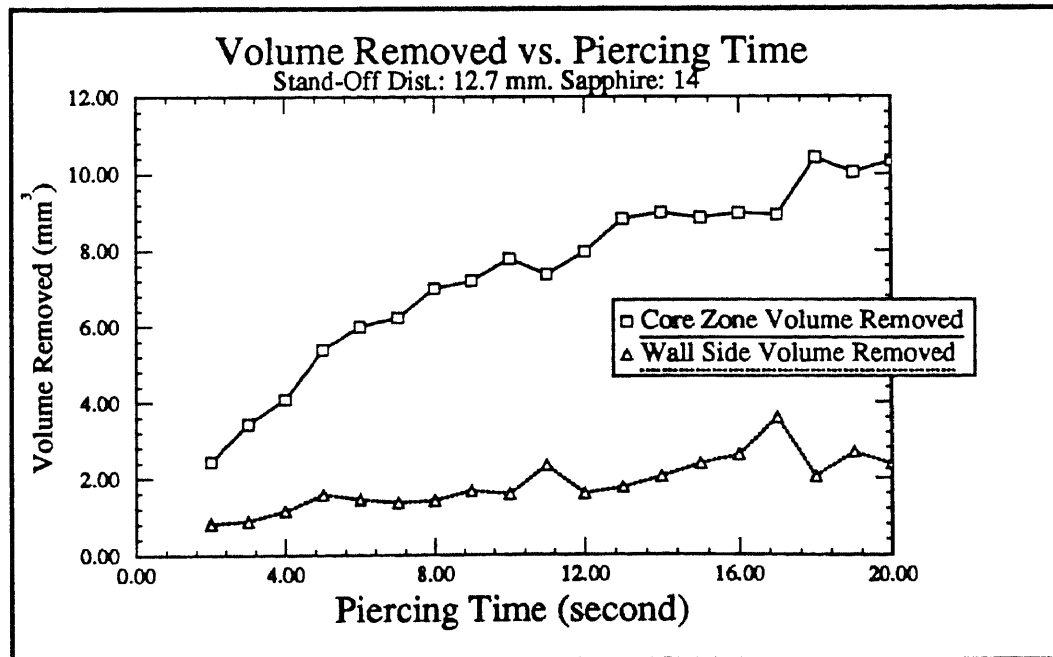
Figure 4.6. Volume removed history.

Notice the linear increase in the core zone region and smaller increase in wall.
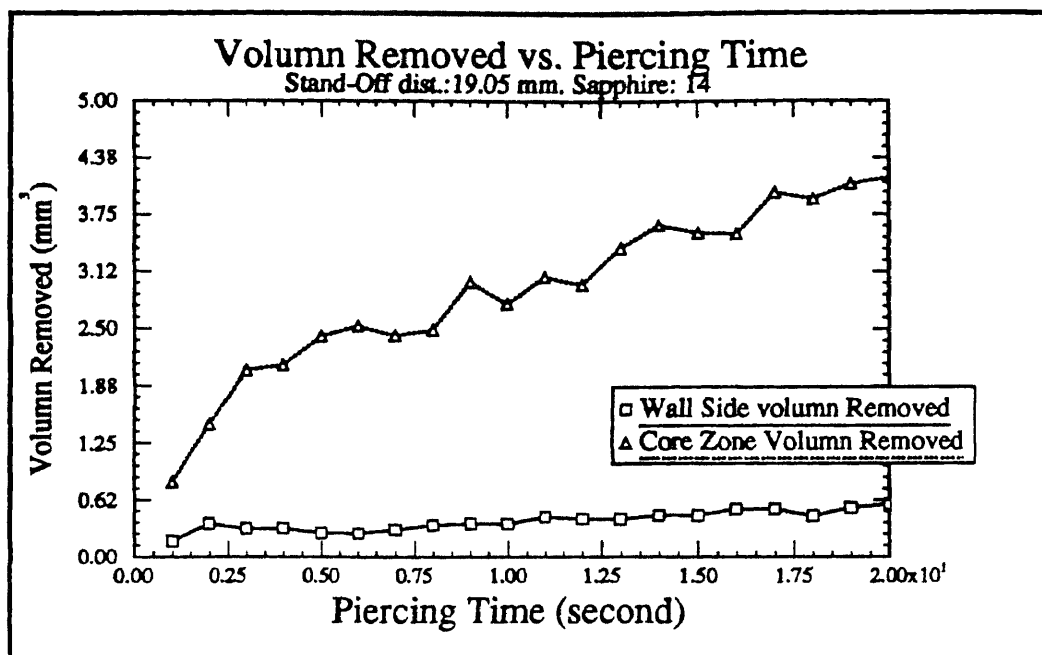
Figure 4.7 Volume removed history.

Notice the linear increase in the core zone region and smaller increase in wall.
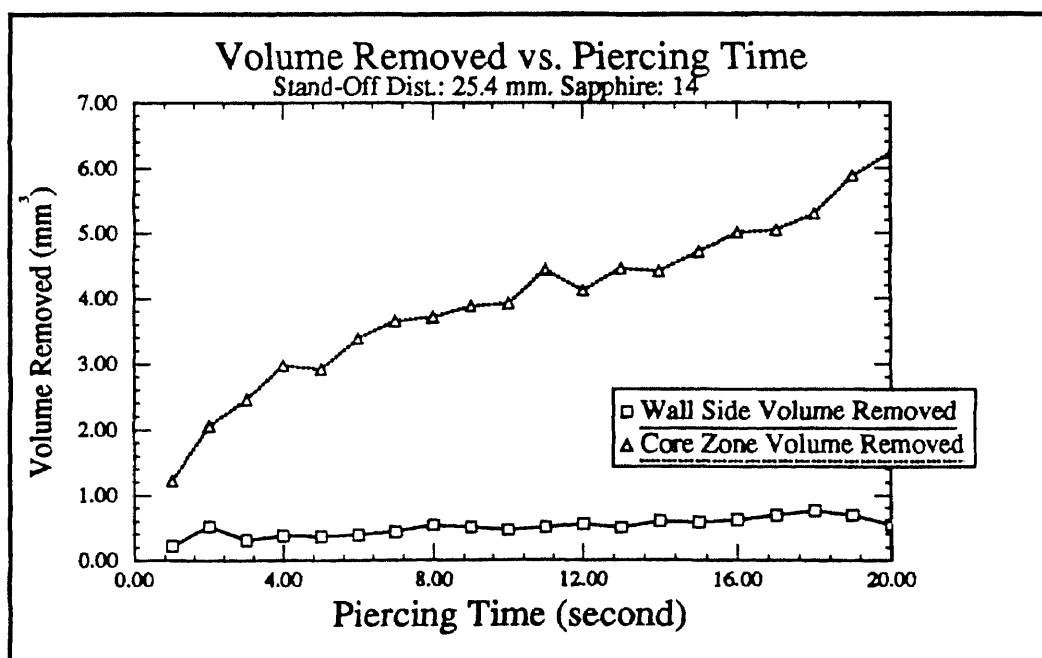
Figure 4.8. Volume removed history.

Notice the linear increase in the core zone region and smaller increase in wall and smooth growth compared with Figure 4.6 and Figure 4.7.
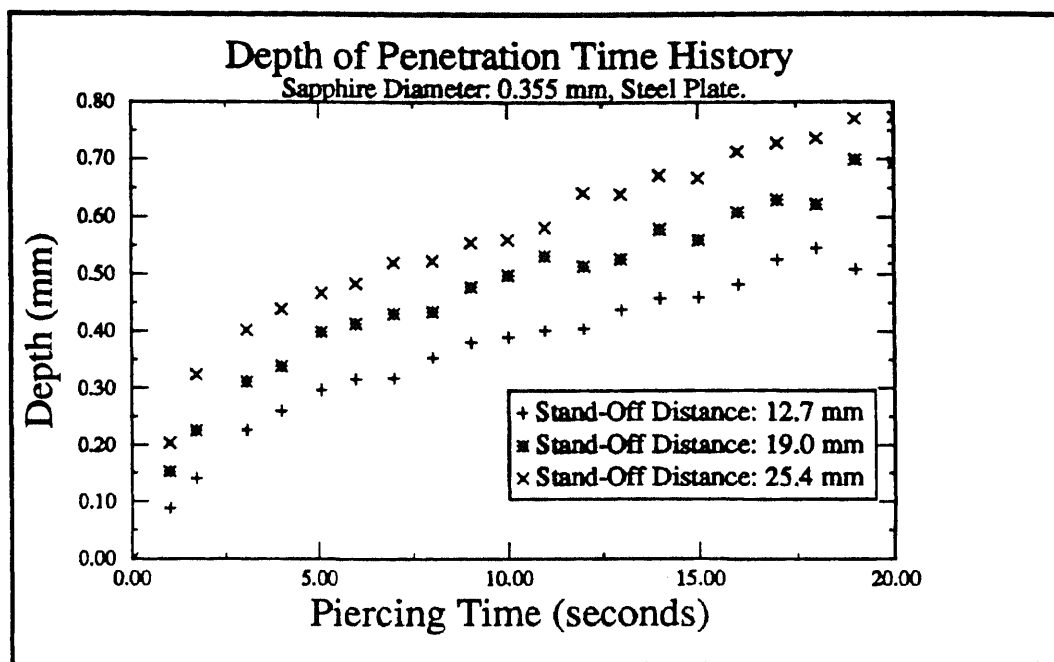
Figure 4.9. The history of the penetration depth. Notice the linear increase of all curves. beyond the starting transient.
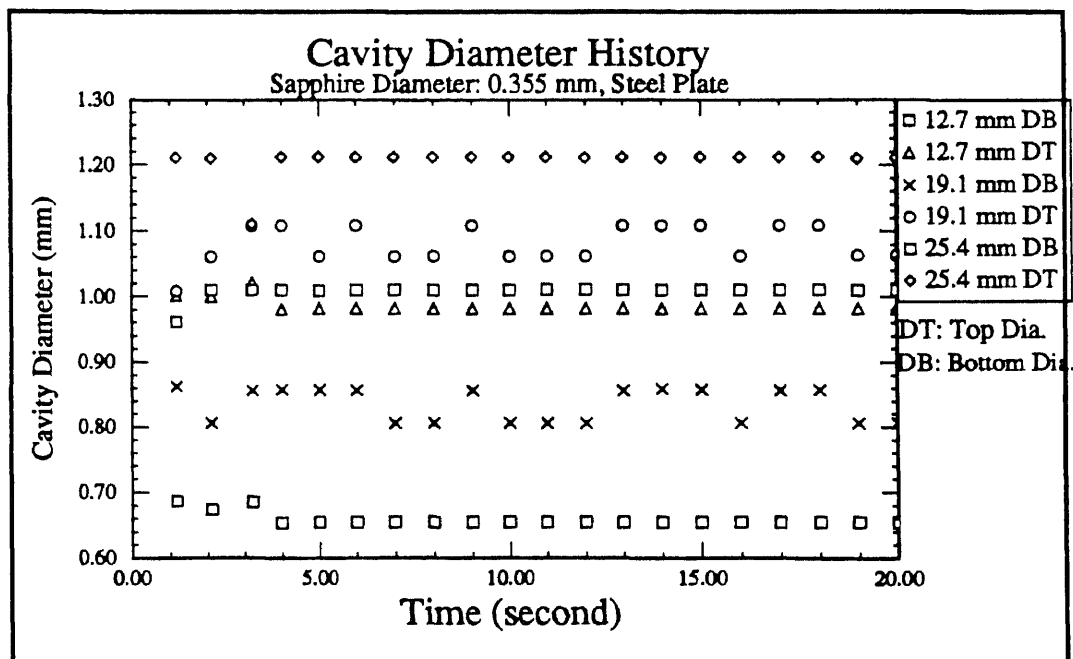
Figure 4.10. The history of cavity damage area.
Notice that the cavity diameter does not change with time.
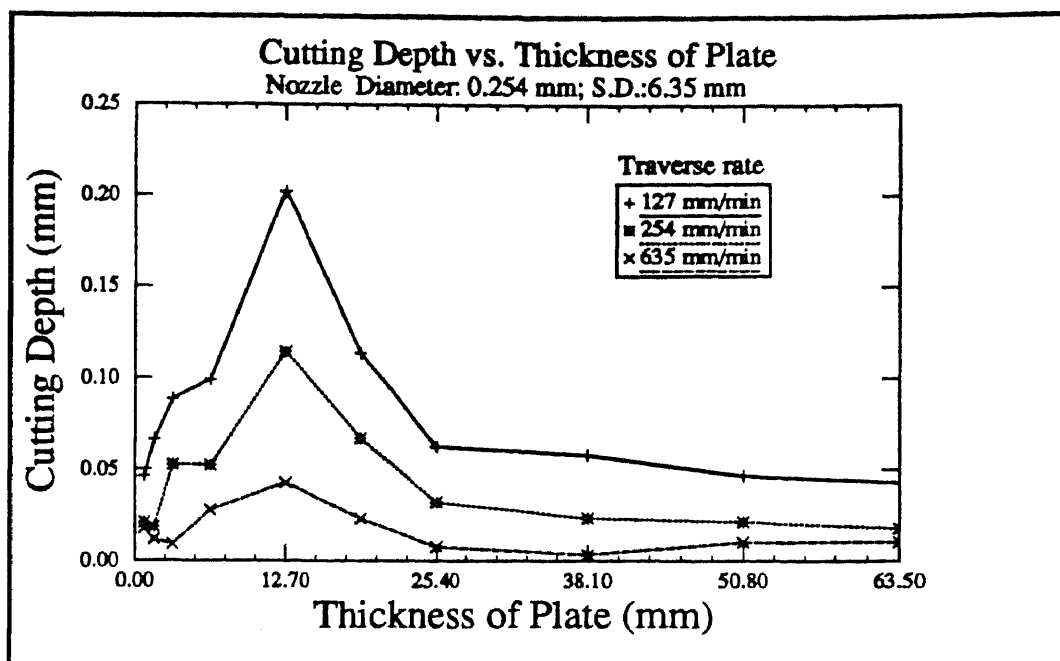
Figure 4.11. Cutting depth in the function of plate thickness

Notice the extremal point at the 12.7 mm thickness.
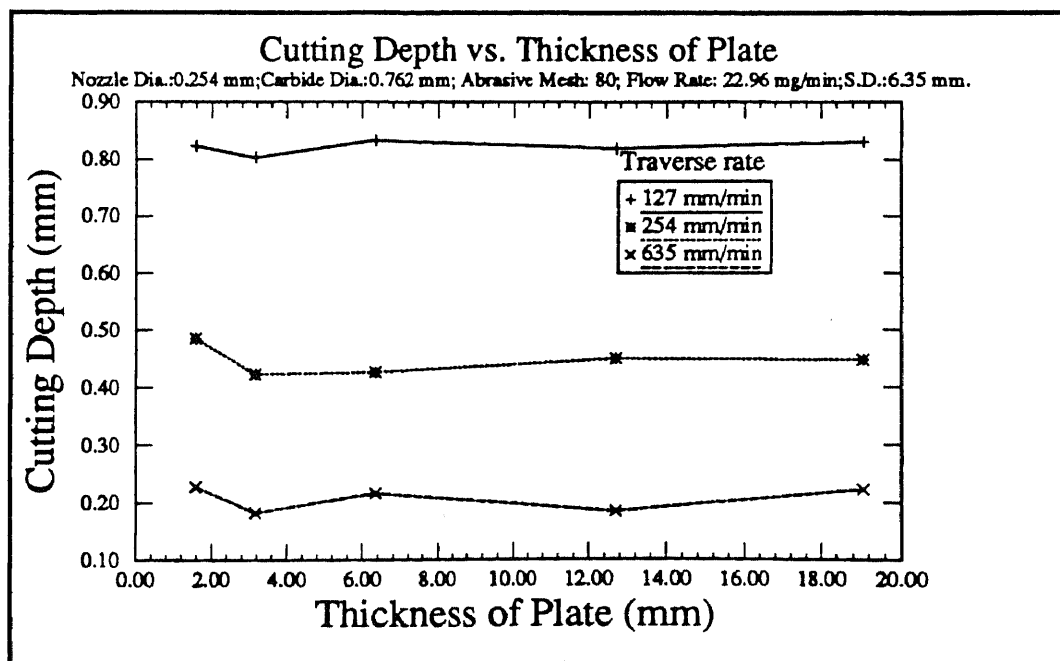
Figure 4.12. Cutting depth in the function of plate thickness by abrasive water jet.

Notice that no extremal point exists.

CHAPTER 5

MICROGRAPHIC STUDY OF

THE GENERATED MATERIAL SURFACE

5.1 Objective

The objective of this study is to characterize the fracture mode of metal during water jet machining by using optical and scanning electronic microscopes. The information revealed by obtaining micrographs enables us to identify the mechanism of material fracture. Material surfaces during abrasive water jet machining have also been studied. The polished cross section of the sample material surfaces have been electrodeposited by copper and investigated by optical microscope and represent the direct statement of the fracture mechanisms.

5.2. Introduction

Metal fails in many different ways and for different reasons. Determining the cause of failure is essential in either preventing or simulating such a process. One of the most important sources of information relating to the cause of failure is the fracture surface itself. It contains evidence of loading history, environmental effects and material quality. The principal technique used to analyze this evidence is electron fractography [48].

Electron fractography is collected by the use of higher magnification techniques of fracture examination, particularly Transmission Electron Microscope (TEM) or Scanning Electron Microscope (SEM).

Scanning Electron Microscopy uses a highly focused beam (less than 10 mm diameter) which can be scanned in a raster on the sample surface. The intensity of second-

ary electrons produced at each point is used to form a picture of the sample. Magnification factors from 10X to 100,000 X can be obtained. The depth of field is inherently quite large which allow the micrographs to be in focus at all points across a rough surface. In addition, the SEM does not suffer from the light microscope problem of light reflecting off at odd angles and being lost from view. Micrographs are marked with full identification. The sample number/description and area designation are noted on the top one or two lines. Next is the magnification and finally the micrograph sequence code which refers to the sample being examined and particular area on the sample.

Through the study of the fractography, there is a group of microscopic appearance often called "fracture mode". Each of these modes has a characteristic fracture surface appearance and a mechanism or mechanisms by which the fracture associated.

Regardless of the fracture path, all classical microscopic fracture detail into four classical modes-" Dimple Rupture ", " Cleavage ", "Fatigue ", and " Decohesive Rupture ". There is a consequent tendency to assign any particular topography to one of these modes. However, it is often that the majority of a fracture surface is "ill defined" in classical terms and often one must search to find local areas which are adequately representative of the mode assigned.

• Dimple Rupture: When material failed because of exceeding the fracture limit, a failure process called "microvoids coalescence" is usually the principal cause. As the stress in the material increases to over yielding limit, the plastical deformation generated and local plastical deformation creates microvoids. Eventually a continuous failure surface is generated by these microvoids coalescing. This surface exhibits numerous cuplike depressions which are the direct result of coalescence. These cuplike depressions are referred to as dimple and the fracture process mode is known as dimple rupture (Figure 5.1).

The size of dimples on the fracture surface is governed by the number and distribution of microvoids that are nucleated. When the nucleation sites are few and widely spaced, the microvoids grow to a large size before coalescing and form a large dimple.

When the coalescence happened before nucleation, small dimples are formed. Extremely small dimples are often found in oxide dispersion strengthened materials.

The state of stress within the material as the microvoids form and coalescence affect the shape of the dimples. Equiaxial dimples bounded by a lip or rim are the result of tension and compression (Figure 5.2). Depending on the microstructure and plasticity of the materials, the dimple can exhibit a very deep, conical shape (Figure 5.2) or can be quite shallow (Figure 5.3). The formation of shallow dimples may involve the joining of microvoids by shearing along slip bands. The elongated dimples are the result of tearing or shearing loading locally. The characteristics of an elongated dimples are elongated and open in one side, that is the dimple not completely surrounded by a rim. In the case of tearing, the elongated dimple are oriented in the same direction.

• Cleavage: Cleavage is a low-energy fracture that propagates along well-defined low-index crystallographic planes known as cleavage planes. This fracture surface should have perfectly matching faces and should be completely flat and featureless (Figure 5.4 and Figure 5.5). However, the true flat and featureless cleavage is seldom observed due to the imperfection of material. As the consequence of this, cleavage fracture produces distinct features, such as cleavage steps, river patterns, feather markings, chevron patterns and tongues.

Cleavage steps: Cleavage fractures frequently initiate on many parallel planes. As the fracture advances, the number of active planes decreases by a joining process that forms progressively higher cleavage steps (Figure 5.6).

River pattern: The network of cleavage steps is called river pattern. This pattern can be used to establish the local fracture direction (Figure 5.4).

Feather marking: Feather markings are a fan-shaped array of very fine cleavage steps on a large cleavage facet. The apex of the fan points back to the fracture origin (Figure 5.6).

Tongue: Tongues are occasionally observed on cleavage fractures. It is formed when a cleavage fracture deviates from the cleavage plane and propagates a short distance along a twin orientation (Figure 5.5).

• Fatigue: A fracture that is the result of repetitive or cyclic loading is known as a fatigue fracture. A fatigue fracture generally occurs in three stages: it initiates during stage I, propagates in stage II and proceeds to catastrophic fracture during stage III.

Fatigue crack initiation and growth during stage I occurs principally by slip-plane cracking due to repetitive reversals of the active slip systems in the metal (Figure 5.7 and Figure 5.8). The crack tends to follow cryptographic planes, but changes direction at grain boundary. At large plastic-strain amplitudes, fatigue cracks may initiate at grain boundary. The stage I surfaces are faceted, often resemble cleavage, and do not exhibit fatigue striation. Normally observed on high-cycle low-stress fractures and absent in low-cycle high stress fatigue.

In stage II of fatigue fracture, cracks grow principally occurred by transgranular fracture and is more influenced by the magnitude of alternating stress in stead of the mean stress. The fatigue striations are usually observed in this stage (Figure 5.9 and Figure 5.10).

Under normal conditions, each striation is the result of a single loading cycle and marks the position of the fatigue crack front at the time the striation was formed. However, when there is a sudden decrease in the applied load, the crack can temporarily stop propagation, therefore no striation formed, and resumes only after a certain number of cycles are applied at the lower stress.

The space between striation is primarily governed by the magnitude of alternating stress. Increasing the magnitude of alternating stress produces an increase in the striation spacing.

Stage III is the terminal propagation phase of a fatigue crack in which the striation

forming mode is progressively displaced by the static fracture modes, such as dimple rupture or cleavage. Therefore stage III fatigue is sensitive to both microstructure and mean stress.

• Decohesive Rupture: When a fracture exhibits little or no macro-plastic deformation and does not occur by dimple rupture, cleavage, or fatigue, is referred to as decohesive rupture (Figure 5.11). This type of fracture is generally the result of a reactive environment or an unique microstructure and is associated almost exclusively with rupture along grain boundaries. Some fractures, such as quasi-cleavage and flutes, exhibit an unique appearance but cannot be readily placed within any of the principal fracture mode.

• Quasi-Cleavage: Quasi--cleavage is a localized, often isolated feature on a fracture surface that exhibits characteristics of both cleavage and plastic deformation (Figure 5.12).

• Flute: Flute exhibits elongated grooves or voids that connect widely spaced cleavage planes. This process is called fluting. Although flutes are not elongated dimples, they are the result of a plastic deformation process (Figure 5.13).

• Tearing Topography Surface: This type fracture occurs in variety of alloy system, including steel, aluminum, and titanium under a variety of fracture conditions such as overload, hydrogen embrittlement and fatigue.

The fracture process seems to a result of a microplastic tearing process that operates on a very fine scale (Figure 5.14 to 5.17). It does not exhibit as much plastic deformation as dimple rupture, although they are often observed in combination with dimples. The fractures are generally characterized by relatively smooth, often flat, areas or facet that usually contain thin tear ridges. Tearing topography surface fractures may be due to closely spaced microvoid nucleation and limited growth before coalescence, resulting extremely shallow dimple.

The characteristics of each fracture mode are tabulated in Table 5.1.

Table 5.1: Summary of Fracture Mode, Characteristics and Possible Formation

Mode	Characteristics	Possible Formation Reasons
Dimple Rupture	Microvoids and Dimples.	Overloading.
Fatigue	Striation.	Repeated or Cyclic Loading.
Decohesive Rupture	No Bulk Plastic Deformation and not from Dimple Rupture, Cleavage or Fatigue.	Reactive Environment or an Unique Microstructure associated with rupture along Grain Boundary.
Quasi-Cleavage	Combined Plastic Deformation and Cleavage.	Localized Fracture Charpy Impact.
Flute	Grooves or Voids Connected Widely Spaced Cleavage Plane.	Model III Shear Load Fracture
Tearing Topography Surface (TTS)	Fine Scale Dimples.	Overloading or Hydrogen Embrittlement and Fatigue.
Cleavage	Flat and Featureless matching surface.	Solid Impact and Stress-Corrosion Cracking.

5.3. Experimental Procedure

Aluminum, steel and titanium were used as sample materials in this study. Each material sample was impinged upon by WJ or AWJ at different parameter combinations. Both a light optical microscope and a scanning electronic microscope were used for observation. However, the use of the light optical microscope was limited, since the lower magnification will lead to an inaccurate observation conclusion (see Figure 5.18 and Figure 5.19). The samples were made in accordance with specifications in Table 5.2:

Some samples have been evaluated at bottom and wall side of the scratches to determine the typical material fracture pattern.

Table 5.2: Sample Material Specification

Sample Number	Materi al	Jet Form	Sapphire size (0.025 mm)	Carbide size (0.025 mm)	Traverse rate (mm./ min)	Stand-off Dist. (mm)	Abrasive Mesh	Abrasive Flow rate (g/min)
1	Al.	WJ	10	63	3810	12.7		
2	Al.	WJ	14		25.4	12.7		
3	Fe.	WJ	10			6.35		
4	Ti.	WJ	14		1270	12.7		
5	Al	WJ	10		*	6.35		
6	Al.	AWJ	10	63	3810	12.7	220	5.94
7	Al.	AWJ	10	63	3810	12.7	80	5.92
8	Ti	AWJ	14	30	1270	12.7	80	2.48

*: 0.5 second interaction

5.4 Results and Discussion

5.4.1 Pure Water Jet

Numerous cavities, as shown on Figure 5.20-Figure 5.22, which are of a typical damage pattern often present in dimple rupture and TTS damage are observed. The size of the cavities is too large compared with the dimple size resulting from the TTS fracture mode. It is reasonable to believe that these cavities were damaged in microscale. Thus in higher magnification of these pictures, non-directional striation and bulk plastic deformation can also be observed (see Figure 5.23-Figure 5.25). The same features were also present in steel samples (see Figure 5.26-Figure 5.28). Considering the damage mechanism associated with this observation, the presence of non-direction striation and plastic deformation suggests fatigue. In titanium samples, less damage can be understood as crack generation due to higher hardness of the property. Less plastic deformation is observed (Figure 5.29 and Figure 5.30).

Observing the SEM pictures in Figure 5.31-Figure 5.33, which represent the aluminum sample surface impinged upon by WJ for 1 second duration, dark trenches, shown in Figure 5.32, indicate the weakening of material on the intergranular boundary and soft part of the material. This weakening differs from the large amount of plastic deformation shown in Figure 5.33. These appearances indicate that the destruction in Figure 5.32 was not fully developed.

A series of pictures which use material sample 3, steel electrodeposited by copper, is used to demonstrate the cross section of the generated subsurfaces (Figure 5.35-Figure 5.40). The description of the cross-section is shown in Figure 5.34. Cracks on the machining surface and subsurface can be observed.

5.4.2 Abrasive Water Jet

An aluminum sample impinged upon by AWJ is shown in Figure 5. 41 to Figure 5.45. A typical pattern to be found in these pictures is the randomly distributed flat and featureless surfaces; neither plastic deformation nor striation can be observed. The same pattern also can be observed in a titanium sample which is shown at Figure 5.47 to Figure 5.48.

5.5 Conclusion

The appearance in samples prepared by WJ suggests that the cutting mechanism is not completely uniform across the cavity diameter. Rather the cutting appears to be greater near the edge, and the bottoms of the cavity are irregular, suggesting that the cutting may have taken place locally at different rates. The nondirectional striation is generally observed in fatigue loading pattern material. The undercut mechanism may be considered to be based on erosion of grain boundaries and inclusions, the weakest in the metallic system. Considering the striations and recalling the extrema shown in Figure 4.11, stress wave resonance can be account for WJ-workpiece interaction. These stress waves propa-

gated in the material gradually reduce the endurance limit of the material and enhance fatigue effect. Undercut in the subsurface occurs at the frequency resonance point in the material and cracks on the cavity surface, are due to microscale loading on material surfaces. Such microscale loading suggests the cutting mechanism of WJ-workpiece interaction to be cavitation erosion. Comparing the fractographies of the workpiece in the course of WJ interaction with typical cavitation erosion fractography, see Figure 5.49, where great similarity was observed.

In the case of AWJ machining, flat featureless surfaces suggest the damage mechanism as cleavage resulting from solid particle erosion.
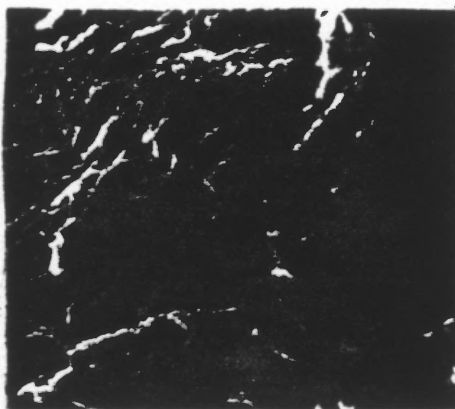
Figure 5.1: Example of dimple rupture mode of fracture.
Note: Large and small dimples in the fracture surface of a tool steel saw
disk. The extremely small dimples at top left are nucleated by numerous,
closely spaced particles.
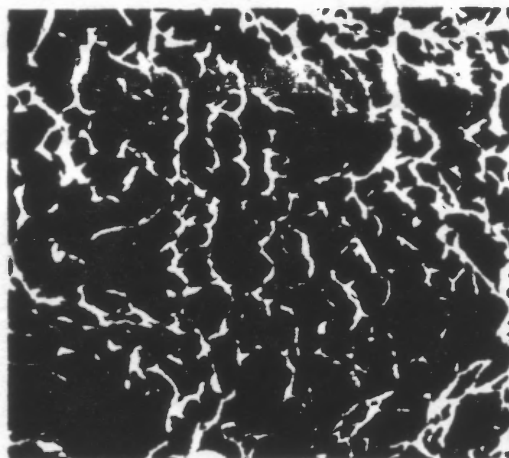
Figure 5.2: Conical equiaxed dimples Shallow dimples in a in a spring steel specimen.
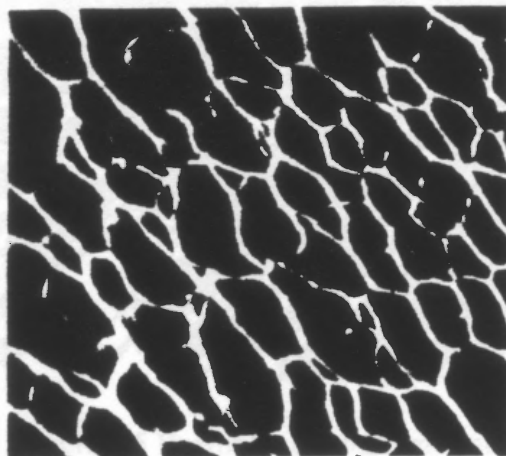
Figure 5.3: Shallow dimples in a maraging steel specimen.
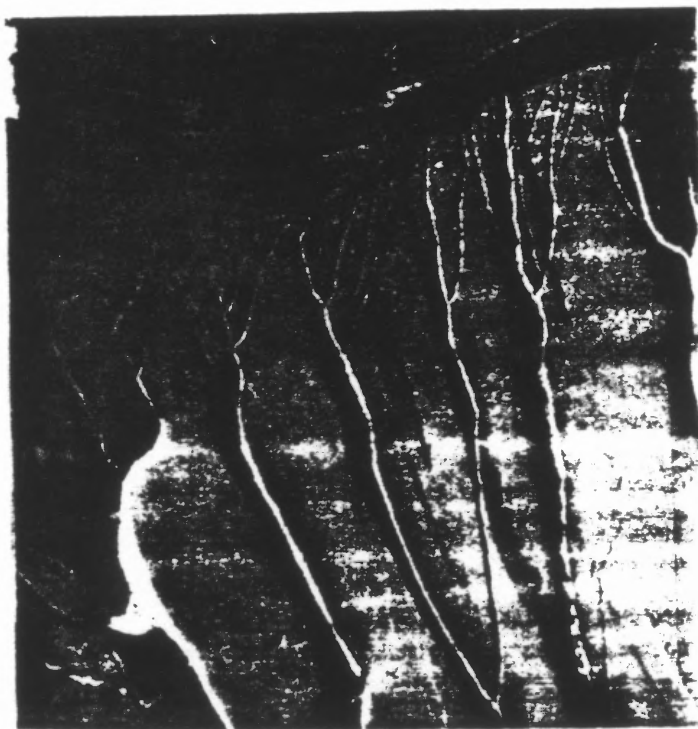
Figure 5.4. Examples of cleavage fracture.
Cleavage steps, river pattern and twist boundary on an alloy fractured by impact.
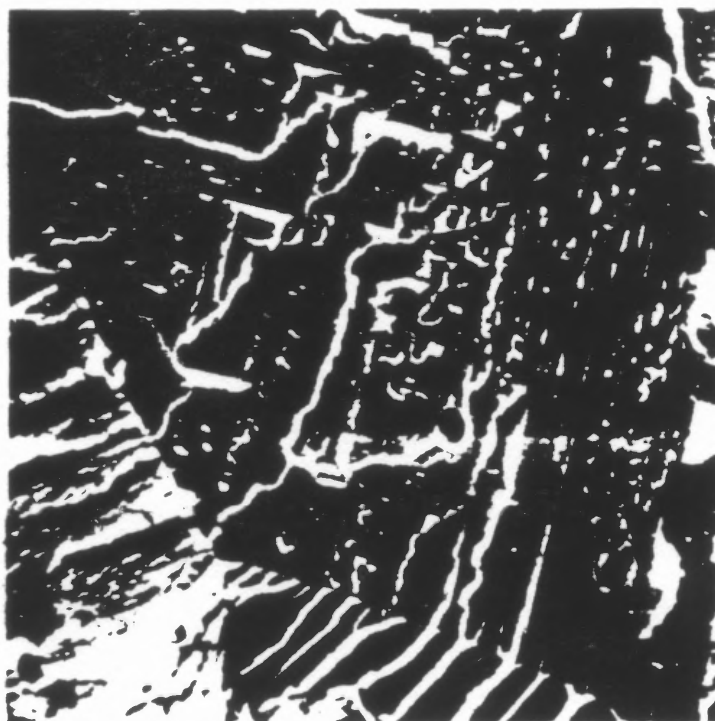
Figure 5.5 Examples of cleavage fracture.
Tongues fractured on a steel sample by cleavage.

Figure 5.6. Cleavage steps in an Cu-Au alloy fractured by transgranular stress-corrosion cracking.

Figure 5.7: Stage I fatigue fracture. On cast alloy.

Figure 5.8. Stage I fatigue fracture. On ASTM F75 alloy.
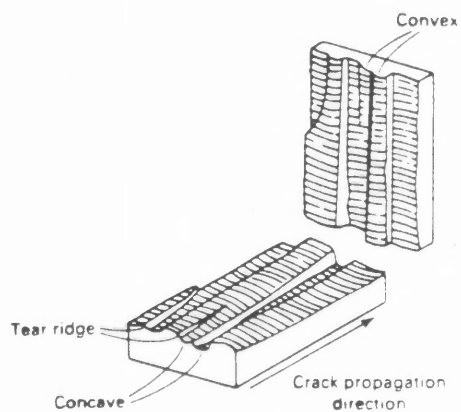
Figure 5.9. Schematic illustrating fatigue striation on plateaus.

Figure 5.10. Variations in fatigue striation.
An increase in striation spacing due to a higher alternating stress.
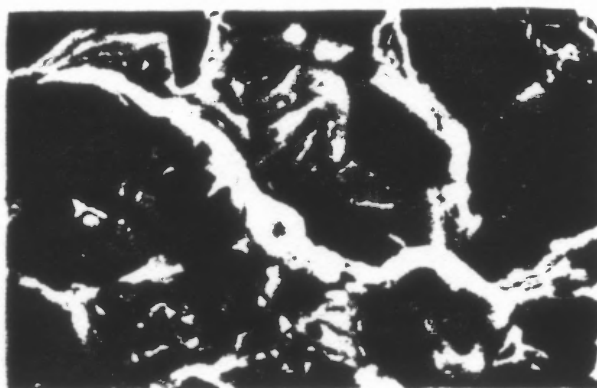
Figure 5.11. Decohesive rupture in an AISI 8740 steel nut due to hydrogen
embrittlement.
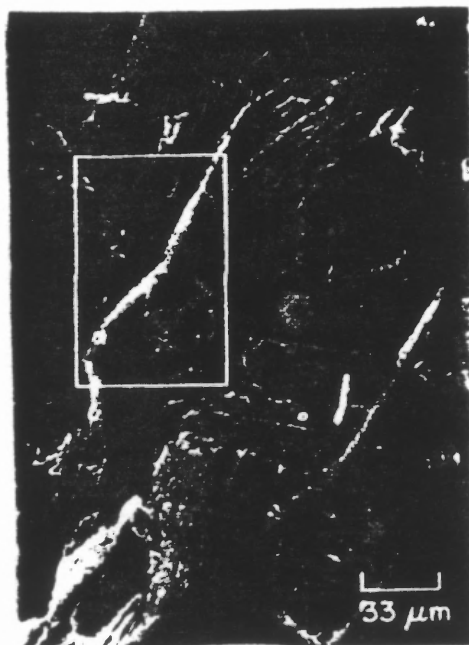
Figure 5.12 Examples of quasi-cleavage Charpy impact failure in a steel specimen.
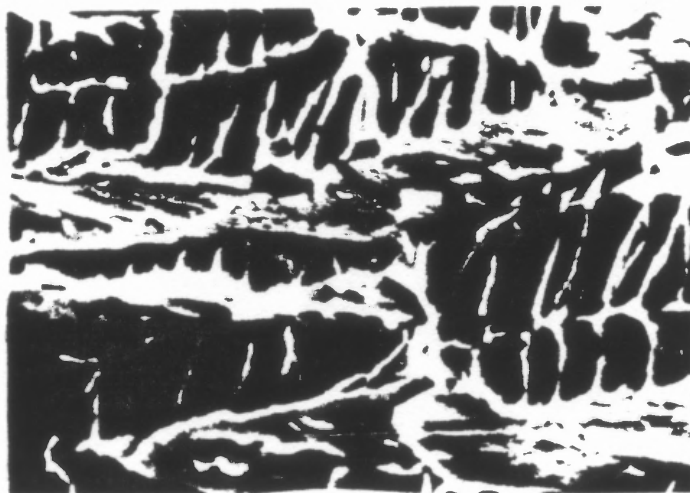
Figure 5.13. Examples of fluting. Flutes and Cleavages on a steel specimen
resulting from sustained load cracking vacuum
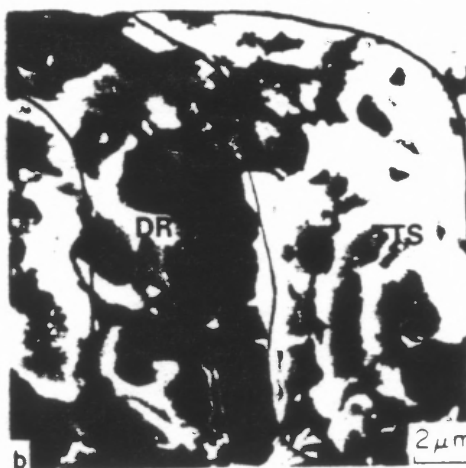
Figure 5.14. Appearance of TTS fracture in Appearance of TTS fracture in HY-130 steel.

Figure 5.15. Another view of appearance of Figure 5.14
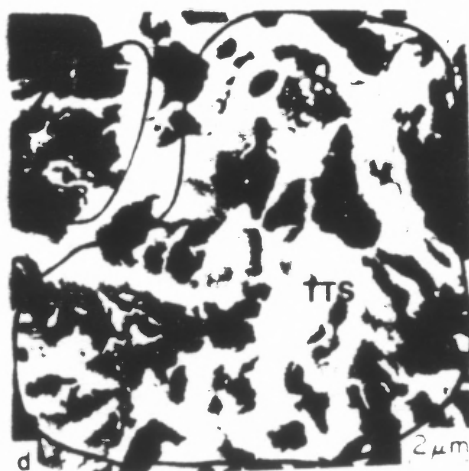
Figure 5.16. Another example of TTS fracture in HY-130 Steel.
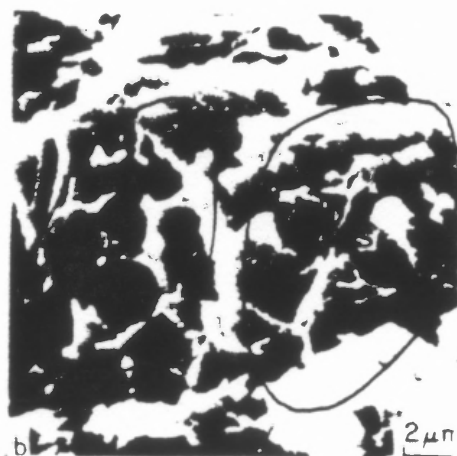
Figure 5.17. Appearance of TTS fracture.
Dimple rupture and TTS fracture in a quenched and tempered HY-130 steel.

Figure 5.18. Aluminum plate under WJ and AWJ. Magnification: 96.

	WJ	AWJ
Sapphire size(mm)	0.254	0.254
Carbide size(mm)		1.6
Stand-off Dist.(mm)	12.7	12.7
Abrasive mesh		80
Abrasive flow rate(g/min)		5/92
Jet speed(inch/min)	150	150
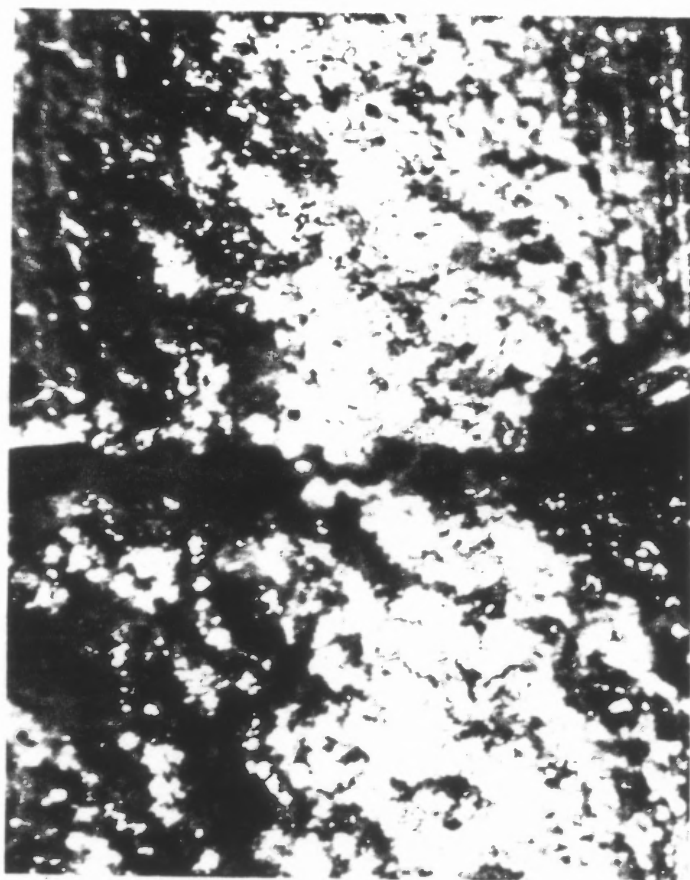
Figure 5.19. Aluminum plate under WJ and AWJ. Magnification: 96.

	WJ	AWJ
Sapphire size(mm)	0.254	0.254
Carbide size(mm)		1.6
Stand-off Dist.(mm)	12.7	12.7
Abrasive mesh		80
Abrasive flow rate(g/min)		5/92
Jet speed(inch/min)	125	125
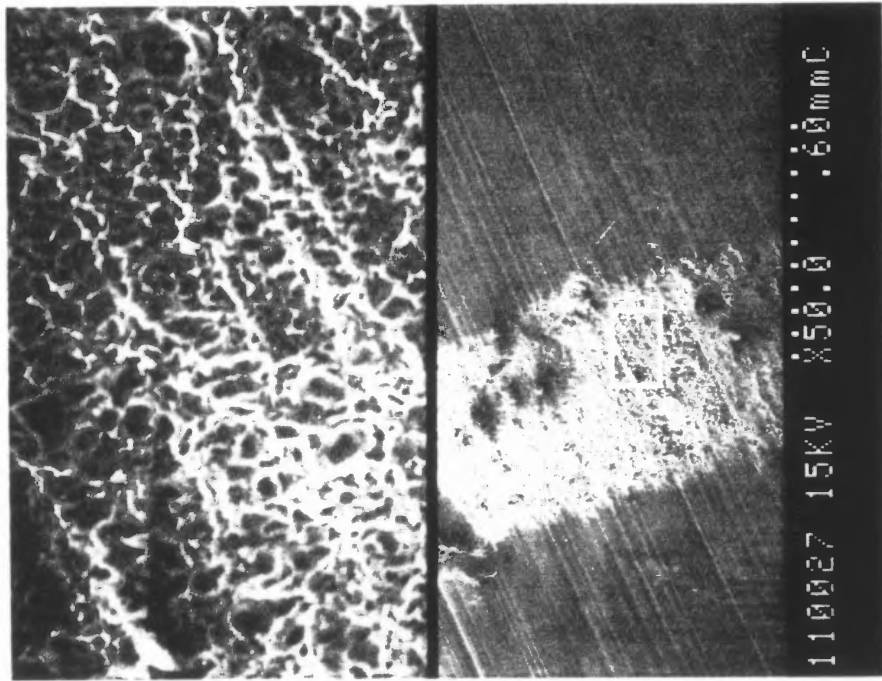
Figure 5.20: Sample 1 Aluminum Plate Under WJ cutting.
Note: Compare with Figure 5.2. Cavities Structure is present.
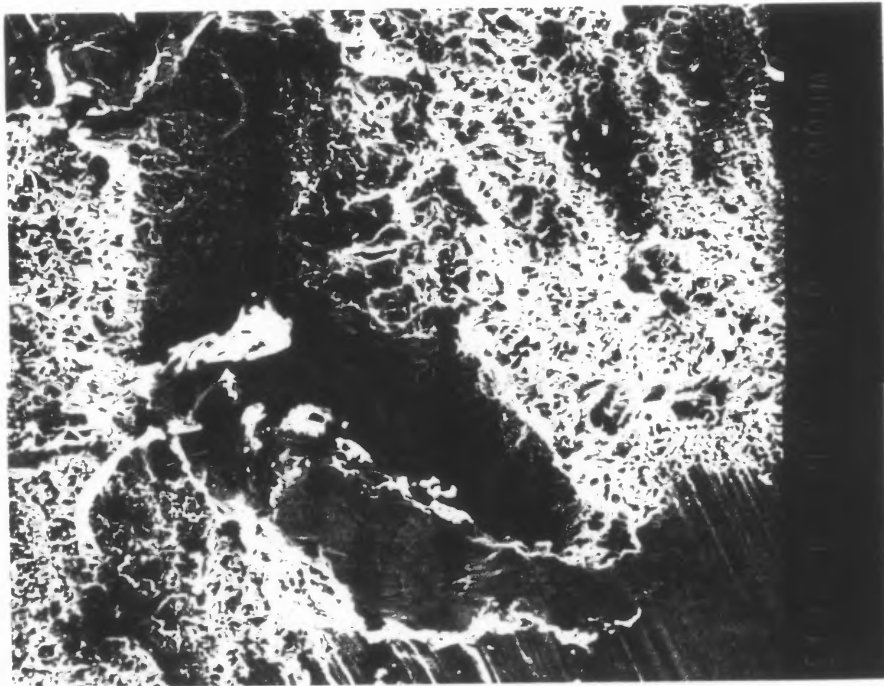
Figure 5.21 Sample 1 Aluminum plate under WJ cutting.
Note: A flat surface may be due to water contaminated dust impact.
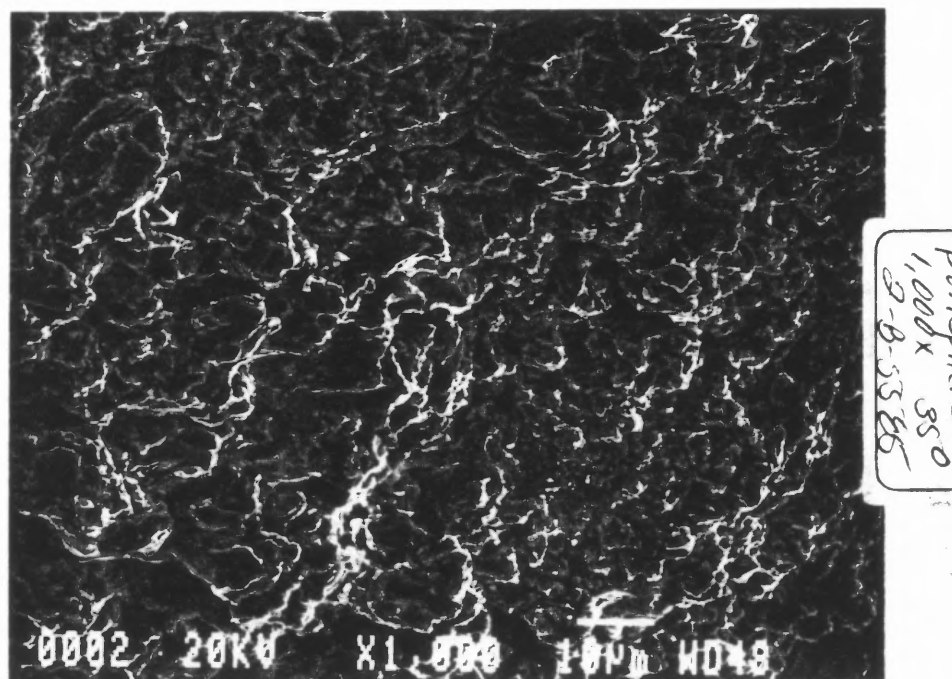
Figure 5.22. Sample 1 Aluminum plate under WJ cutting.
Note: Clear cavities are shown in higher magnification.
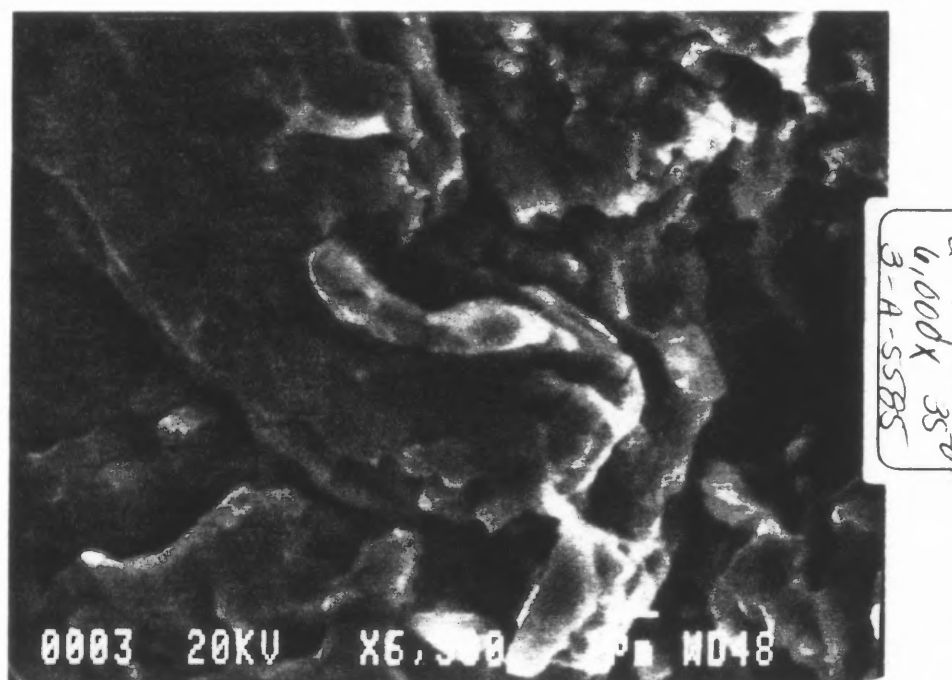
Figure 5.23. Sample 2 Aluminum plate under WJ cutt.
Note: Cavities and plastic deformation are present.
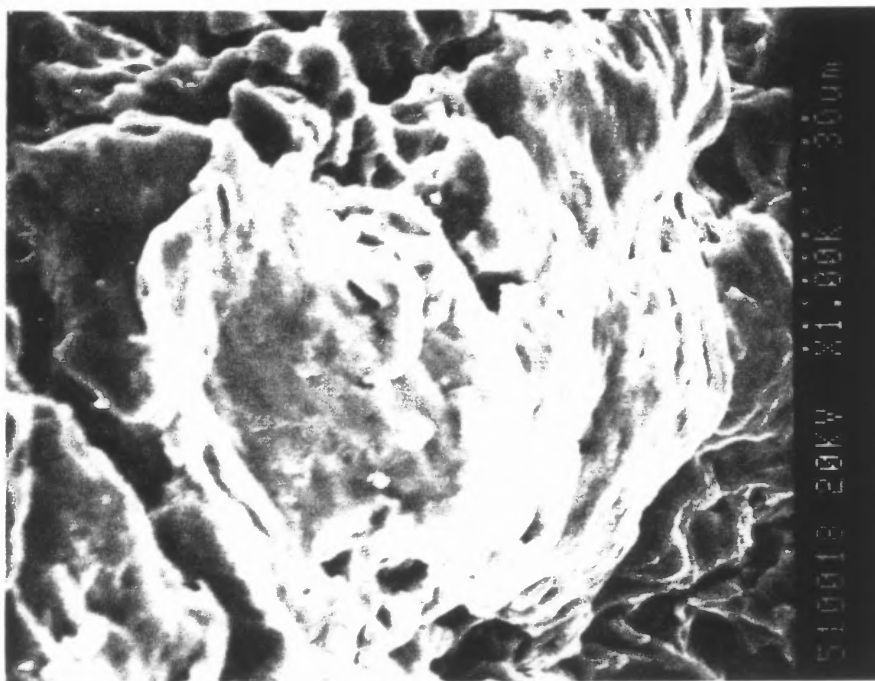
Figure 5.24. Sample 2 Aluminum plate under WJ cutting.
Note: Non-direction striation are shown.

Figure 5.25. Sample 2 Aluminum plate under WJ cutting.
Note: Plastic deformation in the edge of the flat surface.
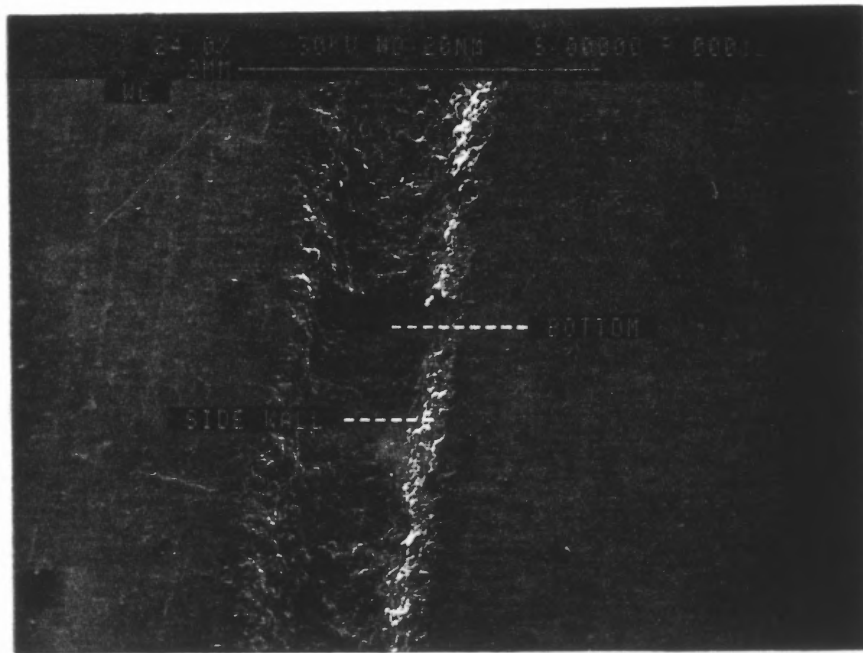
Figure 5.26. Scratch processed sample 3 Steel plate.
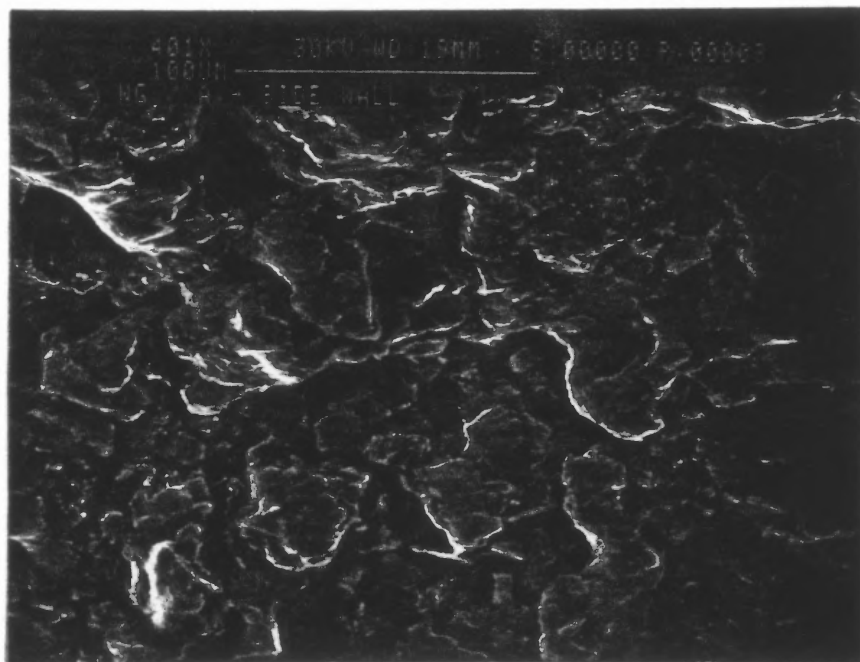
Figure 5.27. Wall side of the Sample 3 steel plate under WJ cutting.
Note the dark trenches area caused by the erosion wear. With repeated impingements at
the same point water undercut and spall particles of the material.
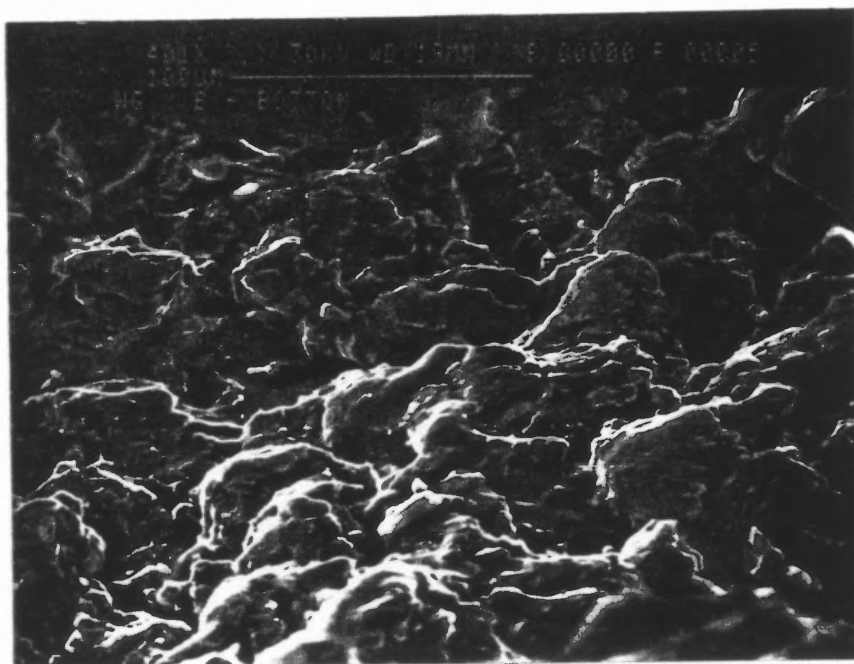
Figure 5.28. Bottom side of the Sample 3 steel plate under WJ cutting.
Note: The same features as in Figure 5.27.
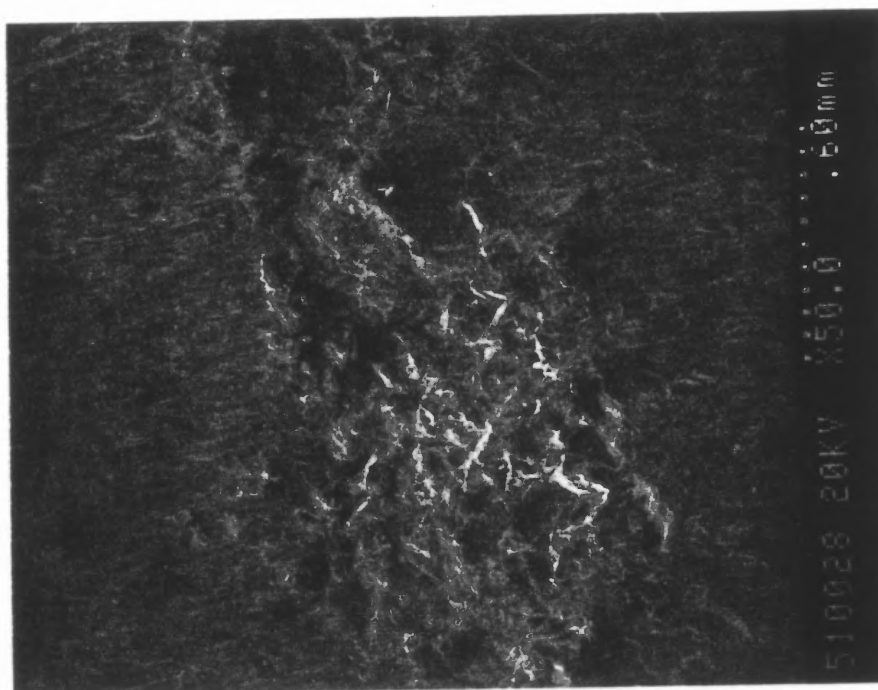
Figure 5.29. Sample 4 Titanium material under WJ cutting.
Note: Damage state is less severe than Figure 5.28
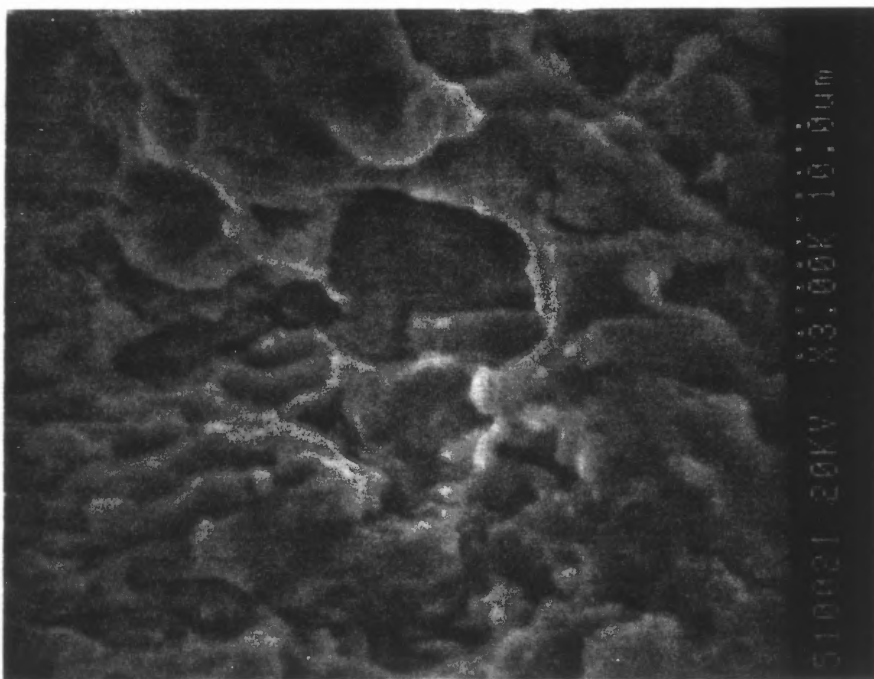
Figure 5.30. Sample 4 Titanium plate under WJ cutting.
Note: Some cavities are clearly shown.
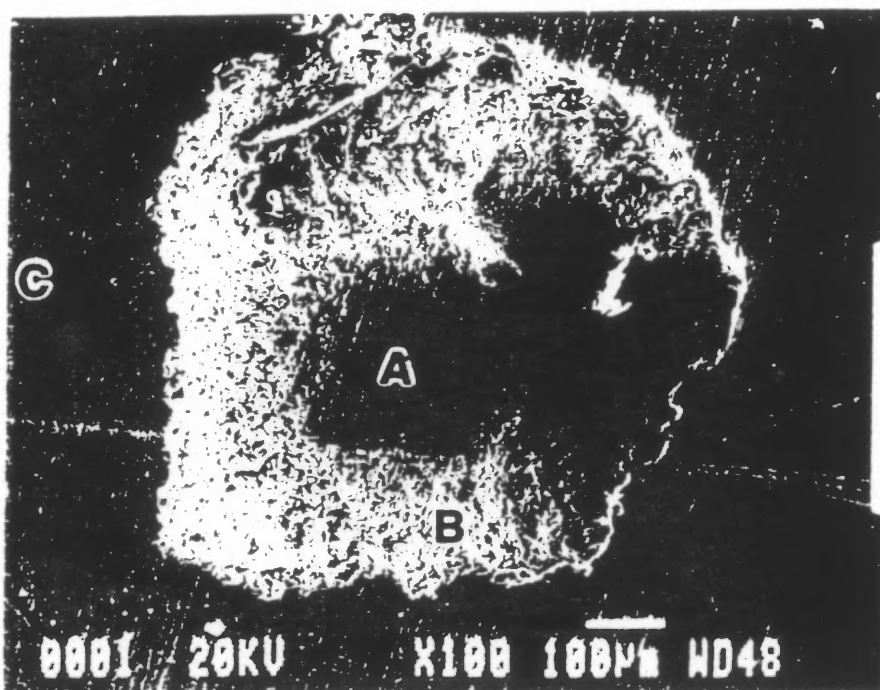
Figure 5.31. Sample 5 Aluminum plate under WJ cutting.
Note: Region B represent wall side of the cavity. Region A represent bottom. The damage
state in B is much severe than A.
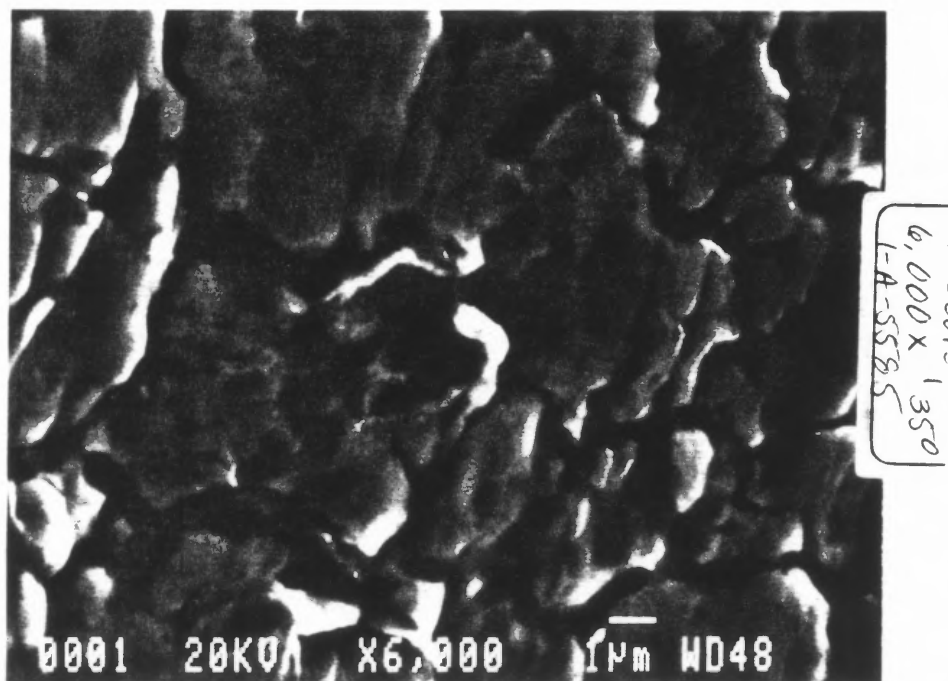
Figure 5.32. Sample 5 Aluminum plate region A.
Note: Dark trenches.(furrows)
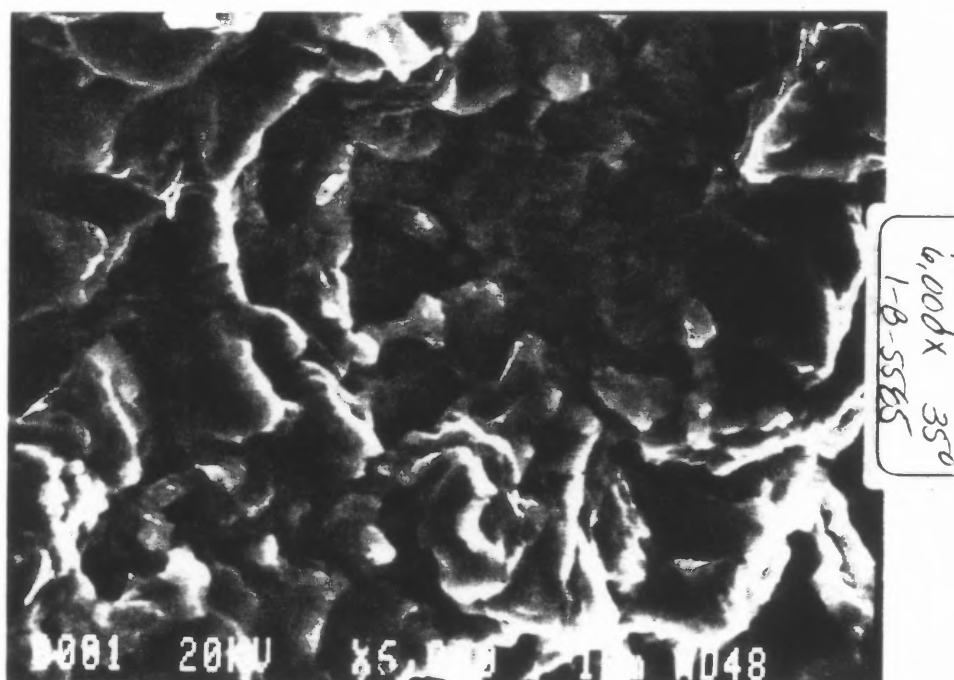
Figure 5.33. Sample 5 Aluminum plate region B.
Note: The different pattern as in Figure 5.32 and large amount of plastic deformation.
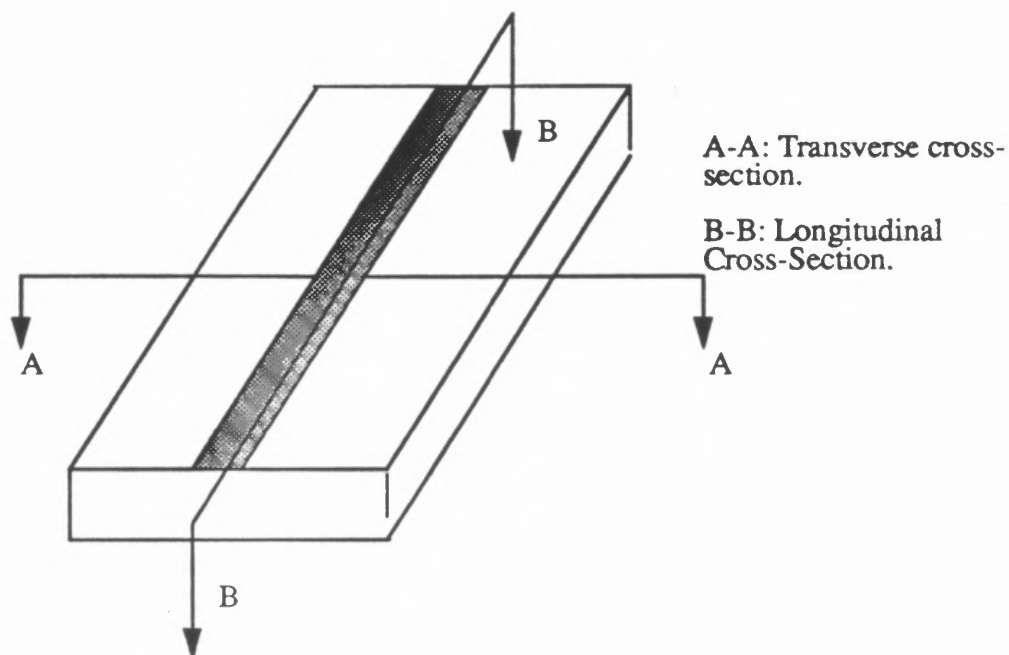
Figure 5.34. Description of Cross-Section From Figure 5.35-5.40

A-A: Transverse cross-section.

B-B: Longitudinal Cross-Section.
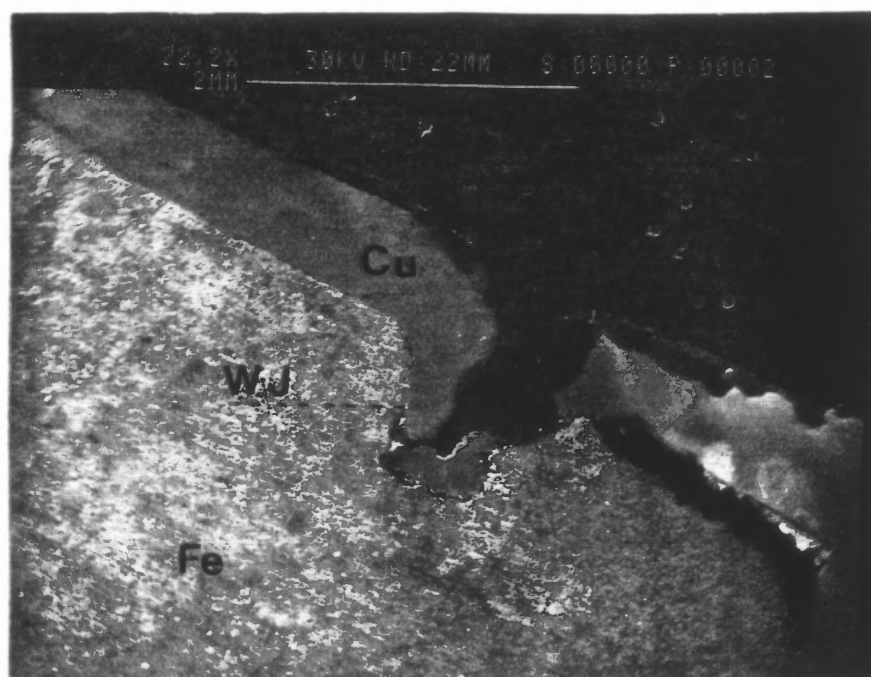
Figure 5.35. Sample 3 transverse Cross-Section of scratch processed by WJ. Description of the edge protection.
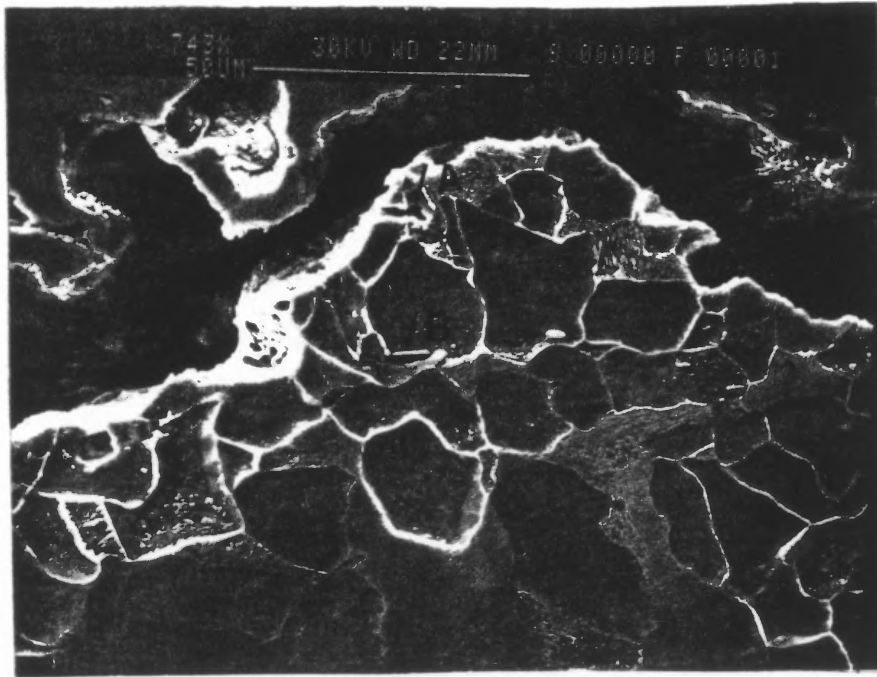
Figure 5.36. Sample 3 bottom side of transverse cross-section of the scratch
Note: Arrow A indicate crack at the cutting edge.
Arrow B indicate Intercrystalline crack at subsurface.
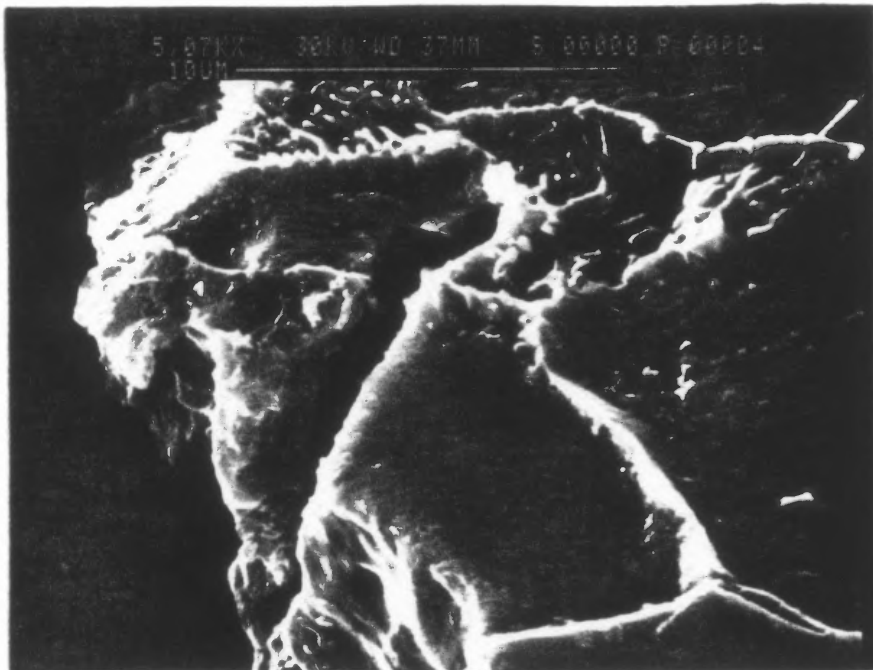
Figure 5.37. Sample 3 higher magnification of A in Figure 5.36.
Note: Erosion wear pattern.
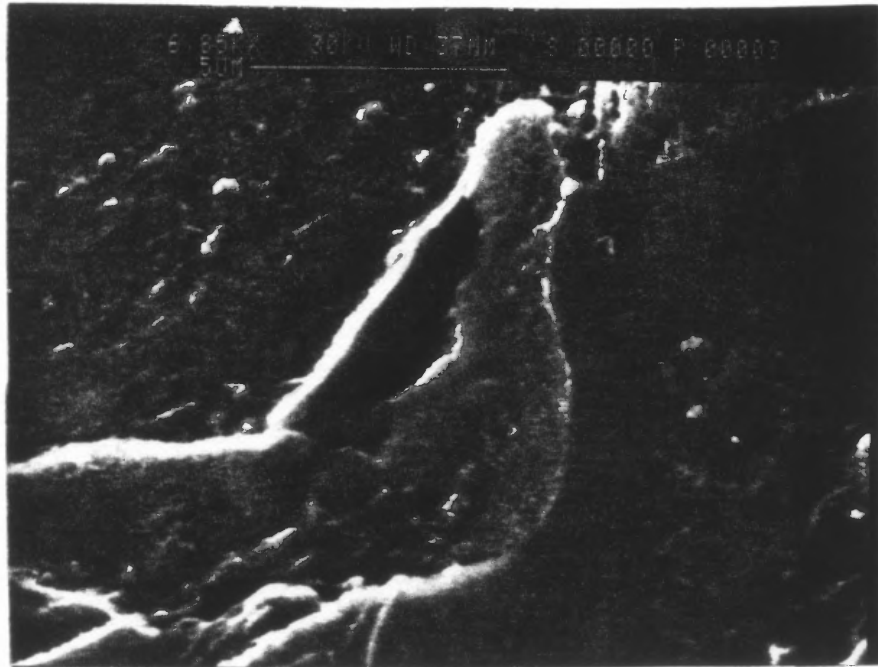
Figure 5.38. Sample 3 higher magnification of A in Figure 5.36.
Note: Typical crack failure.
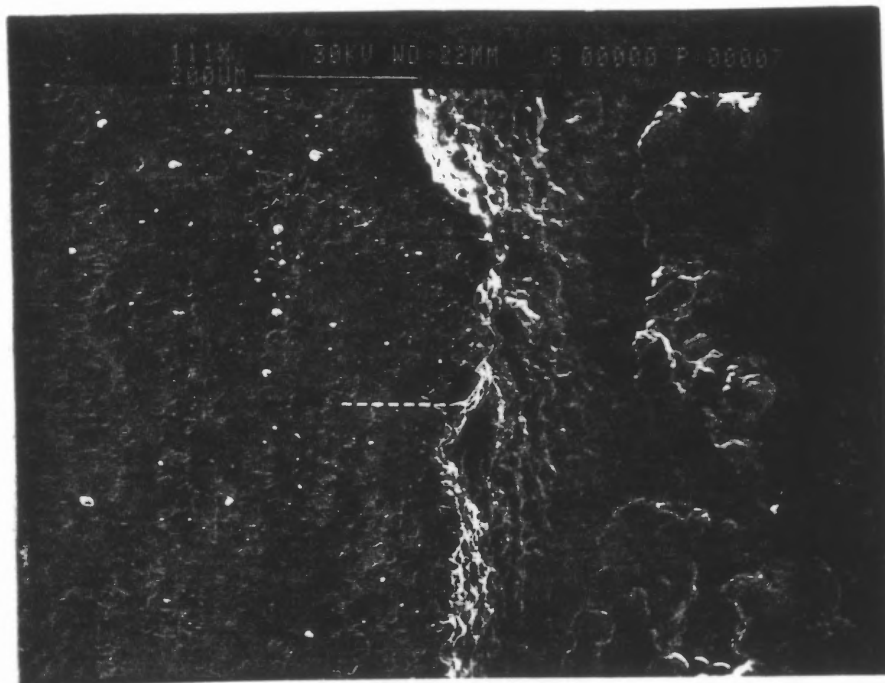
Figure 5.39. Sample 3 longitudinal cross-section of the scratch
Note: Typical erosion pattern in dotted line area.
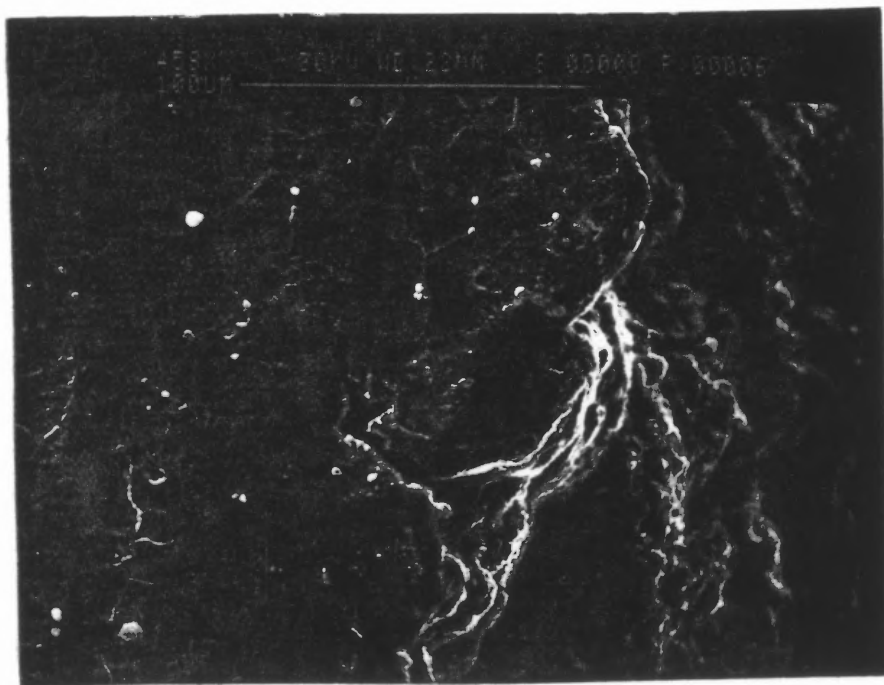
Figure 5.40. Sample 3 higher magnification of Figure 5.39.
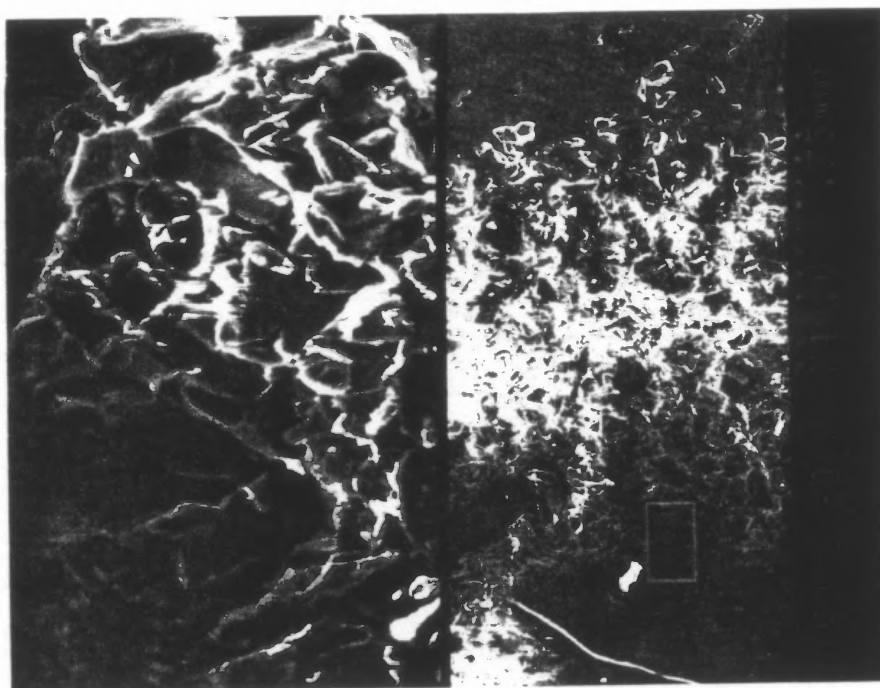
Figure 5.41. Sample 6 Aluminum plate under AWJ.
Note: The flat and featureless surface in upper pictures.
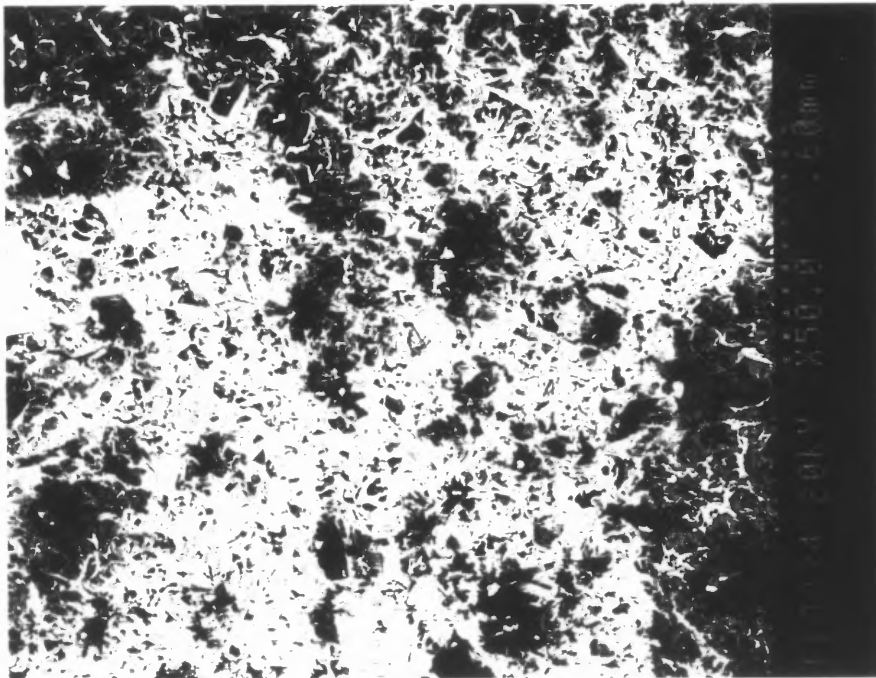
Figure 5.42. Sample 7 Aluminum plate under AWJ.
Note: Abrasive particles embedded and solid particles impact surfaces.
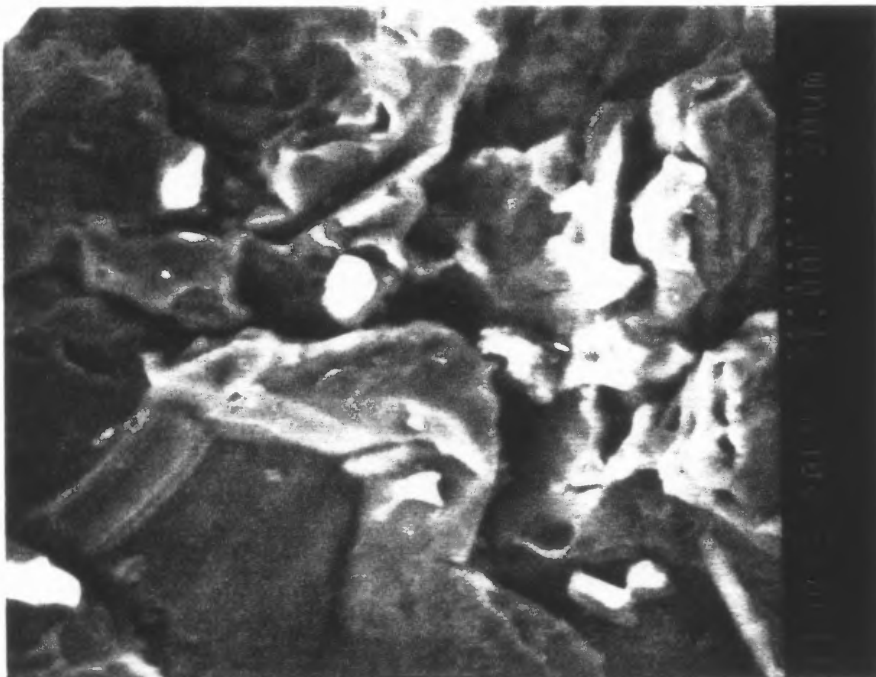
Figure 5.43. Higher magnification of Figure 5.42.
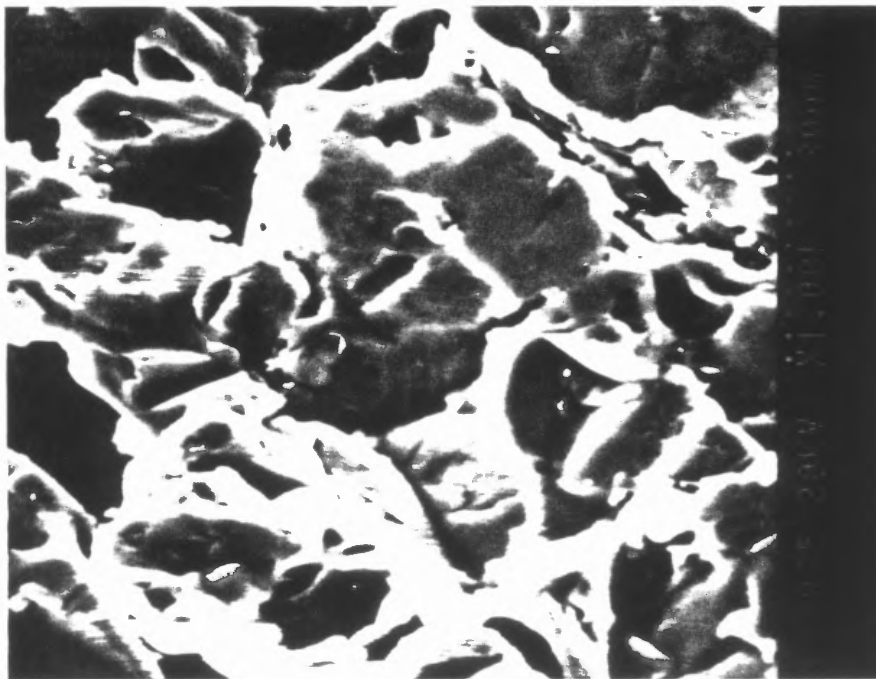
Figure 5.44. Sample 6 Aluminum plate under AWJ.
Note: The flat surfaces.

Figure 5.45. Higher magnification of Figure 5.44.
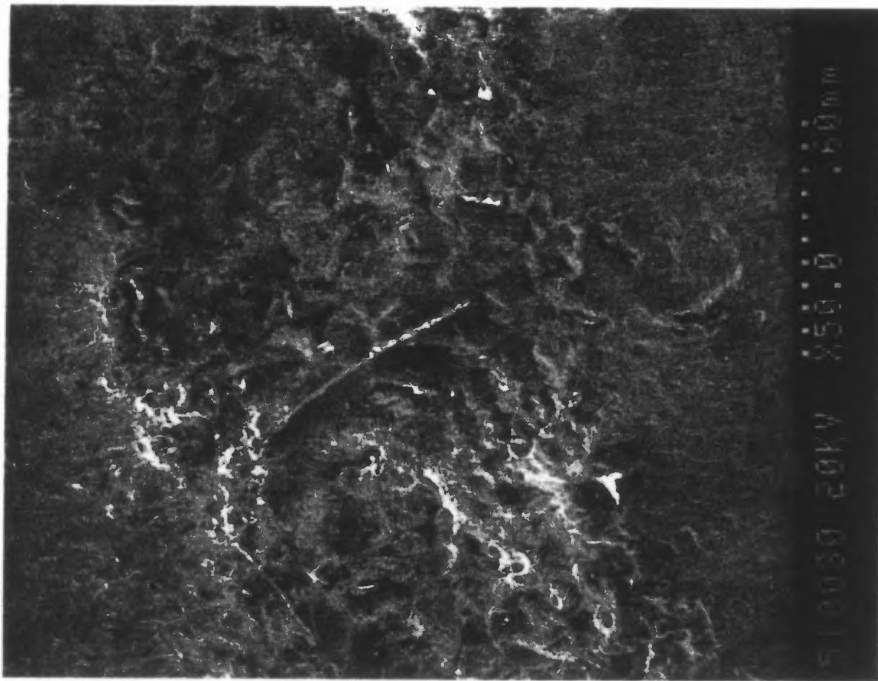
Figure 5.46. Sample 8 Titaninum plate under AWJ.
Note: Damage state is more severe than 5.29.
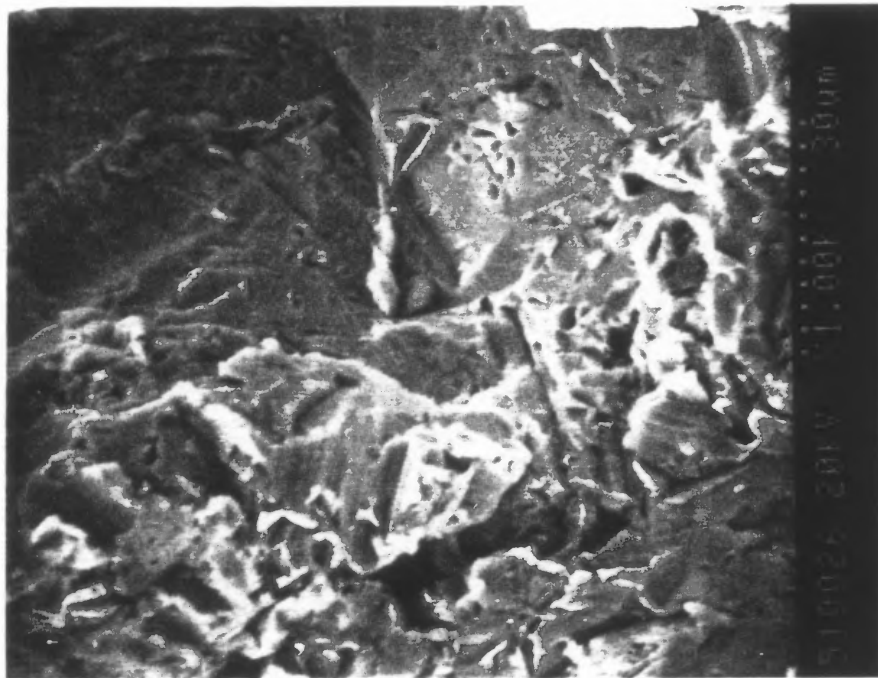
Figure 5.47. Higher magnification of Figure 5.46.
Note: The flat and featureless surfaces as in Figure 5.41.
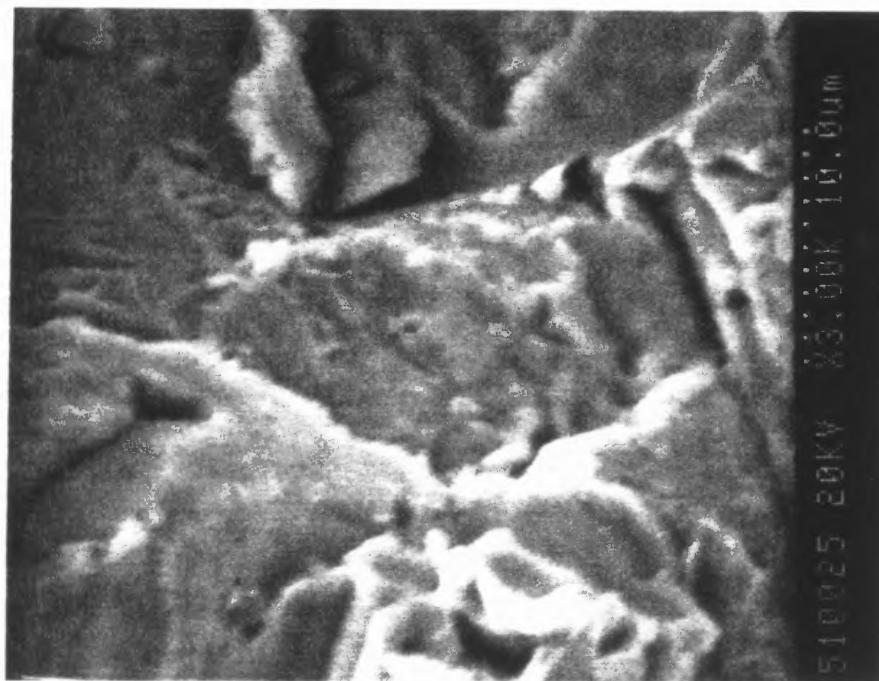
Figure 5.48. Higher magnification of Figure 5.46.
Note: The flat surfaces.
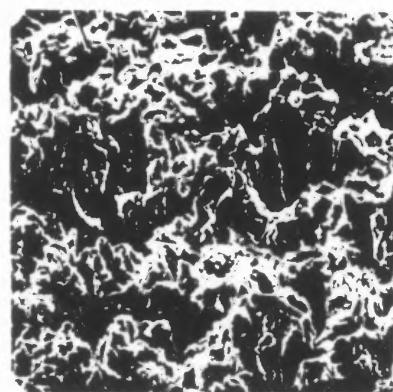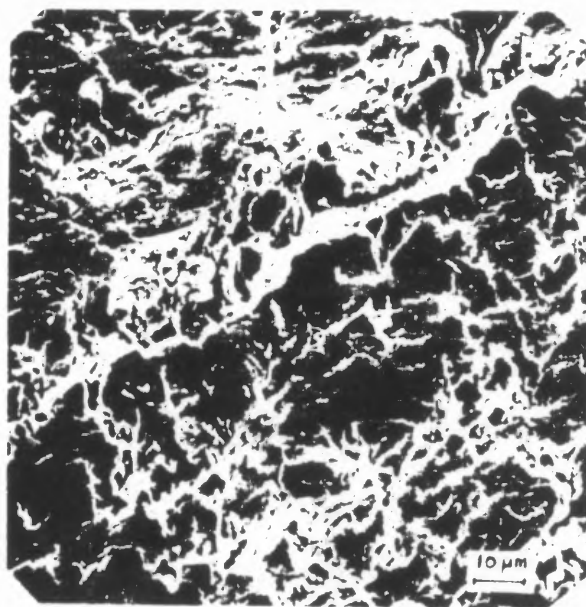
Figure 5.49 Typical Erosion Cavitation Fractography.

CHAPTER 6

STRESS WAVE FREQUENCY MEASUREMENT

6.1 Introduction

The study presented in previous chapters, Chapter 4 and Chapter 5, imply that the damage mechanism on ductile material associated with WJ interactions is cavitation erosion. WJ composed of numerous air cavities and droplets impinge on material surfaces generating pulses of stress waves into these materials. These stress waves reduce material endurance limit and enhance fatigue effect. The objective of this study is to identify the existence of the stress waves and measure their frequency.

The response of materials and structures to intensive impulsive loading can be roughly divided into three categories. For loading conditions that result in stresses below the yielding point, materials behave elastically and follow Hook's law. As the intensity of the loadings are increased, material is driven to the plastic range. The behavior here involves large deformation, heating, and failure of colliding solids through a variety of mechanisms. With still further increase in loading intensity, pressures are generated which exceed the strength of the colliding solids by several orders of magnitude, which, in effect, behave hydrodynamically.

For low intensity excitation, both the geometry of the entire structure as well as the nature of the material from which it is made play a major role in resisting external forces. As the loading intensity increases, the response tends to become highly localized and is more affected by the constitution of the material in the vicinity of local application than by the geometry of the total structure.

These external loadings applied on material surface will generate stress waves

propagating into material, which is a dynamic process; that is their intensity varies with time. Both the maximum intensity and the rate of change in intensity with time spread over wide measurement ranges and then often require highly specialized equipments and mathematical modeling for the precise determination.

This stress waves propagation process is assumed to be a stationary random process. However, a stationary random process is only an idealized concept. It is nevertheless useful in many applications to assume that certain phenomena may be modeled by this process. In most applications to date the only characteristics estimated have been the mean and the second order statistics given by either the auto-correlation function or the mean square spectra density. One of the available numerical modeling of this process is Fourier Transformation.
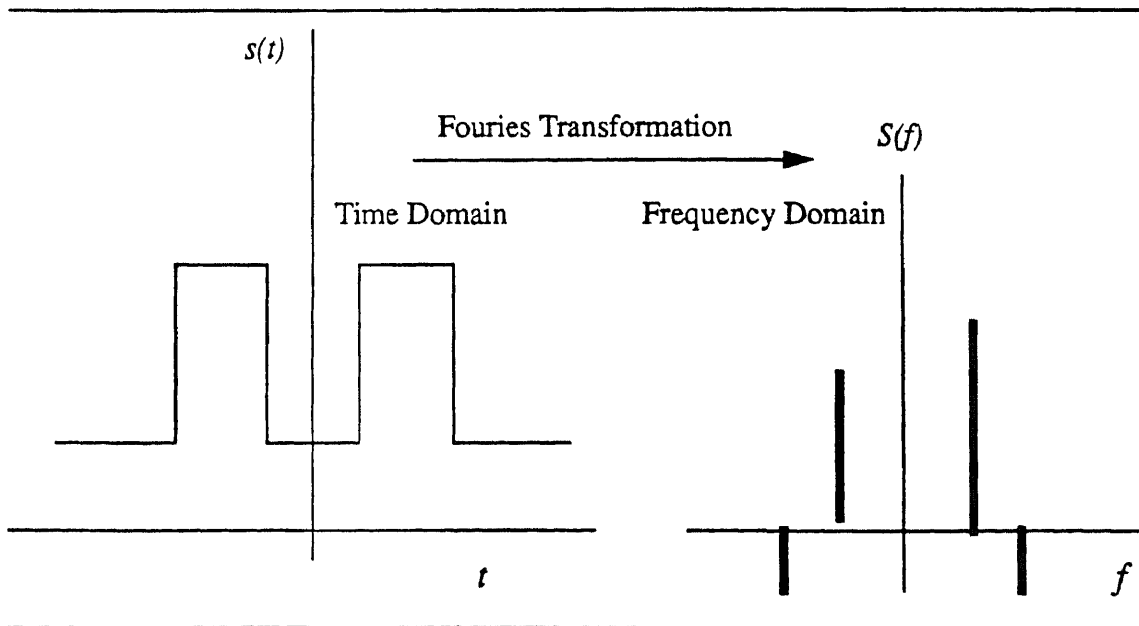
Figure 6.1. Demonstration of Fourier Transformation Effect.

The objective of Fourier Transformation is to convert signal in time domain to frequency domain. Mathematically, this relationship can be stated as [49]:

$$F(y) = \int_{-\infty}^{\infty} f(t) e^{-jty} dt \qquad (6.1)$$

F(y):Fourier Transfor of *f(t)*.

f(t): Waveform to be decomposed.

j: $(-1)^{1/2}$

y: frequency.

An example of a square wave function is illustrated in Figure 6.1.

Consider the pressure deviation on a plane sound wave varies with time as *f(t)*.

The instantaneous rate of energy transfer across unit area may be shown to be proportional to $f^2(t)$, if *f(t)* satisfies Equation (6.2) as:

$$\left(\langle f^2(x) \rangle = \lim_{X \to \infty} \frac{1}{2X} \int_{-X}^{X} |f(x)|^2 dx \right) < \infty \qquad (6.2)$$

Such functions are often called finite power signal since a finite mean rate of energy transfer in a system is often represented by such a function. For functions satisfy Equation(6.2), a quantity called the power spectrum, $P_f(y)$, is defined to compare the energy of waves propagating in material.

$$P_f(y) = \lim_{X \to \infty} \frac{1}{2X} F^2(y) \qquad (6.3)$$

As the integrated value of the energy spectrum over all frequencies is proportional to the total energy transfer in an excitation, the integrated value of a power spectrum can also match the mean rate of the energy transfer.

However, careful inspection of Equation (6.1) reveals that if there are N data points of the function $s(t)$, then computation time is proportional to N^2, the number of multiplications, if the amplitude is to be determined.

Fast Fourier Transformation developed in 1965 by Cooley and Tukey [50] is a computation algorithm which can reduce the computing time of Equation (6.1) from N^2 to $NLog_2(N)$.

In this study, a computer Fast Fourier Transformation program is developed and used to convert the voltage signal of transducers in time domain to frequency domain. The power spectrum, Equation (6.3), is used to compare the signal amplitude distribution.

6.2 Experimental Setup

Two transducers were used in this experiment. A Kistler accelerometer, 5 KHz Model 9042a, was used to measure the excitation in low frequency domain and an ultrasonic transducer, Krautkramer Branson 5 MHz narrow band, was used for the high frequency signal. Aluminum and steel plates were used to be the principle medium for the wave propagation. Both the transducers were installed on the bottom of the plate and oil has been applied as the couplant between aluminum plate and ultrasonic transducer.

The impingement was carried out at a normal angle and 45° angle with a nozzle diameter of 0.0254 mm and stand-off distance of 6.35 mm. The temporal signal from both sensors were received by the digital oscilliscope and then transformed into frequency domain by Fast Fourier Transformation program. In order to demonstrate that the observed stress waves are the result of the jet-material interaction, the measurement was carried with the jet impinging directly above and on the vicinity of the top of the transducer. The sketch of experimental setup is shown in Figure 6.2.

The signal received from transducer is transferred to computer for power spectrum calculation based on the FFT algorithm.
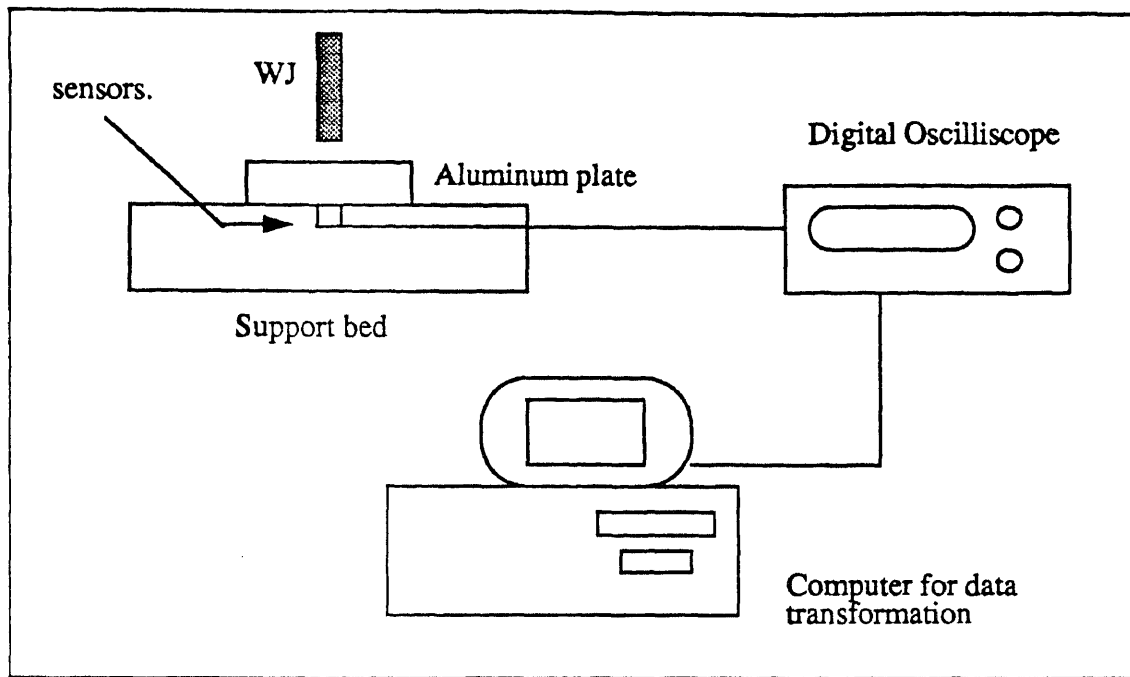
Figure 6.2. Experimental setup of the wave propagation measurement.

6.3 Experiment Results and Discussions

Two transducers were used in this study. A 5 KHz Piezoelectric transducer was using to measure the frequency in the low frequency domain. For acoustic frequency, 5 MHz ultrasonic transducer was adopted.

6.3.1 Low Frequency Response.

• Effect of Propagating mediums.

The frequency and power spectrum on different materials are present in Figure 6.3 to Figure 6.8. WJ was first impinged on supporting bed to evaluate the structure vibration frequency (Figure 6.3 and Figure 6.4), which show an approximately 500 HZ frequency with spectrum in the order of 10^{-2}. Comparing Figure 6.5 with Figure 6.6 and Figure 6.7 with Figure 6.8, the wave energy propagating in steel plate is smaller than in aluminum plate. This can be explained as the steel plate possesses a high damping effect and reduce

the propagating energy. Cross examination of these graphs and delete the effect structure vibration induced by the impingement, a frequency of about 3 KHz is observed for the direct impingement.

• Effect of Impact Angle and Stand-off Distance.

The inclined impact angle significantly generates many different waves propagating to many directions in material, which can be classified as noise by comparing their amplitudes with the amplitude of the wave generated by normal impingement. Comparing Figure 6.9 with Figure 6.10, Figure 6.11 with Figure 6.12, and Figure 6.13 with Figure 6.14, normal impact generates the largest power spectrum, which presents the principle wave propagating in the material a longitudinal wave.

Comparing Figure 6.10, Figure 6.12, and Figure 6.14, larger stand-off distance generates more wave frequencies and less power spectrum. This can be explained by the larger stand-off distance is composed of more water droplets and randomized the frequency distribution.

6.3.2. Acoustic Wave Frequency Response

A calibration curve, shown in Figure 6.15, has been constructed to include the boundary conditions of the transducer-wire-plate system. The structure acoustic resonance frequency was obtained by the impingement of the jet upon supporting bed and present in Figure 6.16, which demonstrates a neglectable power spectrum.

• Effect of impact angle and stand-off distance.

The inclined impact jet also generates some noise in the material, present in Figure 6.17 to Figure 6.22, as explained in low frequency measurement. However, a constant wave frequency of approximately 3 MHz is present.

A larger stand-off distance also presents a smaller power spectrum as present in low frequency measurement.

6.4 Conclusion

The frequency measured from the accelerometer, approximately of 3 KHz, is observed to be the signal generated at the bottom of the plate while acoustic wave frequency, 3 MHz, is measured at the top of the plate. This demonstrates a large number of impact loading on the material surfaces and propagating into the material, which resulting a 3 KHz frequency at the bottom of the plate before these decaying below threshold measurable value.

These two frequencies are used to construct the boundary conditions in the numerical simulation.

Figure 6.3

Figure 6.4

Spectrum Analysis

5 KHZ Transducer, #10 Nozzle, 0.25" S.D., 0.25" Aluminum Plate

Directly Received

Figure 6.5

Spectrum Analysis

5 KHZ Transducer, #10 Nozzle, 0.25" S.D., 0.25" Steel Plate

Directly Received
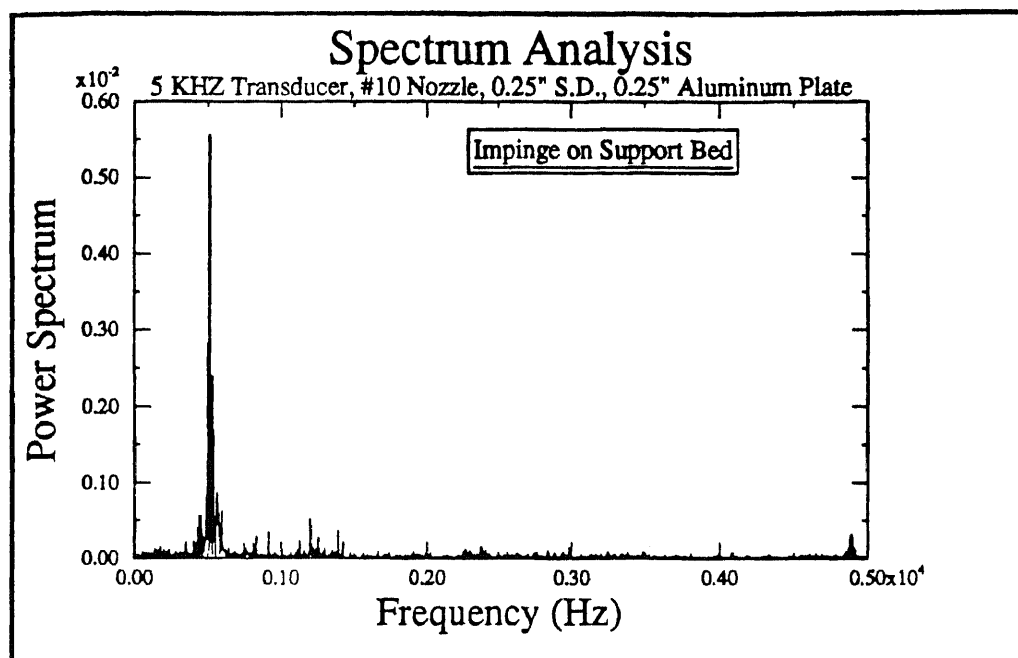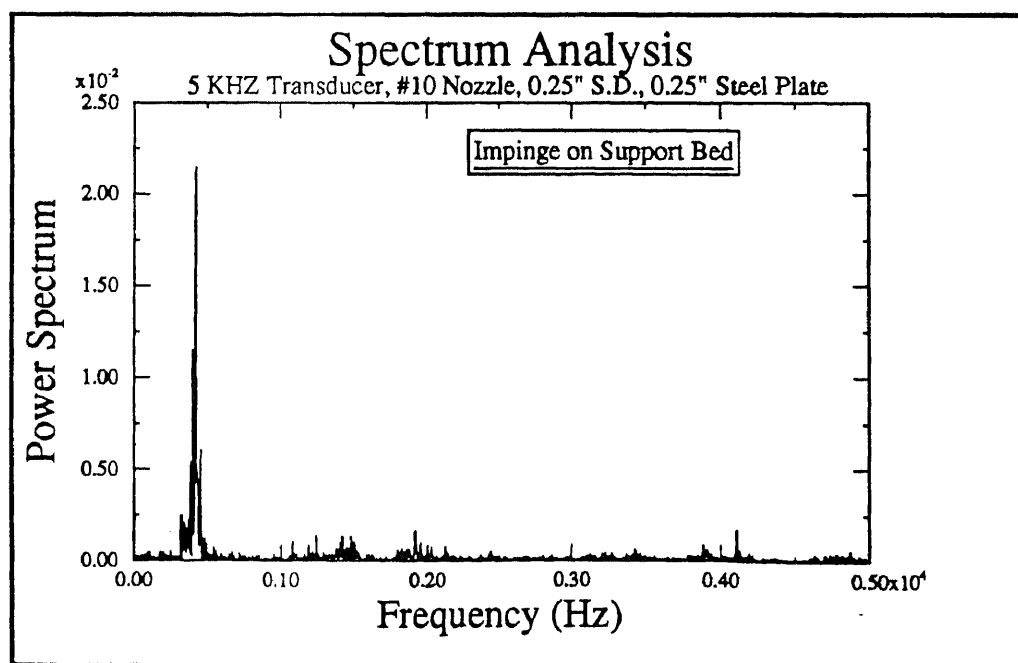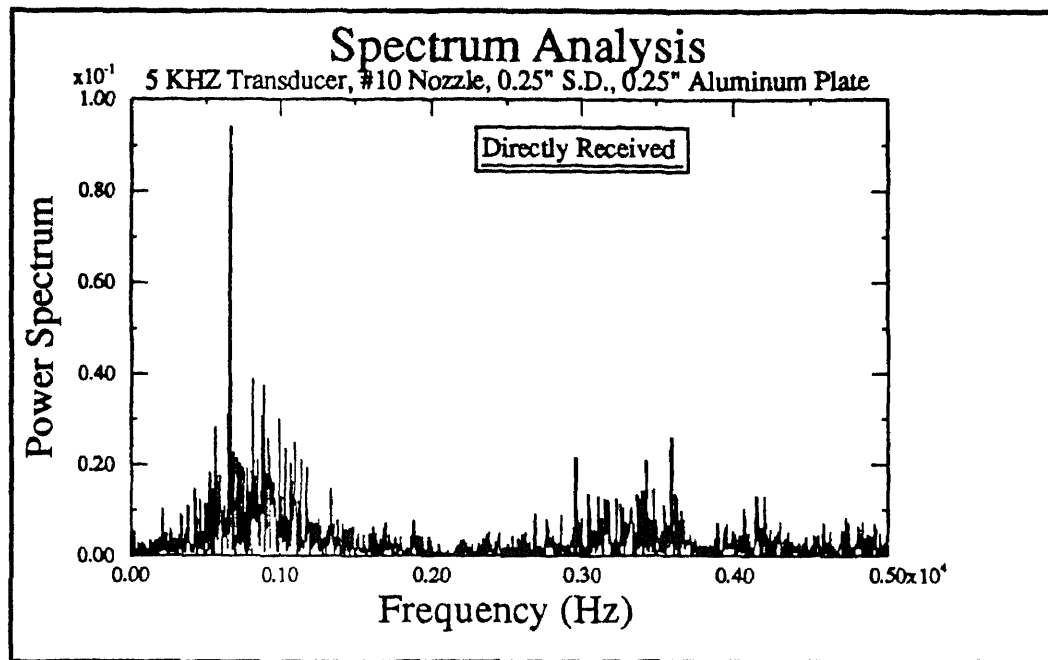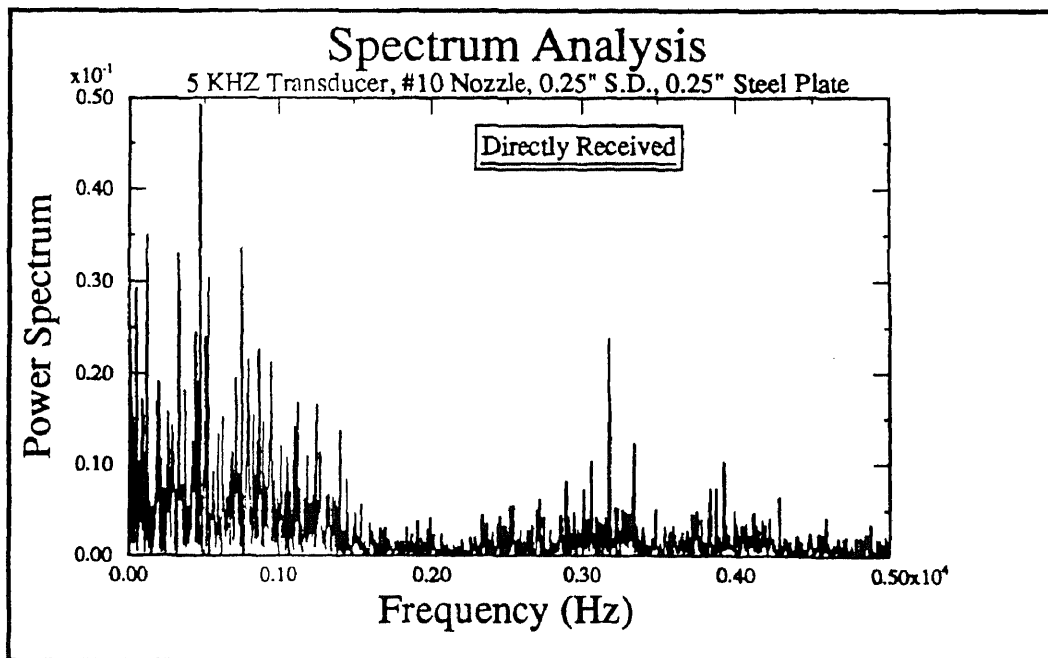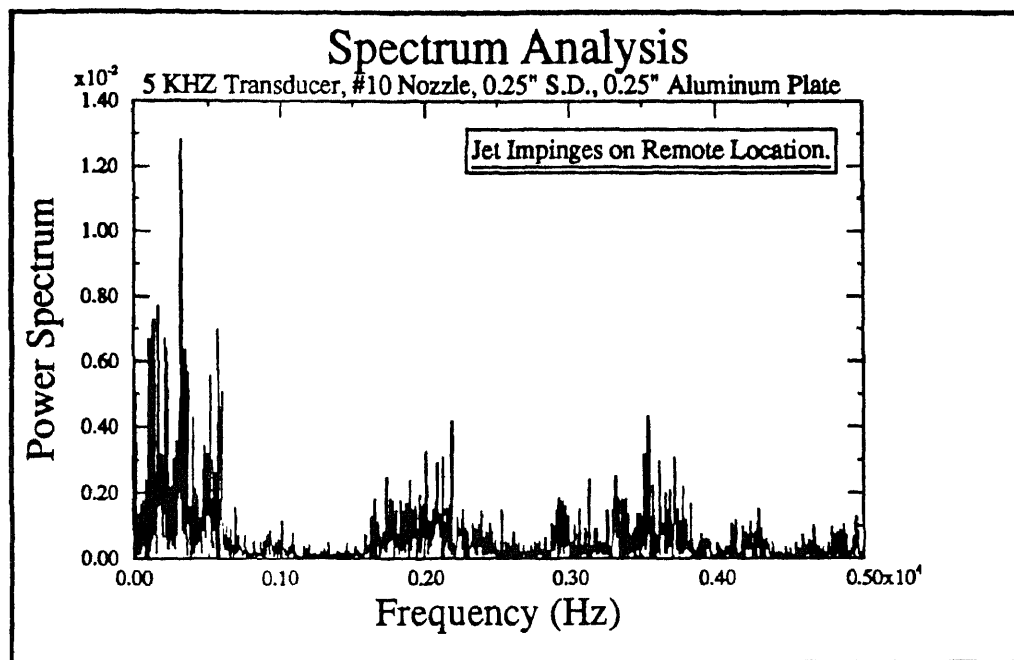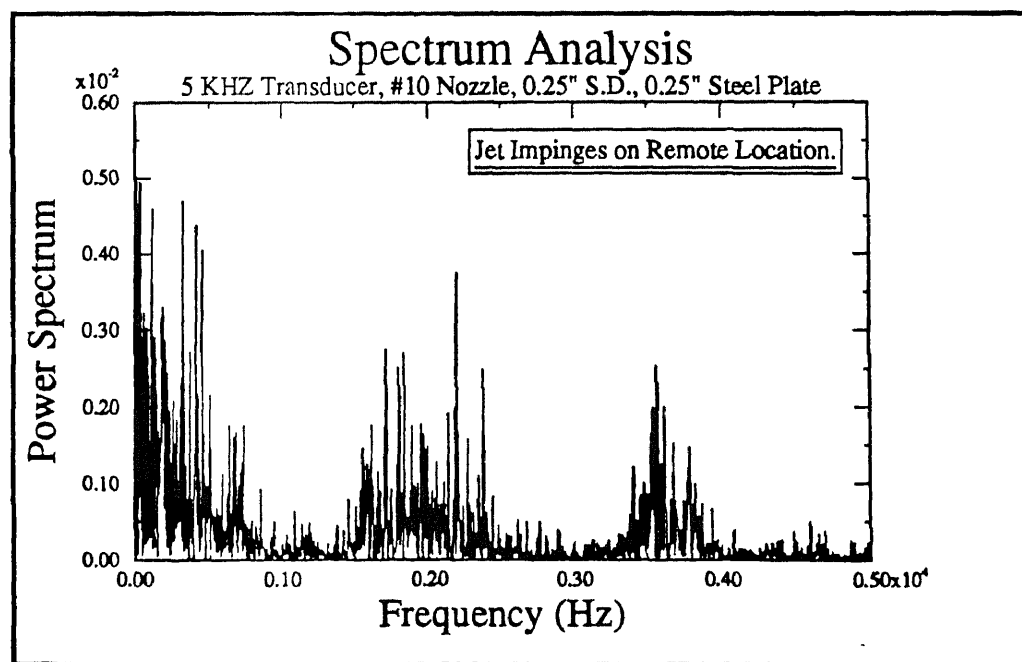
Figure 6.6

Figure 6.7

Figure 6.8
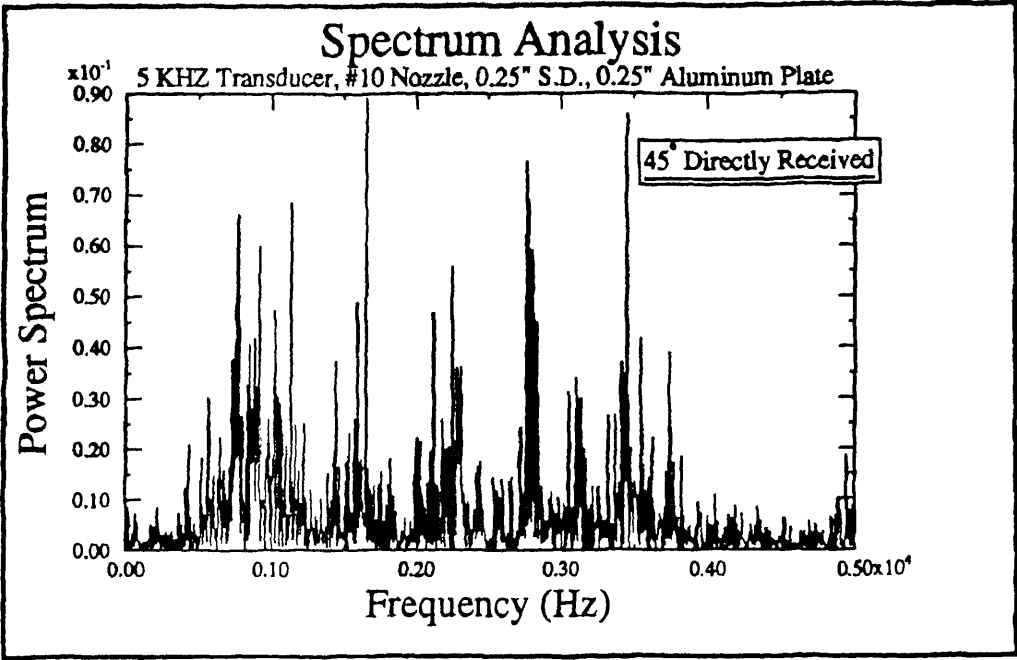
Figure 6.9
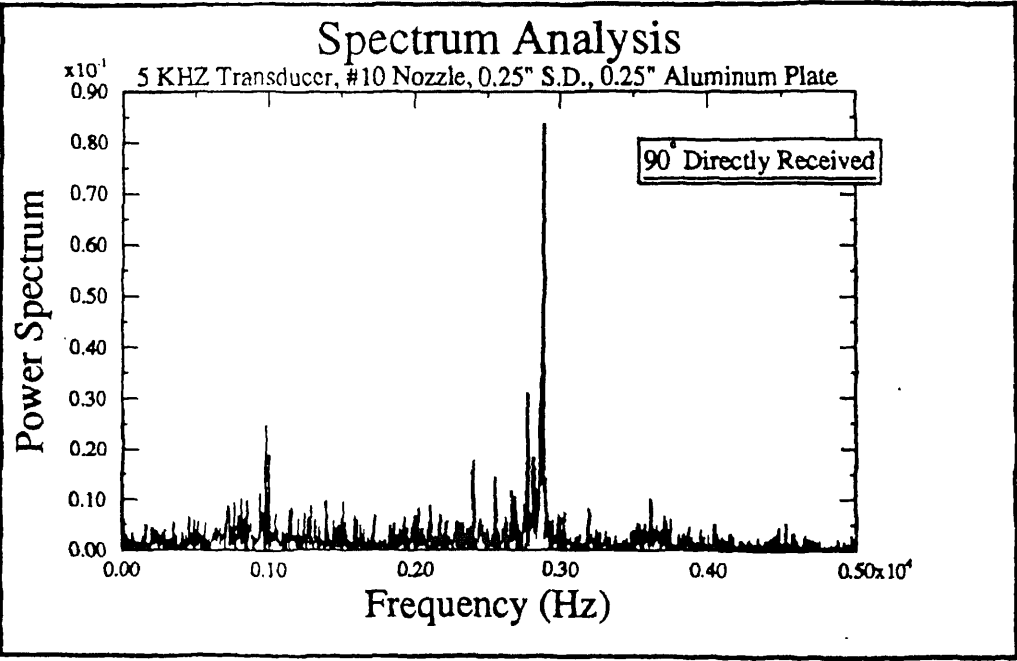
Figure 6.10
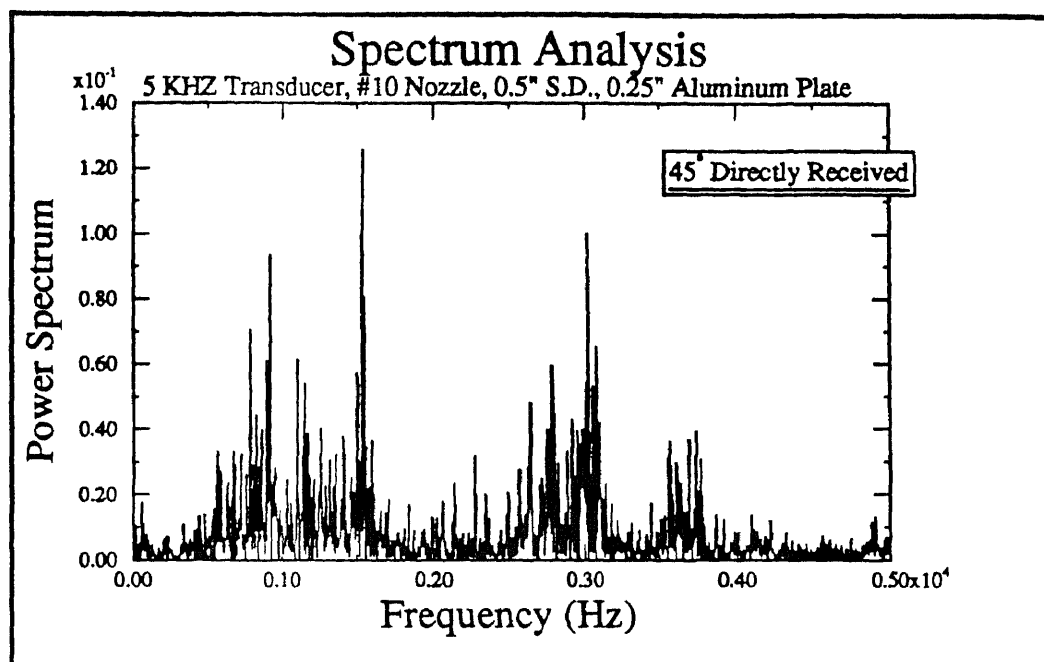
Figure 6.11
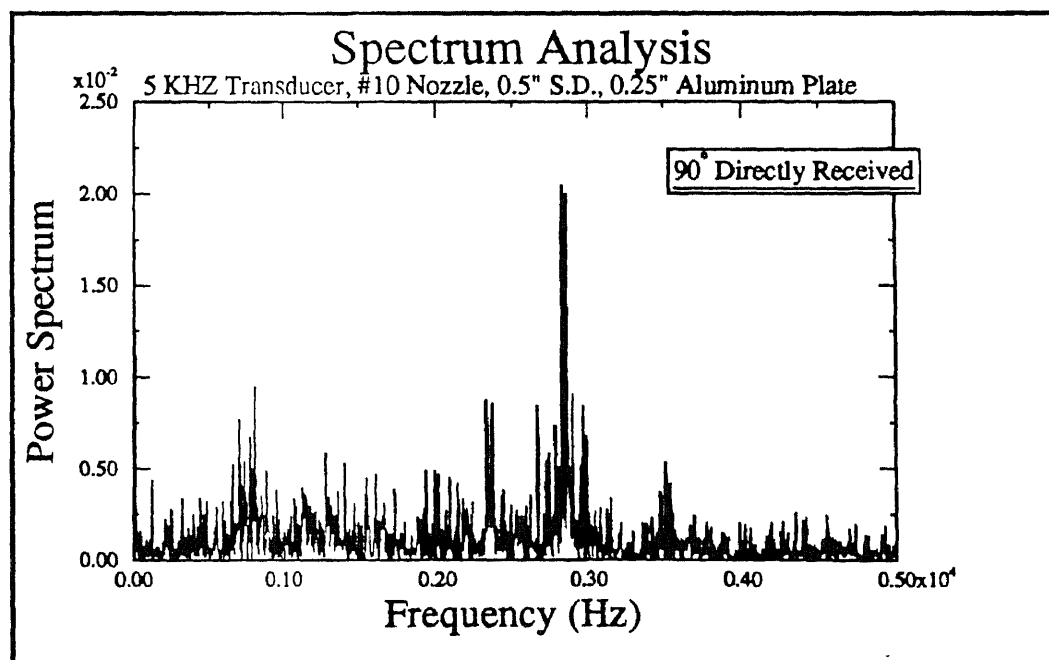
Figure 6.12
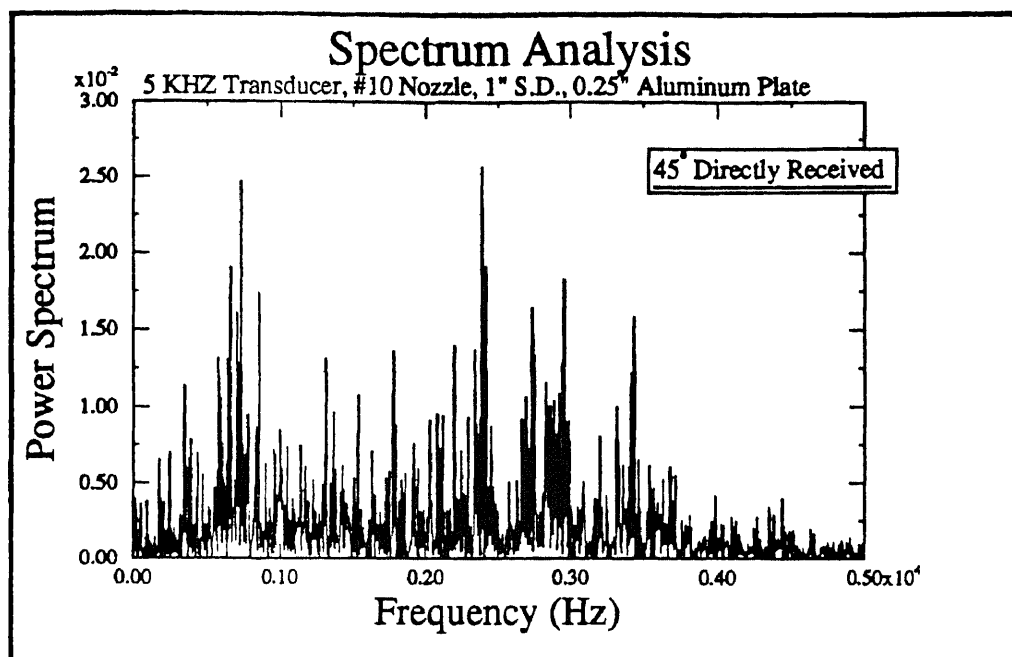
Figure 6.13
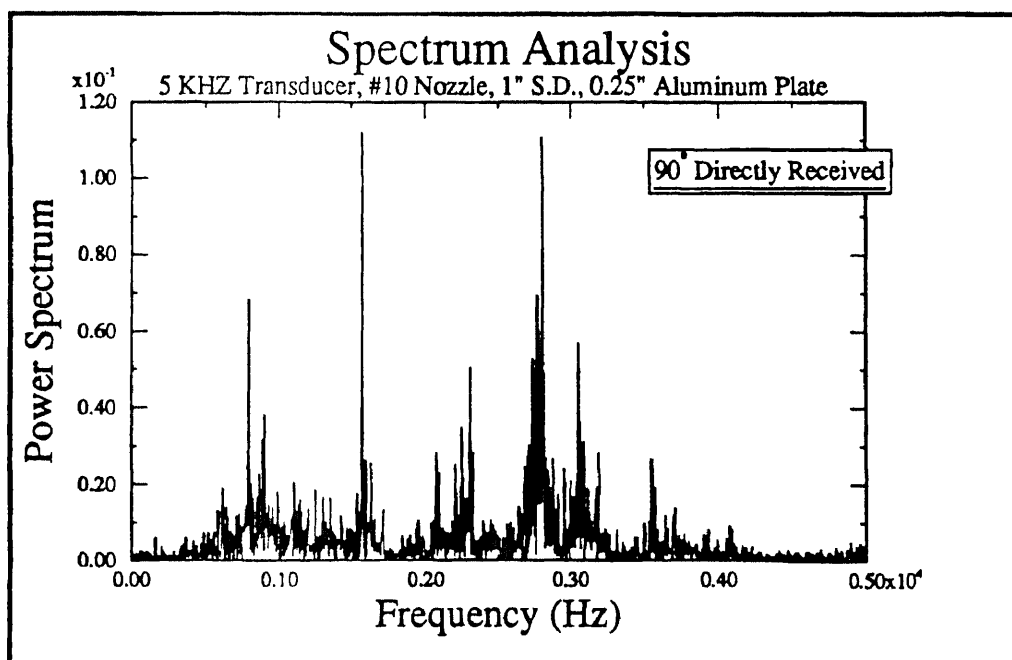
Figure 6.14
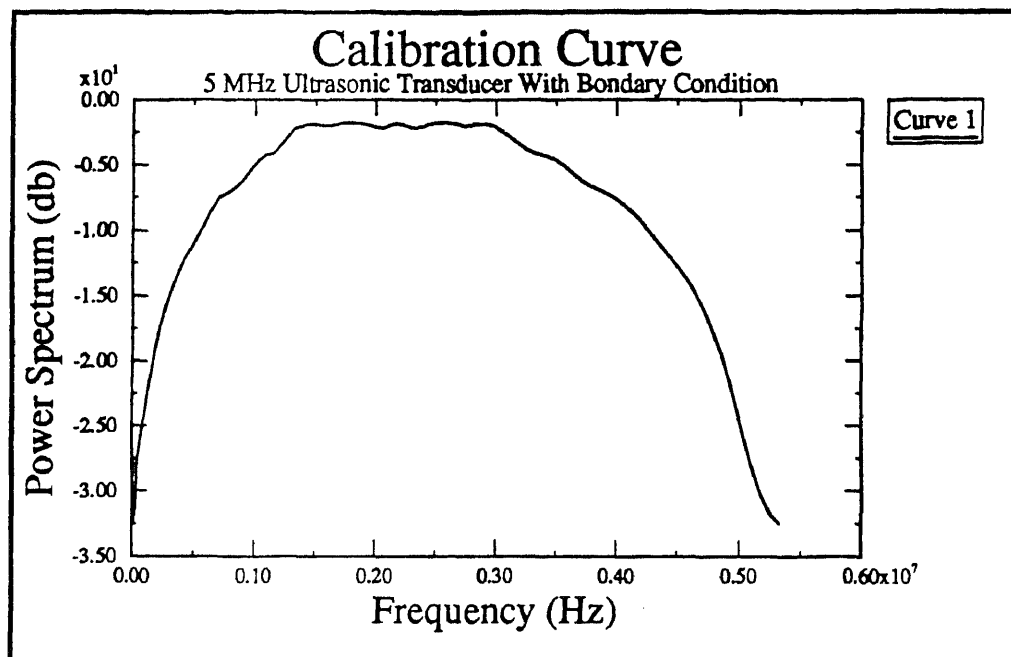
Figure 6.15
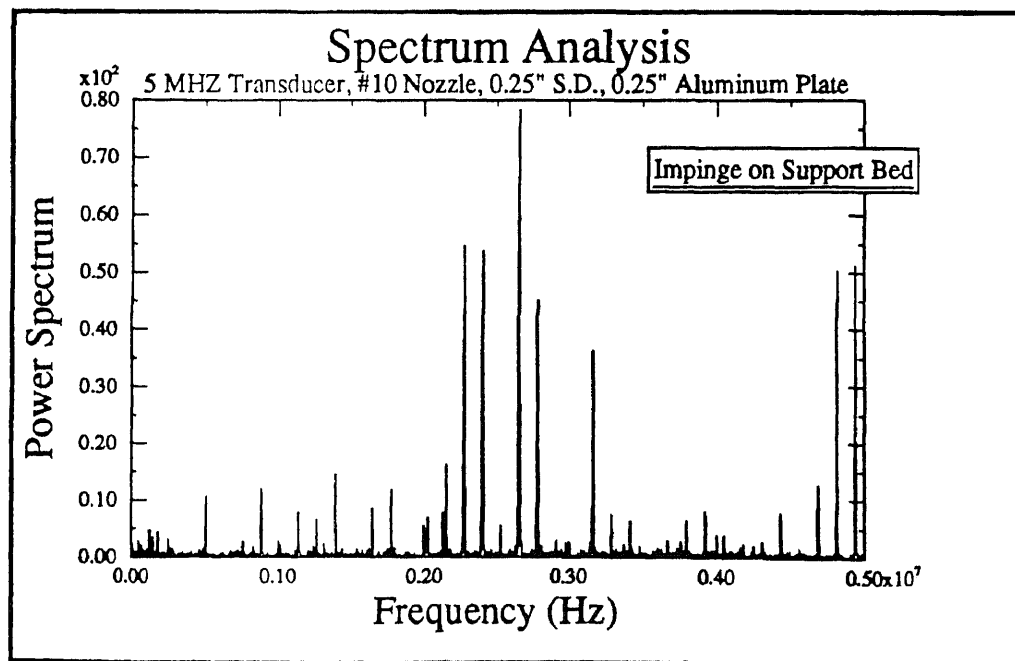
Figure 6.16
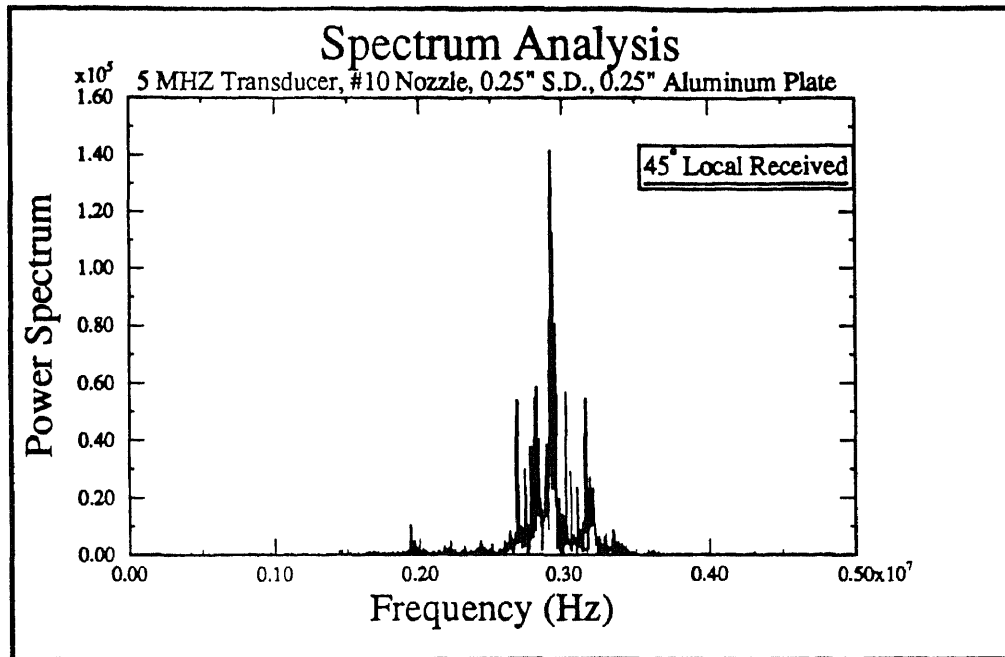
Figure 6.17
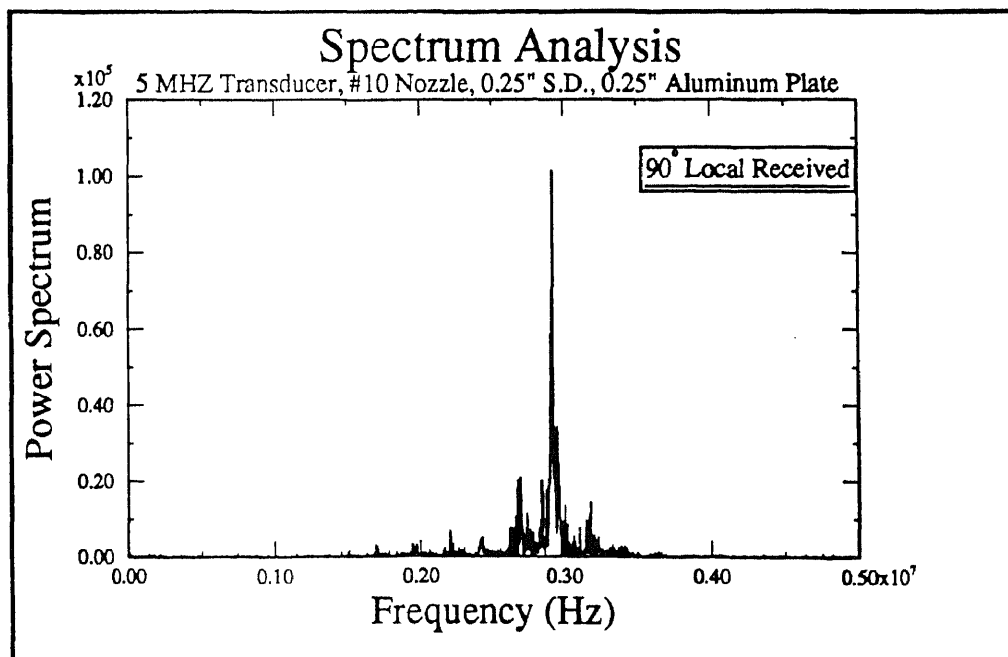
Figure 6.18
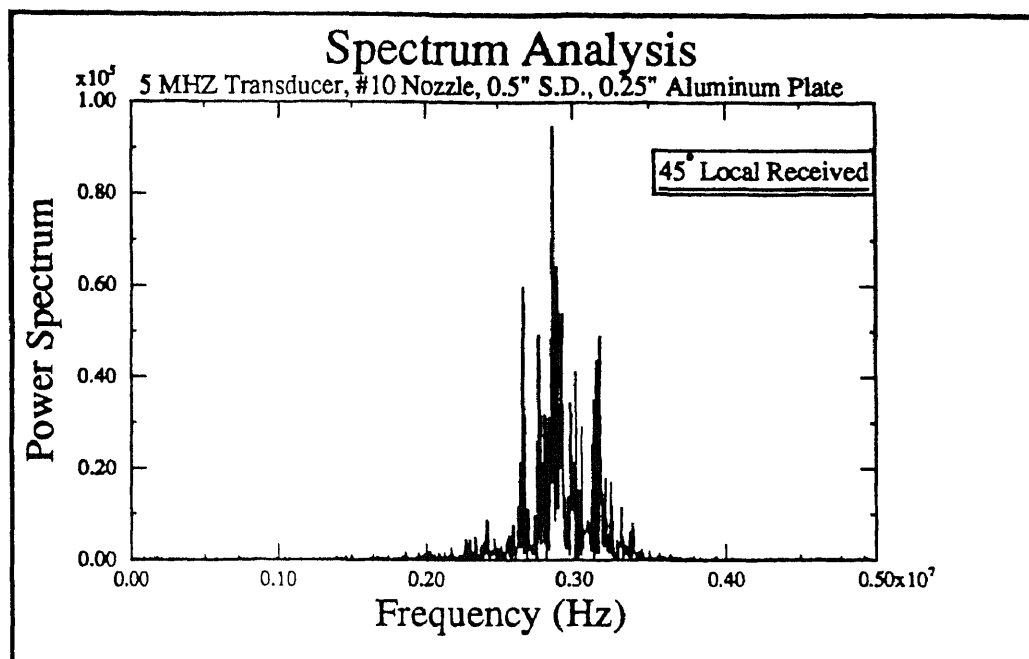
Figure 6.19
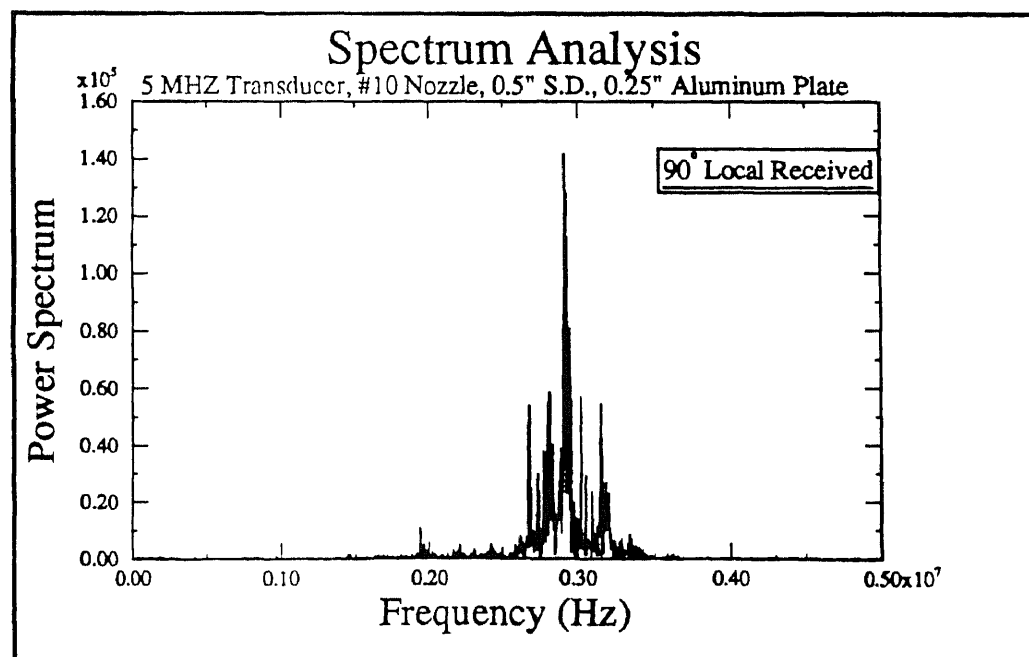
Figure 6.20
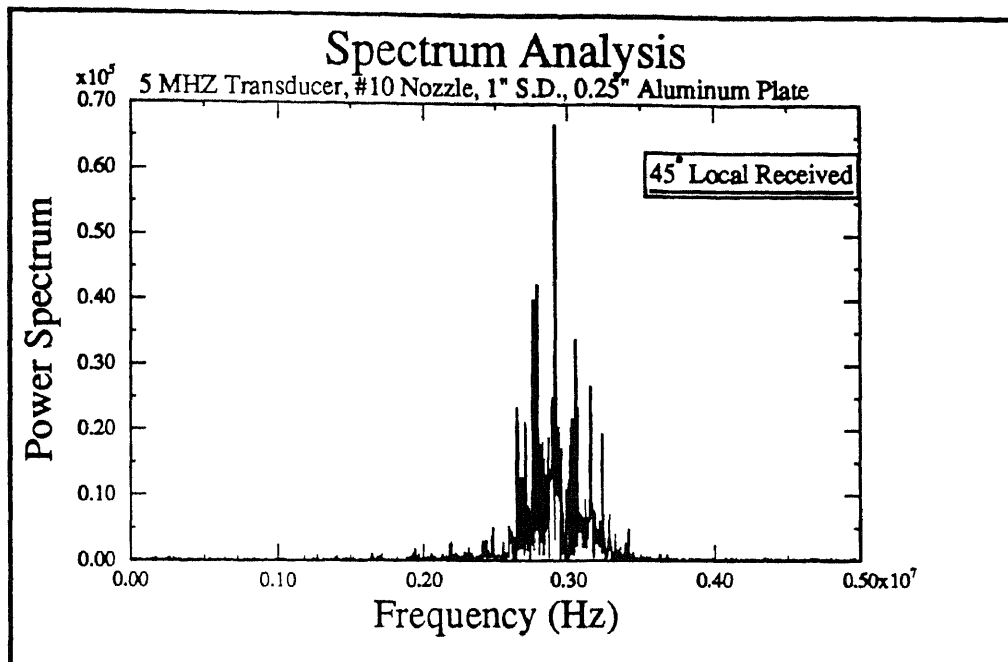
Figure 6.21
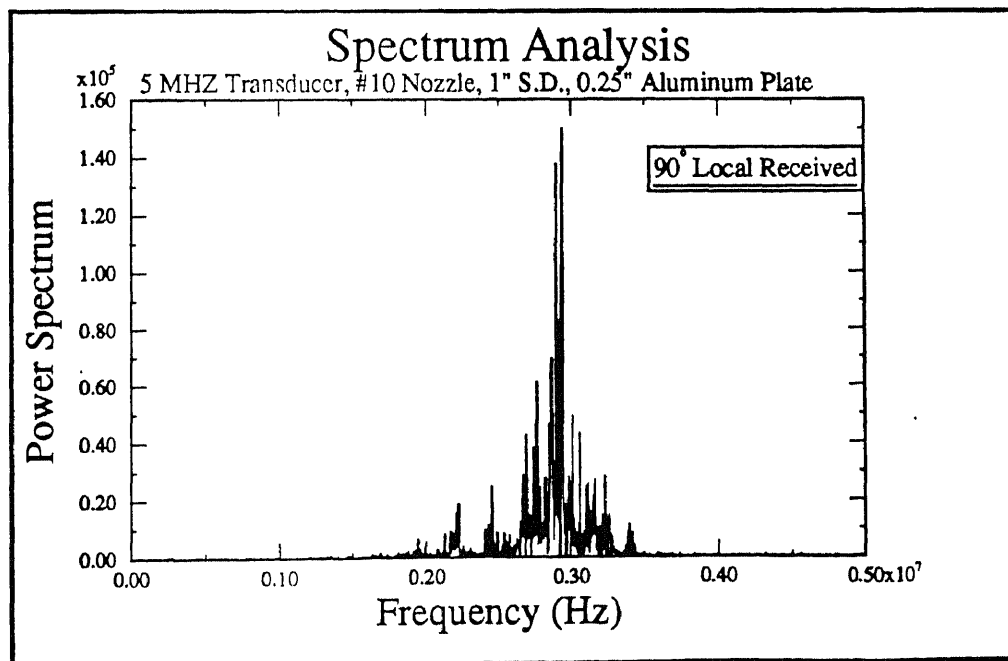
Figure 6.22

CHAPTER 7

EXPERIMENTAL RESULTS AND DISCUSSIONS

Through the experimental studies of material response to WJ impact, following conclusions can be made.

1. From the observation of topographies of material surface, the extremum at a specific thickness found in Figure 4.11, demonstrate the strong effect of the sample geometry on the rate of material removal. It is difficult to imagine any mechanism that could account for this other than resonance of the stress waves. Conversely, in the case of AWJ impingement, the sample thickness had no effect on the rate of the material removal (Figure 4.12). The material destruction by AWJ is due to effects of the individual particles and this process is localized in the vicinity of impingement and does not depend on the global conditions in the solid.

2. From the studies of fractographies, the damage pattern on material surface exhibits strong effects of non-directional fatigue. This fatigue effect, from the stress waves propagated in the material body, reduces the material endurance limit and fractures material. Observing the cross-section of the damage cavity, the size, the shallowness, and depth of the valleys combined with the observation of the surfaces in SEM pictures illustrate the damage mechanism of water jet machining of ductile material is cavitation erosion, which is resulting from cavitation and impact of microdroplets disintegrated from the jet.

3 . Two frequencies have been observed in stress wave measurement study. A 3 KHz frequency, observed in the 1-5 KHz span, is believed to be resulting from the resonances of the whole measurement structure and a 3 MHz frequency, observed in 1-5 MHz span, is believed to represent stress wave resonant frequency in the plate. That frequency is too high for the supporting structure.

FigureThe mode of the material removal by WJ, the effect of the plate geometry, and the fractographies of material surface as well as the direct measurement of stress waves in the impingement region, show that the material removal by WJ is to a great extent due to the stress waves generated in the impingement zone.

Material behavior under WJ interaction is believed to be erosion cavitation process on material surfaces. Longitudinal stress waves generated by this process propagate into material interior acting as a cyclic loading pattern. This constant frequency loading reduces material endurance limit, which is similar to the damage mechanism often observed in fatigue damage. In the following sections, a detailed description of this process and the interaction phenomenon are present.

7.1 Liquid Phase

It is generally believed and agreed that the bubbles or cavities form in a region where the liquid pressure is sufficiently below that within the microbubbles, to allow these to grow in spite of the restraining influence of surface tension. The growth process involves primarily the action of pressure forces, but these are also in the results of the interplay of surface tension, inertia, and viscosity, and gas diffusion and evaporation. The microbubble cavities may be carried to the low pressure region by the stream velocity or may grow in cracks or crevices in solid surfaces, primarily through the effect of gas diffusion until they become large enough to be entrained in the liquid stream through the interaction of drag forces and surface tension. In other cases they may conceivably be formed by liquid turbulent effects along the interface between the liquid and vapor-gas mixture in a relatively stationary cavity formed along the surface of a solid obstacle. They also may be formed by the entrained gas from the imperfection part of the stream boundary [20]. WJ stream then can reasonably be assumed to be composed of numerous bubbles in the jet core zone [17,20,45].

The periphery of a high pressure liquid stream represents a cascade of droplets due to the turbulent properties of the jet and energy reduction. This interaction between liquid and environment reduces the concentrated energy of the jet and gradually disintegrates jet to numerous water droplets. This phenomenon can be applied on WJ and observed in a high speed photography study [64].

When the liquid jet, either in the form of liquid droplets or vapor/air bubbles, impacts on solid material surface, two elastic shock waves are generated at the contact interface and start propagating inside each body.

7.2. Interaction Between Liquid Droplets and Solid Surface

Consider the first impact when a linear jet impinges upon a flat surface, Figure 7.2a. The pressure on the contact surface would instantly rise to the water-hammer pressure, Equation (7.1), and a tangential flow would initiate at the edge of the jet. This outward flow could be several times faster than the incident velocity. Meanwhile, the compressed liquid trapped under the cylindric jet is unable to escape toward the perimeter until " release waves" from the perimeter arrive, at a speed of sound. It would thus take a time t=r/c to start the central liquid flowing outward, at about the speed of incident, V. At that point, the pressure suddenly drops to the value of the stagnation pressure of the incompressible flow, Equation (7.2). The duration of the high pressure pulse for a 0.35mm (14/1000 inch) diameter water jet is calculated from the speed of sound, c=1500 m/sec, in water. Thus t=0.12 μs is obtained.

$$P_1 = \rho \times C \times V \qquad (7.1)$$

$$P_2 = \frac{f}{2} \times \rho \times V^2 \qquad (7.2)$$

The tangential outward flow, at the speed several time faster than incident veloc-

ity, will generate erosive effect on material surface. This erosive effect is due to the presence of the shear stress generated. The magnitude of the shear stress can be obtained by the boundary equation as:

$$\tau = \mu \times \frac{dU}{dy} \qquad (7.3)$$

τ: shear stress.
μ: absolute viscosity.
U: tangential flow velocity.
y: thickness of boundary.

Comparing the value of these three stresses, Equation(7.1), Eq(7.2) and Equation(7.3), it is apparently that the shear stress can't be a primary damage mechanism at velocity of interest unless the velocity is extremely high.(See Table 7.1)

Table 7.1 Comparison of stress generated by liquid impact.

Stress (Pascal)	V=500 m/sec	V=750 m/sec.
Water Hammer Effet	7.5×10^{8}	1.13×10^{9}
Stagnation Pressure	1.25×10^{8}	2.81×10^{8}
Shear Stress*	12.1	18.1

*Shear stress was calculated based on the assumptions that U=5V, temperature = 20°C, $\mu = 1 \times 10^{-3}$ N-sec/m^2 and boundary thickness to be 30 μm.

For non-linear liquid, the wave generated also will travel at the velocity of acoustic speed. The magnitude of the peak interaction pressure changes according to the Tait's equation as [17,20]:

$$P\left(\frac{\rho_0}{\rho}\right) = B \times \left(\left(\frac{\rho_0}{\rho}\right)^{-n} - 1 \right) \qquad (7.4)$$

For Water: n=7 and B=3000 bar.
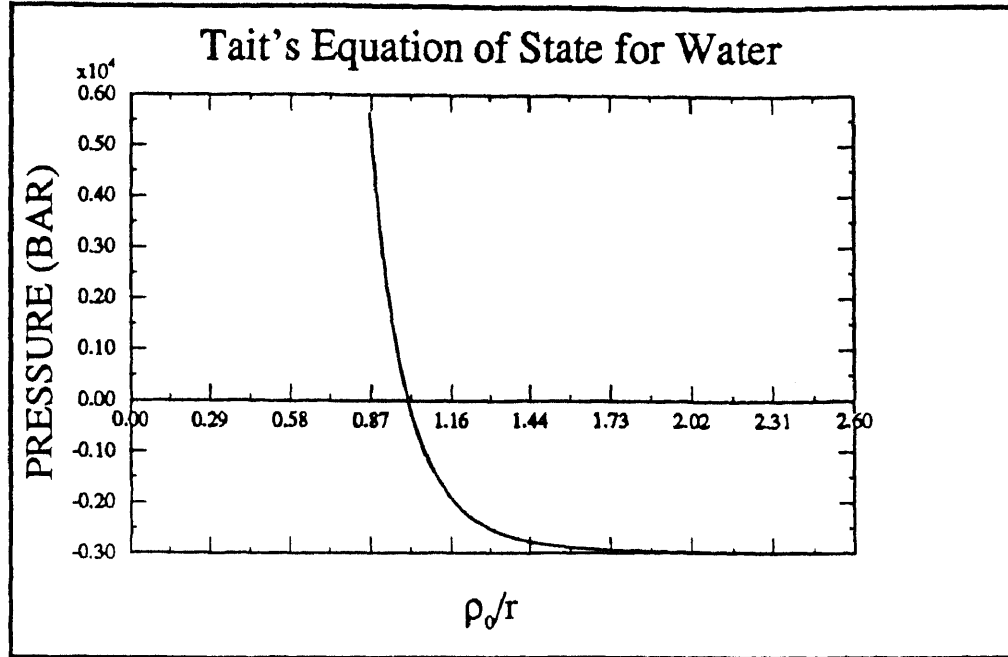
Figure 7.1 Nonlinear liquid jet pressure changes according to Tait's Equation.

Inspecting Tait's equation, the pressure vanishes in the initial configuration, ρ_0/ρ =1, and increases rapidly as the liquid is squeezed, ρ_0/ρ =0, or drops to the residual value -B as the liquid is expanded, ρ_0/ρ =∞. Morever, the elastic dilatation wave velocity is given by [51,53,54]

$$V^2_{dilatation} = \frac{dP}{d\rho} = (n\frac{B}{\rho_0})(\frac{\rho}{\rho_0})^{n-1} \qquad (7.5)$$

In the case of the liquid jet impinged on a damaged concave solid surface, Figure 7.2b, both the outward and inward flow must be considered separately. The concave surface fills with liquid in time $t=y/V= r(1-\cos \theta)/V$ and the diameter of the trapped liquid is $2x_0=d+2Ut=d+[2r(1-\cos \theta)v]/V$. Based on this calculation, Vicker found U=6V is an acceptable value [40].

7.3. Interaction Between Liquid Bubbles and Solid Surface

Collapse of vapor/air microbubbles on material surface has been extensively studied by many researchers. The phenomenological and the numerical model have been generally constructed. A typical example is shown in Figure 7.3 [20,45]. These results showing that the initial collapse of microbubbles is from the sides normal to the rigid surface, followed by the accelerating collapse of the side away from the wall, and the development of a microjet. The interaction between this microjet and solid surface is similar to that of the liquid jet impingement on material surface.

However, the actual calculation of the stress regime applied to a surface eroded by cavitation is still unknown due to the complexity of processes involved. Since the surface damaged from cavitation and droplet impacts often have a very similar appearance, it can be presumed that these two processes are quite similar in their effects on material surface.

7.4 Material Response to Liquid Jet Impact

Elasticity theory for isotropic solid considers there are two types of waves propagated in the material. Dilatational(Longitudinal) waves travel with particles motion induced by the disturbance normal to the wave front. Distortional (Transverse or Shear) waves are those in which the particles move in a plane at right angles to that in which the wave front propagates. The expressions for the velocity of propagation for these two type waves, denoted by C_L and C_S are well known and given as

$$C_L = \sqrt{\frac{E}{\rho}} \qquad (7.6)$$

$$C_S = \sqrt{\frac{G}{\rho}} \qquad (7.7)$$

In addition to dilatational and distortional waves that travel through solid medium,

elastic waves may be propagated along the surface of a solid. Rayleigh surface wave decays exponentially with depth from the surface to the medium interior. In this rapid decay, the amplitude is only appreciable near the surface of the body. Love wave only can only be propagated in a layer material which possesses different physical constants for different layers.

When either a dilatational or distortional wave impinges on a boundary of the solid, waves of both types are generated. For a normal impact compressive pulse, the pulse is reflected as a tensile wave and if its amplitude is greater than the tensile strength of the material, fractures occur causing material separation, Figure 7.4. As the intensity of the applied load increases, the material is driven beyond its elastic limit and becomes plastic. Two types waves now propagate in the solid, an elastic wave followed by a much slower but more intense plastic wave. If the characteristics of the medium are such that the velocity of propagation of larger disturbances is greater than the propagation velocity of smaller one, the stress pulse develops a steeper and steeper front on passing through the medium, and the thickness of this front is ultimately determined by the molecular constitution of the medium. The steeper wave(shock wave) thus formed differs from the high pressures generated by conventional methods in that it relies on the internal response of material to rapid acceleration rather than to static constraints.
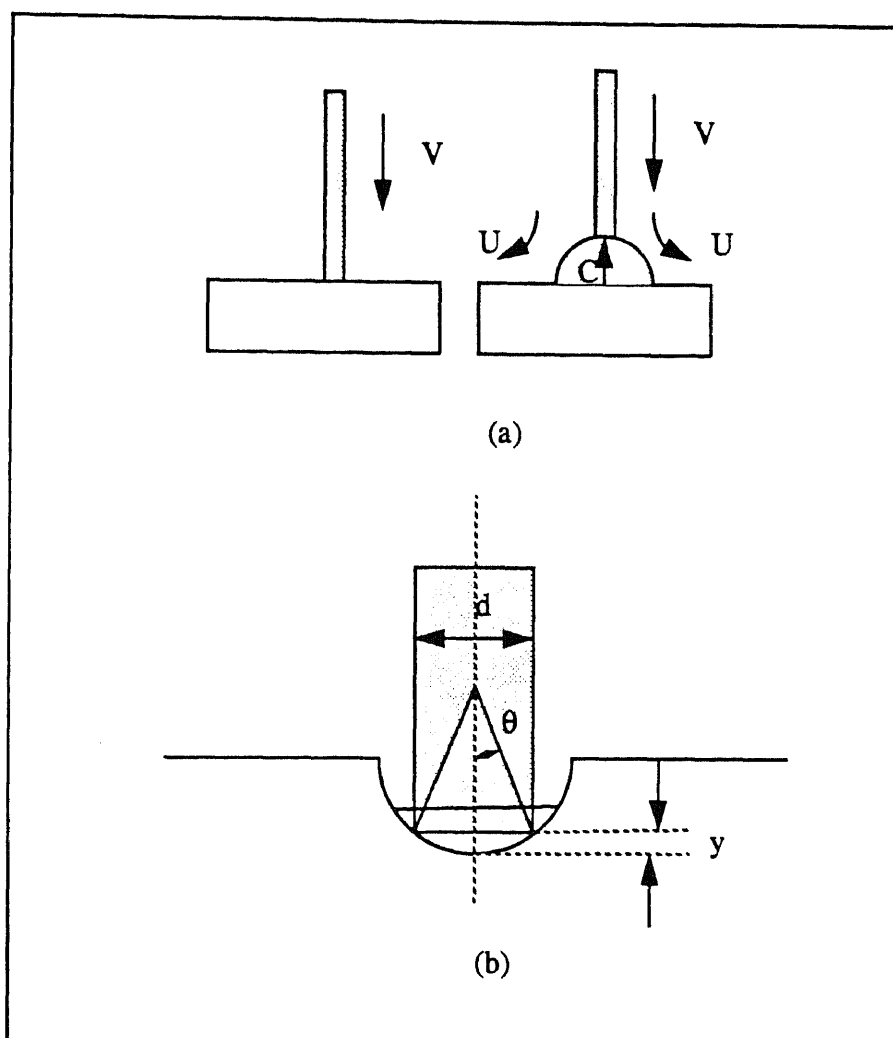
Figure 7.2 Schematic of Flat End Impact and Concave Surface Impact.
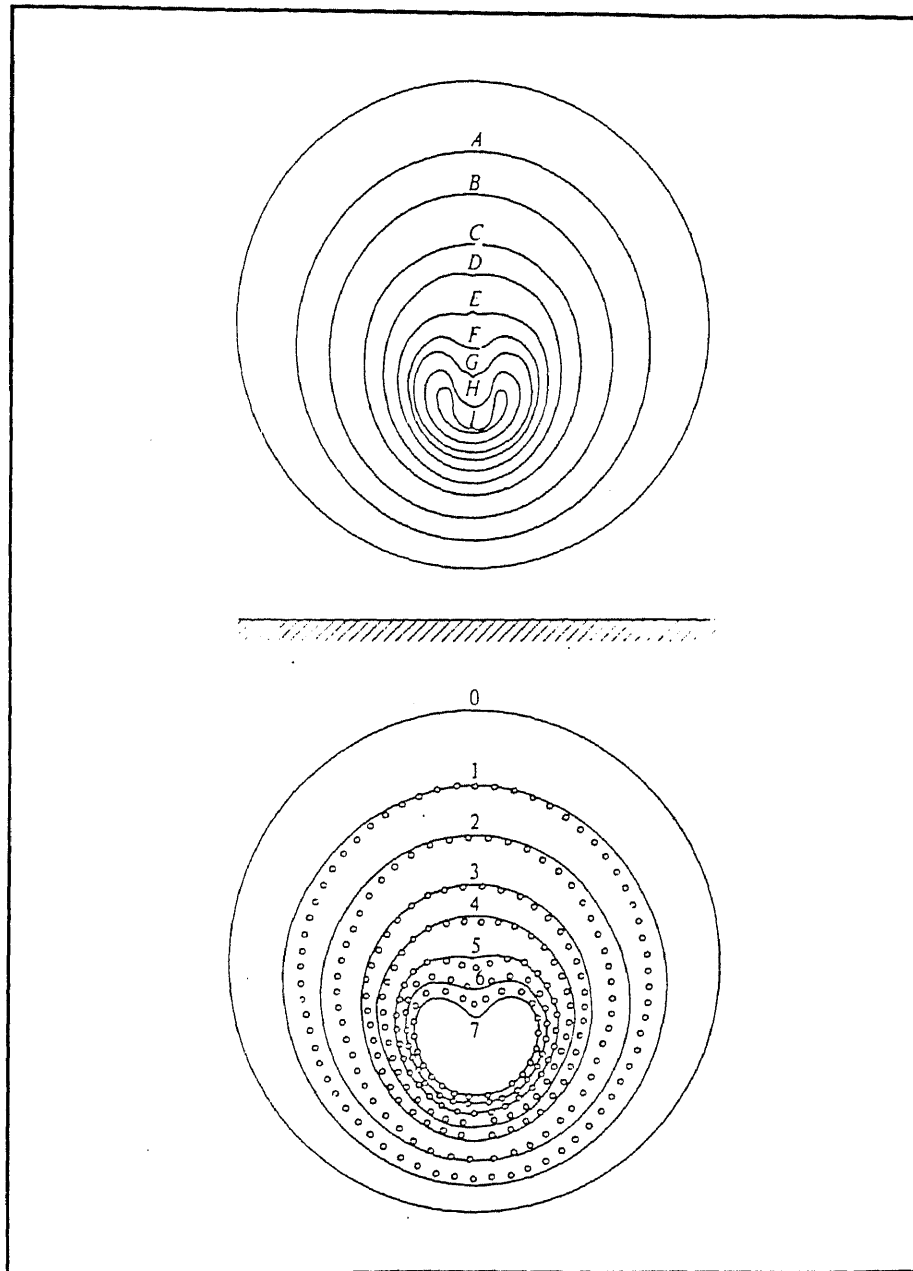
Figure 7.3 Computed bubble collapse, From Plesset-Chapmann[20,45]
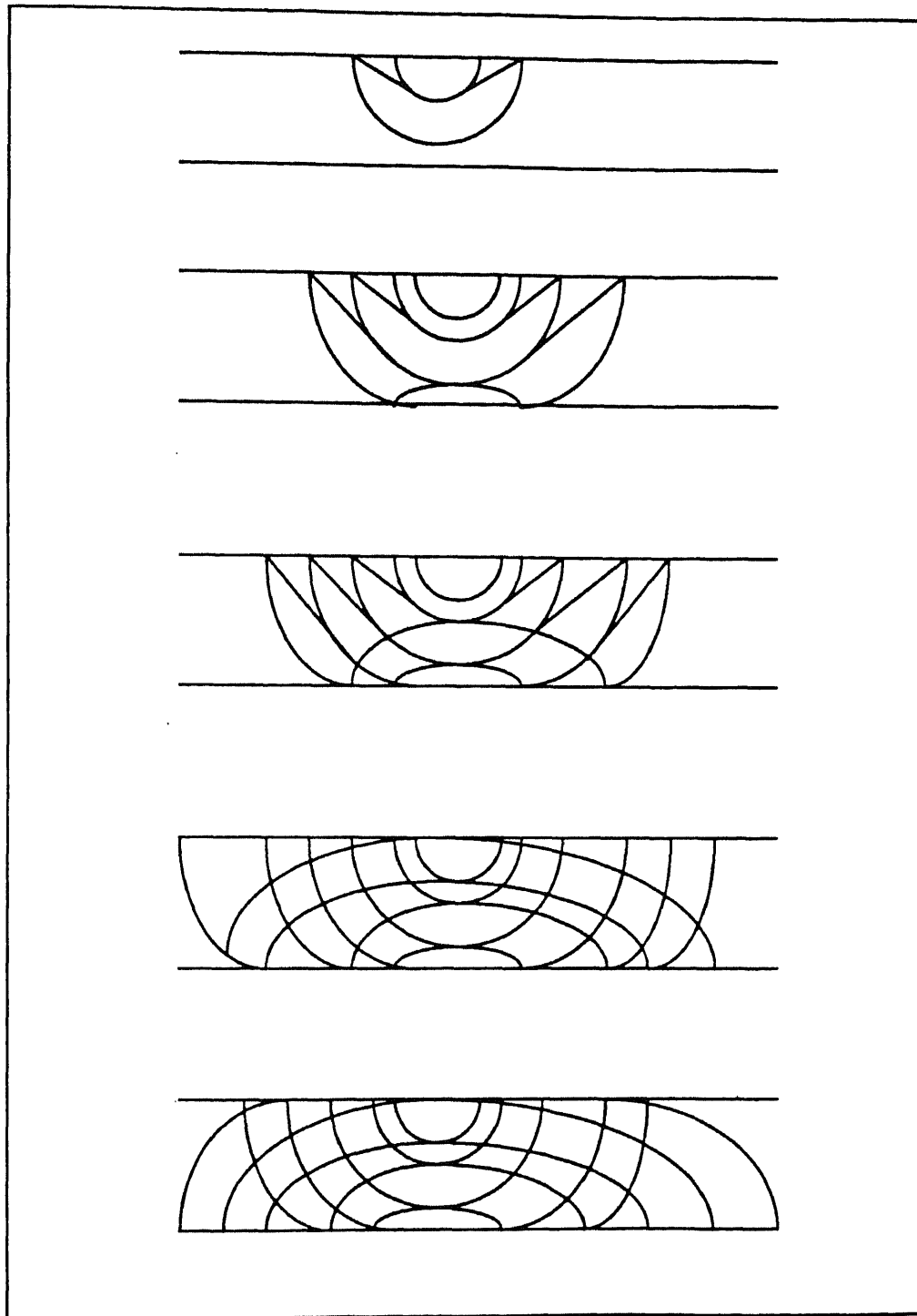
Figure 7.4 Stress Wavefronts propagation due to a point load excitation on a plate.

CHAPTER 8

NUMERICAL SIMULATION

Analytical models, although limited in scope, are quite useful for developing an appreciation for the dominant physical phenomena occurring in a given impact situation. They may be even useful in making predictions, provided care is taken not to violate the simplifying assumptions introduced in their derivation or exceed the database from which empirical constants are derived. If a complete solution to impact situation is necessary, resource must be made to numerical simulation.

Two dimensional numerical simulations of high pressure water jet impact on ductile material have been performed in this study. Finite element method in Langrangean coordinate is used to describe the material response at impact and the displacement output is coupled with Continuum Damage Mechanics to predict the damage growth on material surface. A schematic of the process is given in Figure 8.1.
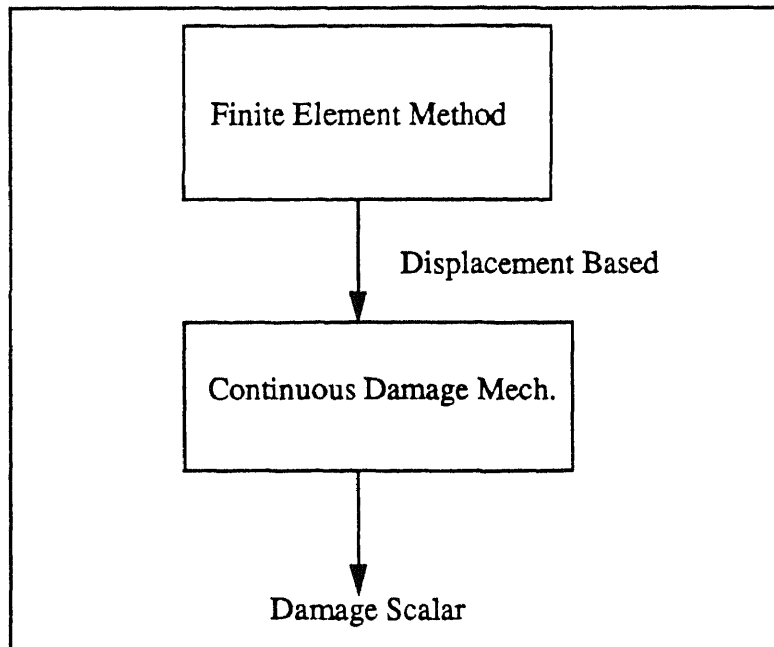
Figure 8.1. Numerical Process of WJ Impact Simulation.

8.1 Discretization Method

It is necessary to replace a continuous physical system by a discretized system in a computational analysis. In the discretization process, the continuum is replaced by a computational mesh. The techniques most commonly used are Finite Difference Method and Finite Element Method.

A common property of both the Finite Element and Finite Difference method is the local separation of the spatial dependence from the time dependence of the dependent variable. The major advantage of finite element method compared with finite difference method is in treating geometries and variations in mesh size and type. In finite element method, the equations of motion are formulated through nodal forces for each element and do not depend on the shape of the neighboring meshes while equations of motion are expressed directly in terms of pressure gradients of the neighboring mesh in finite difference method. This inherently requires the differential equations must be formulated separately for irregular regions and boundaries. In this simulation, finite element method is adopted to discretize the field equations of motion.

8.1.1 Field Equations

Consider a body with volume Ω and a surface $\partial\Omega = \partial_\sigma\Omega \cup \partial_u\Omega$ where $\partial_\sigma\Omega$ and $\partial_u\Omega$ are the traction and kinematic boundaries respectively and $\partial_\sigma\Omega \cap \partial_u\Omega = 0$. The equation of momentum balance and boundary conditions are[51,52]

$$\sigma_{ji,i} + \rho b_i = \rho \ddot{u}_i \quad in \quad \Omega \quad (8.1)$$

$$\sigma_{ji} = \sigma_{ij} \quad in \quad \Omega \quad (8.2)$$

$$t_i = \sigma_{ji} n_j \quad on \quad \partial_\sigma\Omega \quad (8.3)$$

$$u_i = \bar{u}_i \quad on \quad \partial_u\Omega \quad (8.4)$$

,where σ_{ij} is the Cauchy stress, b_i is the body force per unit mass, t_i is the surface traction and u_i is the displacement and a superposed dot denotes differentiation with respect to time. Initial conditions are specified as

$$u_i(x, 0) = u_i^0 \qquad on \qquad \Omega \qquad (8.5)$$

$$\dot{u}_i(x, 0) = v_i^0 \qquad in \qquad \Omega \qquad (8.6)$$

The constitutive equation is specified by writting the strain as the sum of elastic and plastic parts [52]; that is

$$\varepsilon_{ij} = \varepsilon^e_{ij} + \varepsilon^p_{ij} \qquad (8.7)$$

It is assumed that the stress may be derived from an elastic potential[53] by which:

$$\sigma_{ji} = \frac{\partial}{\partial \varepsilon^e_{ij}} W(\varepsilon^e_{kl}) \qquad (8.8)$$

Taking the time derivative of Equation (8.7), we obtain

$$\dot{\varepsilon}_{ij} = \dot{\varepsilon}^e_{ij} + \dot{\varepsilon}^p_{ij} \qquad (8.9)$$

The stress-rate elastic strain relation can be written as

$$\dot{\sigma}_{ij} = L_{ijkl}\dot{\varepsilon}_{kl} \qquad (8.10)$$

Where $L_{ijkl} = \partial^2 W/\partial\varepsilon^e_{ij}\partial\varepsilon^e_{kl}$ is the tensor of elastic moduli.

When the stress generated over the yield locus criteria, Von-Mises criterion is adopted in this simulation [54], the plastic flow rule can be presented as

$$\dot{\varepsilon}^p_{ij} = \frac{\phi}{\eta}\dot{\sigma}_{ij} \qquad (8.11)$$

Where ϕ is a relation function and η is a viscosity parameter.

The equation of motion in Equation (8.1) can be equivalently stated in weak form by the principle of virtual work, i.e.,

$$\int_{\Omega} (\sigma_{ij}\delta\varepsilon_{ij} + \rho\,(\ddot{u}_i - b_i)\,\delta u_i)\,d\Omega = \int_{\partial_\sigma\Omega} t_i\,(\delta u_i)\,d\Gamma \qquad (8.12)$$

Where Γ is the surface.

The body force b_i is neglected in the subsequent discussion.

8.1.2. Spatial discretization

Spatial discretization of the weak form of momentum balance, Equation (8.1), is determined by the finite element method. The displacement and variation fields are approximated as [55,56]:

$$U(x, t) = N(x)U^a(t) \qquad (8.13)$$

Where $N(x)$ is the matrix of global interpolation functions and the super-

script a denotes a nodal quantity. The symmetric gradient operator is denoted as **B** as

$$\delta\varepsilon = B\delta U \qquad (8.14)$$

Using the above relations, and the arbitrariness of the nodal variations, Equation (8.12) may be written in semidiscrete form as

$$M\ddot{U}^a = f - F \qquad (8.15)$$

Where

$$M = \int_\Omega \rho N^T N d\Omega \qquad (8.16a)$$

$$f = \int_{\partial_\sigma \Omega} N^T t d\Gamma \qquad (8.16b)$$

$$F = \int_\Omega B^T \sigma d\Omega \qquad (8.16c)$$

A lumped mass matrix may be obtained from the consistent mass matrix. Equation (8.15) is a system of ordinary differential equations in time and may be integrated using a number of schemes. Explicit central difference method is applied in this study [55,56,57].

8.1.3 Time Step Integration

Time integration routines are the heart of most structural dynamics programs. Broadly, it may be said that implicit integration methods are most effective

for structure dynamics problems while explicit integration methods are best for wave propagation problems.

Methods for integrating the discretized equations of continuum mechanics are called explicit if displacements at time t+Δt in the computational cycle are independent of the accelerations at the time. Rewrite the equation of motion, Equation (8.1), in the form of:

$$M\ddot{u} + Ku = F(t, u) \qquad (8.17)$$

Where M is the lumped mass matrix, K is the stiffness matrix, u is the displacement vector, and F the load vector.

Express velocities and accelerations by difference equivalents in time [55,56,57,58]:

$$\dot{u}(t+\frac{\Delta t}{2}) = \frac{1}{\Delta t}\left[u(t+\frac{\Delta t}{2}) - u(t)\right] \qquad (8.18)$$

$$\ddot{u}(t) = \frac{1}{\Delta t}\left[\dot{u}(t+\frac{\Delta t}{2}) - \dot{u}(t-\frac{\Delta t}{2})\right] \qquad (8.19)$$

Replacing the acceleration term in Equation (8.17) by Equation (8.19) and using Equation (8.18) to put things in term of displacements yields a recurrence relation to be solved at each time:

$$Mu(t+\Delta t) = (\Delta t)^2 F(t) + [2M - (\Delta t)^2 K]u(t) - Mu(t-\Delta t) \qquad (8.20)$$

At any time step, if the velocities and displacements are known, the rate of deformation and strain can be computed from the strain-displacement relation and

the stresses at that time step are found from the constitutive relationship. The equation of motion is then used to find the accelerations, which, together with velocities, are stepped forward in time to find new displacements and the entire procedures are repeated once again.

8.1.4. Mesh Description

There are two basic approaches for describing the motion of a deformable body; material (Lagrangean) description and the spatial (Eulerian) description.

Schematically, the material description concentrates on a constant amount of matter, called the system, and then follows its motion, throughout the open ambient space. A typical example of a Lagrangian grid is shown in Figure 8.2a. In contrast, the spatial description, Figure 8.2b, focuses on a closed volume of the ambient space, called the control volume, and then observes a variable amount of matter flowing through it. As the description applied, Lagrangean code is usually applied to a whole solid in its reference configuration and Eulerian code is applied to a portion of a fluid in its current configuration[17,58].
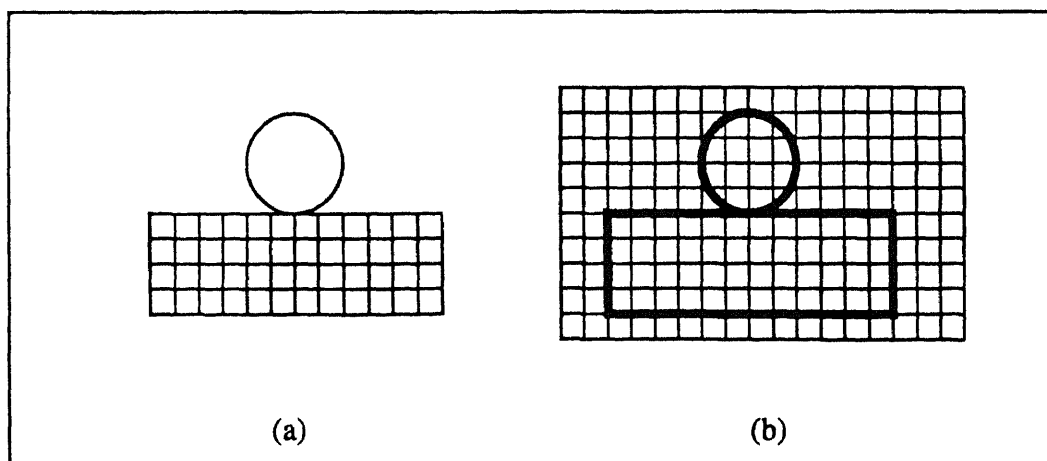
Figure 8.2. Description of Langrangean(a) and Eulerian(b) grid.

Although they are consistent with each other in principle, the material and

spatial descriptions are not equivalent in practice. They differ not only by the relative extents of the volume of matter and of control perceived by the observer, but also by the type of the variable selected to describe the motion. The displacement of each particle is usually chosen for the Langrangean code and the velocity is selected for the Eulerian code [17].

In this study, material description is used to describe the displacement of each material particle deformed.

8.2 Continuum Damage Mechanics

Material can be damaged in many reasons such as creep damage, ductile plastic damage, fatigue damage, and environmental degradation, etc. Each damage has its own fracture characteristics and damage criteria with it. However, the changes to the material structure are irreversible and its entropy increases during the damage process [59,64].

Damage to the metals is mainly the process of the initiation and growth of micro-cracks and cavities induced by large deformation. At that scale, this damage phenomenon is discontinuous. Kachanove [60] was the first to introduce a continuous variable related to the density of such defects. This variable has constitutive equations for evolution, written in terms of stress or strain, which are used in structure calculations in order to predict the initiation of macro-crack. These constitutive equations have been formulated in the framework of thermodynamics and have been applied to many phenomena [61,62,63].

Damage accumulation can take place under elastic deformation, elastic-plastic deformation or creep damage. For the phenomenological description of micro-structure changes it is necessary to introduce some internal variables to describe the damage accumulation state. From the point of view of applications it is required

that the set of parameters must be simple enough and should have an evident mechanical sense.

Consider the surface S of a material body with an unit normal v, Figure 8.3.
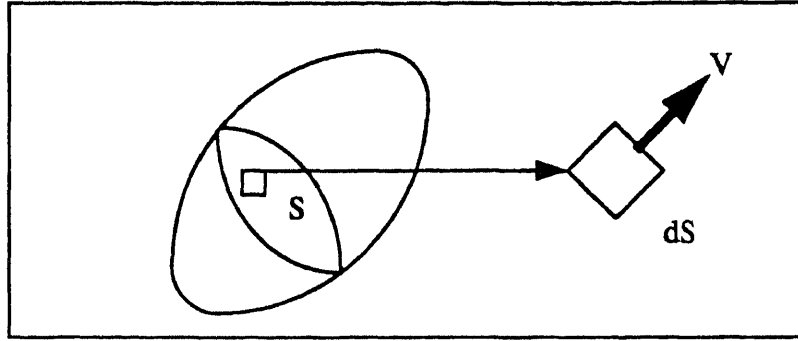
Figure 8.3. Description of Surface and Normal unit Vector.

Let A_0 be the initial area of the undamaged section. As the result of damage a certain part of the section is fractured and denotes the lost area by A.

Consider the damage as isotropic; crack and microvoids are equally distributed in all direction, and the damage variable can be interpreted as a scalar as

$$d = \frac{A}{A_0} \qquad (8.21)$$

Since the damage is irreversible, d is a positive monotonically increasing function. For undamage material, $d=0$; at fracture $d=1$.

The multiplicative kinematic split of the deformation gradient tensor F into the elastic and plastic part can be written as

$$F = F^e F^p \qquad (8.22)$$

By using the Langrangean tensors in material description, we can consider the energy potential of material interested as [65,66,67]

$$\psi(E, E^p, Q, d) = (1-d)\psi^0(E, E^p, Q) = (1-d)[\psi_e^0(E, E^p) + \psi_p^0(Q)] \qquad (8.23)$$

Here $E=0.5(C-I)$ and $E^p=0.5(Cp-I)$ denote the total and plastic Lagrangian strain tensors, respectively, with $C=F^T F$ and $C^p=F^{pT}F^p$. In addition, Q is a state variable of plastic; ψ^0 is the total potential stored in an undamaged material.

Assuming the damage is an elastic process, classic energy method introduces

$$S = \rho_0(1-d)\frac{\partial}{\partial E}\psi_0^e(E, E^p) \qquad (8.24)$$

Where S is the symmetric Piola-Kirchhoff stress tensor and ρ_0 is the mass density.

Effective stress $\overline{S}$ over the effective resisting area is given by

$$\overline{S} = \frac{S}{(1-d)} = \rho_0\frac{\partial}{\partial E}\psi_0^e(E, E^p) \qquad (8.25)$$

Defining a locally average free energy ξ to characterize the damage loading/ unloading conditions,

$$\xi = \rho_0 \psi^0 (E, E^p, Q) \qquad (8.26)$$

A damage criterion can be introduced by requiring that at any time t

$$g(\xi_t, r_t) = \xi_t - r_t \leq 0 \qquad (8.27)$$

Where r_t = the damage threshold (energy barrier) at current time t. If r_0 is the initial damage threshold before any loading is applied, a characteristical property of the material, then $r_t \geq r_0$, Equation (8.27), states that damage in the material is initiated when the damage energy release rate r_t exceeds the initial damage threshold r_0. This condition implies that stress based damage criterion in the presence of significant plastic flow is inherently inadequate for predicting realistic plastic damage growth.

To describe the growth of microcracks and the expansion of damage surface, equations of evolution for $\dot{d}$ and $\dot{r}$ are defined as

$$\dot{d}_t = \lambda \Xi (d_t, \xi_t, s, a) \qquad (8.28)$$
$$\dot{r}_t = \lambda \qquad (8.29)$$

where s and a are the inclusion spacing and sizing, respectively. Ξ is damage evolution function based on experimental results.

Further, the irreversible nature of damage is captured by enforcing that the damage consistency parameter λ satisfy unilateral restrictions:

$$\dot{\lambda} \geq 0 \qquad (8.30)$$

$$g\,(\xi_t, r_t) \leq 0 \qquad (8.31)$$

$$\dot{\lambda}\,(g\,(\xi_t, r_t)) = 0 \qquad (8.32)$$

If $g(\xi_t, r_t) < 0$, the damage criterion is not satisfied and by condition Equation (8.32), we have $\dot{\lambda} = 0$; hence the damage rule, Equation (8.28), implies that $d=0$ and no further damage takes place. If on the other hand $\dot{\lambda} > 0$, then Equation (8.32) implies that $g(\xi_t, r_t) = 0$. In this event the variable λ can be determined by

$$g\,(\xi_t, r_t) = \dot{g}\,(\xi_t, r_t) = 0 \qquad \Rightarrow \dot{\lambda} = \dot{\xi}_t \qquad (8.33)$$

so that r_t is given by the expression as in Equation (8.34). Observing the relationship, it is shown that these conditions are in fact optimal conditions for a principle of maximum damage dissipation.

$$r_t = max\,\{r_0, max\,\xi_s\} \qquad s \in \{-\infty, t\} \qquad (8.34)$$

8.3 Numerical Implementation Results

The general procedure for this numerical implementation is sketched in Figure 8.1. ANSYS Finite Element Program is chosen to implement the material behavior under WJ impact. The displacement based on the material Langrangean coordinate

is input to a program based on Continuum Damage Mechanics to compute the damage scalar.

8.3.1 Mesh Design and Boundary Conditions

The design of a finite element mesh for a wave propagation problem requires a careful investigation. A complicated mesh or larger number of elements will be too expensive for the computer resources. In this study, a four-node linear isoparametric axisymmetric element type is adopted for its simplicity.

In order to optimize the size of material model, a two dimensional 0.1 X 0.125 inch steel plate is defined and 40 X 49 element mesh is constructed.(Figure 8.4). Material simulated is the same as the material used in topography study as 1080 steel. The material properties are listed in Table. 8.1. Material type is set to be non-linear material to accommodate the plasticity. The velocity and displacement of all nodes are set zero at time=0.

Table 8.1. Material properties of Steel 1080

	Density lb/in^3	Young's Modulus psi	Poison Ratio	Yielding Stress psi	Tangent Modulus psi
Steel 1080	0.78	3×10^7	0.3	76000	2.82×10^7

The displacement boundary conditions are assumed that the plate is fixed on the bottom(Equation 8.35). No lateral displacement is defined to simulate a free support work piece. The mesh and the velocity distribution of the jet is constructed and sketched in Figure 8.5 [68].

From the results of stress wave frequency measurement, the frequencies of 3KHz and 2MHz are used. The force boundary conditions are defined as a step function following this results. A sample loading function is presented in Figure

8.6. Since the loading is assumed to be stepwise, multiple iteration nonlinear transient analysis is required to simulate this process. Ten cycles of wave have been simulated.

$$u_i = 0 \qquad v_i = 0 \qquad i \in [2010, 2050] \qquad (Displacement \quad BC) \qquad (8.35)$$

where u and v are displacements in X and Y directions, respectively and i denotes node number.

$$
\left.
\begin{array}{lll}
P^j_1 = 1.632 \times 10^5 & P^j_2 = 4.08 \times 10^4 & j = 20, 21 \\[2mm]
P^j_1 = 1.52 \times 10^5 & P^j_2 = 3.55 \times 10^4 & j = 19, 22 \\[2mm]
P^j_1 = 1.3 \times 10^5 & P^j_2 = 2.61 \times 10^4 & j = 18, 23
\end{array}
\right\} \qquad (8.36)
$$

Where j denotes element number.

ANSYS input program is listed in Appendix A and the displacement of each load step is partially listed in Appendix B. The displacement and the boundary conditions of selected time step are sketched in Figure 8.7 to Figure 8.12.

8.3.2 Continuum Damage Mechanics

Displacement results at each step from ANSYS program are used to calculate the strain energy of each element. The strain energy is then related to the damage variable scalar by using Equation (8.28). The damage evolution function is assumed to be in the Equation (8.37) [65,67]. The summation of the time integral of $\dot{d}$ after each step is the damage scalar at that instant, Equation (8.38). A flow chart of this procedure is shown in Figure 8.13 and program is listed in Appendix C.
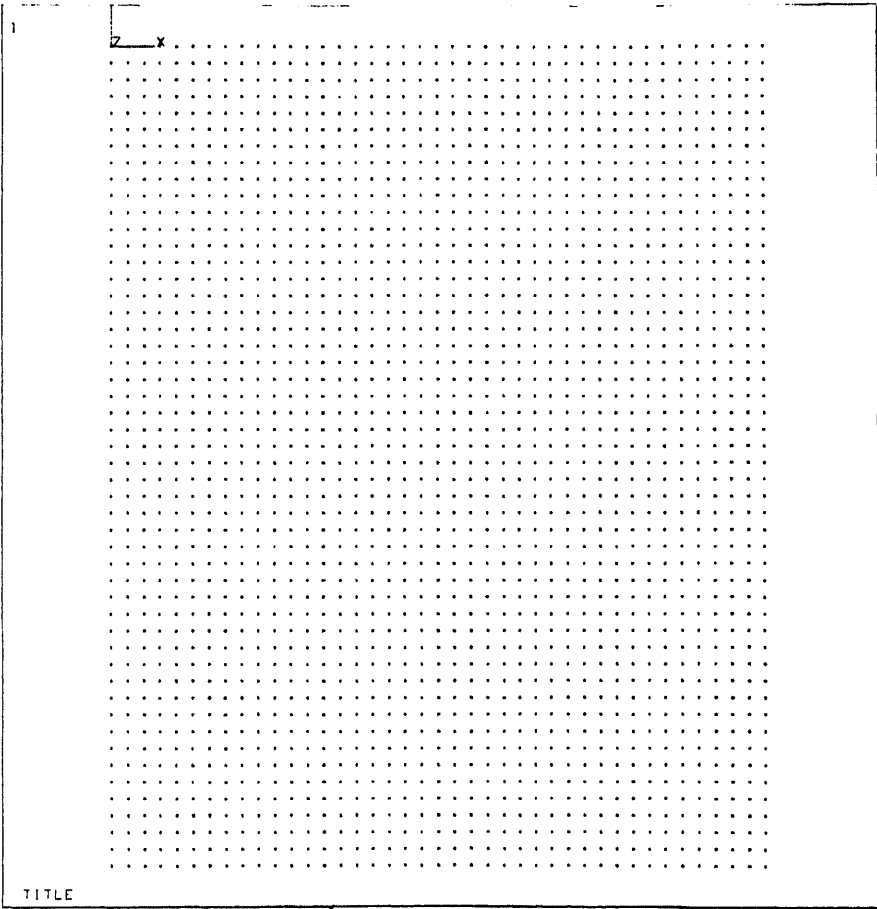
Figure 8.4 Schematic of Material Geometric Model.
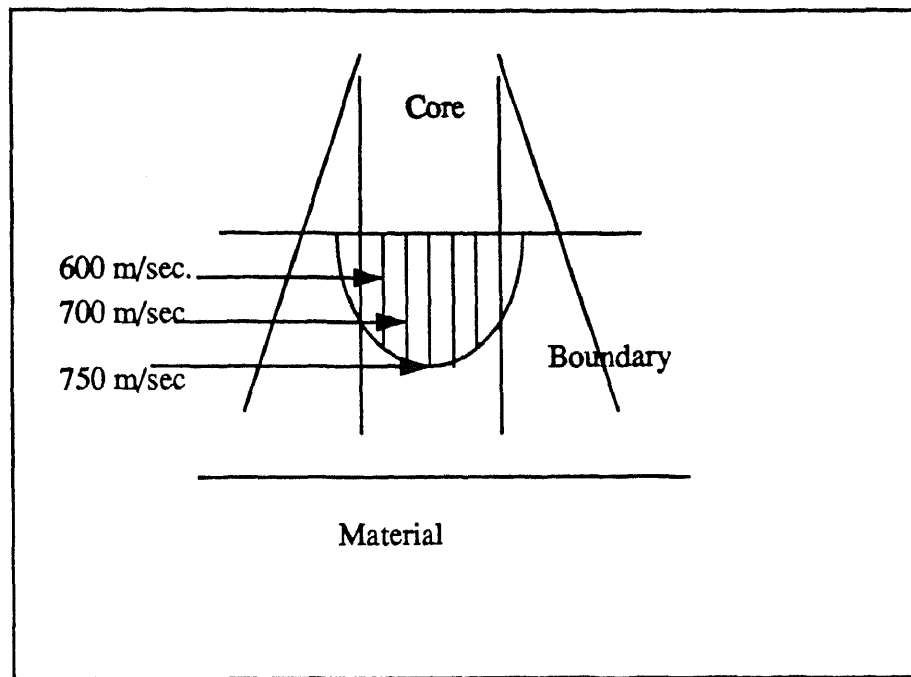
Figure 8.5. Velocity distribution of WJ in radial direction
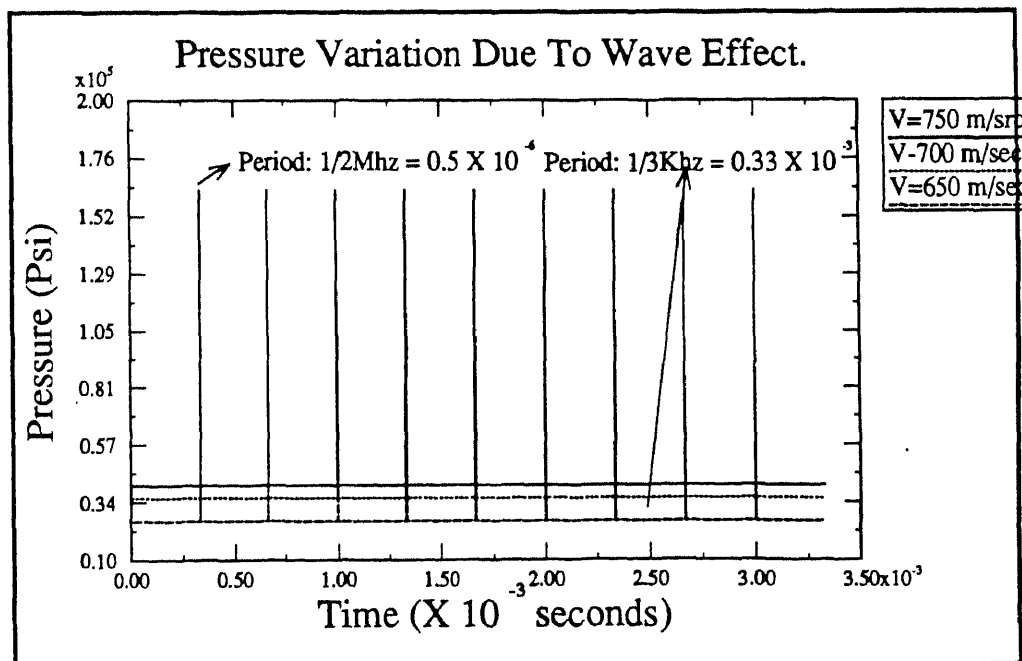
Figure 8.6. Loading function.

$$\Xi = \frac{\xi_0(1-A)}{\xi^2} + AB\,(Exp)^{B\,(\xi_0 - \xi)} \qquad (8.37)$$

where A=0.85, B=4.924 X 10 $^{-7}$ (psi)$^{-1}$, ξ_0= 58 psi.

$$d = \sum_{i=1,n} \dot{d} \qquad (8.38)$$

8.4 Numerical Results and Discussion

To verify this numerical model, the impact of a ten waves, simulating the period of 0.333 X 10^{-3} second jet interaction, is applied on the material model surface. The damage scalar printout of load step at 0.001, 0.002 and 0.003 second is listed in Appendix D. In order to compare the largest damage depth with published result, Figure 8.14, the damage scalar growth of element 20, the axisymmetric element, is listed in Table. 8.2 and the increase trend is shown in Figure 8.15.

Table 8.2. Damage Scalar growth History

Time (10^{-3} Sec.)	0.33	0.66	1	1.33	1.66
Damage Scalar	9.6 X10^{-9}	7.9 X 10 $^{-8}$	3.9 X 10 $^{-7}$	5.8 X 10^{-7}	1.0 X 10 $^{-6}$
Time (10^{-3} Sec.)	2	2.33	2.66	3	3.33
Damage Scalar	2.8 X 10 $^{-6}$	4.3 X 10 $^{-6}$	5.1 X 10 $^{-6}$	6.15X 10^{-6}	6.8 X 10^{-6}

From Equation (8.21), it is reasonable to assume that the square root of the damage scalar is proportional to the element length. Based on this assumption, a linear increase of damage depth is shown in Figure 8.16. The linear increase of the damage depth in conjunction with the maximum loading, which is less than the

yielding stress of material and the ANSYS strain output, it is believed that the material is damaged under elastic fracture.

Further more, an assumption has been made for the interaction time larger than 1 second based on the elastic fracture observation; that is amage scalar is assumed to grow linearly. A linear fitting function has been constructed and the result is shown in Figure 8.17.

It is shown in Figure 8.17, the calculated damage depth is in good correlation with the experimental results in interaction range from 1 second to 5 seconds. Discrepancy is found after 5 seconds interaction. It can be explained as the error from broad exterpolation or the initiation of plastic deformation. Further work can be carried out to analyze deformation from the actual stress wave number loading or to using elastoplastic continuum damage model to compensate the plasticity effect on material.
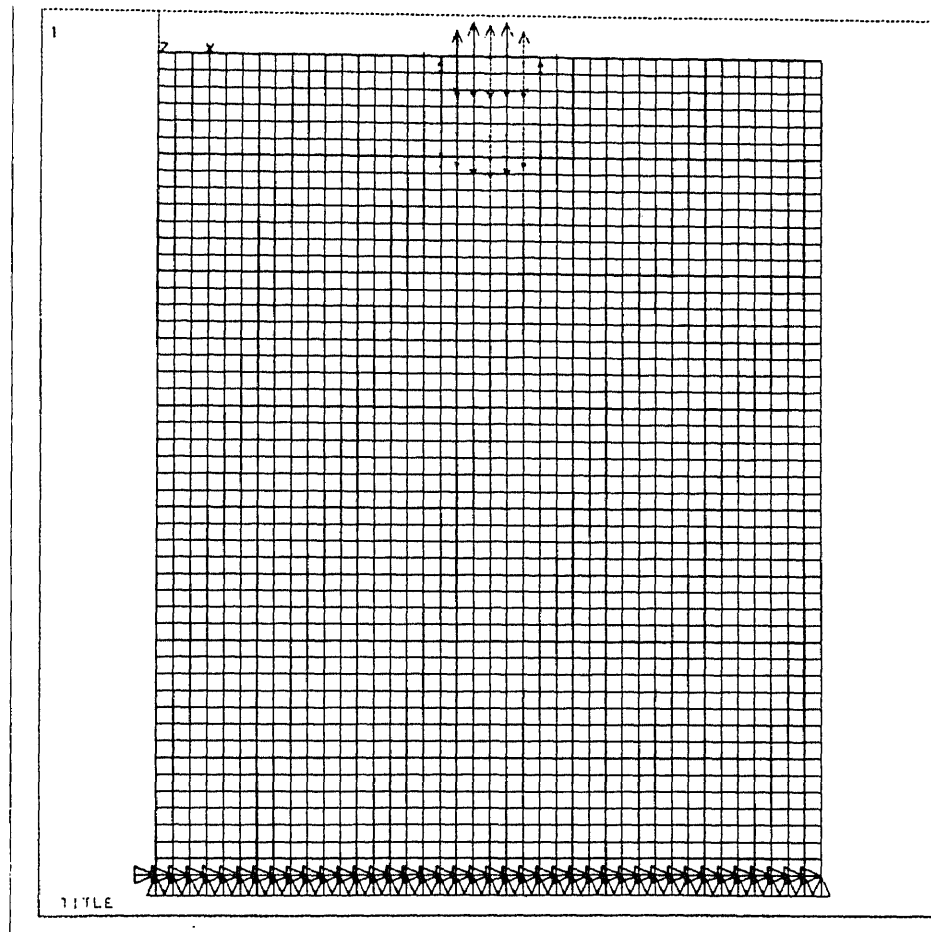
Figure 8.7. Boundary Conditions of Element Mesh at 1 micro-second.
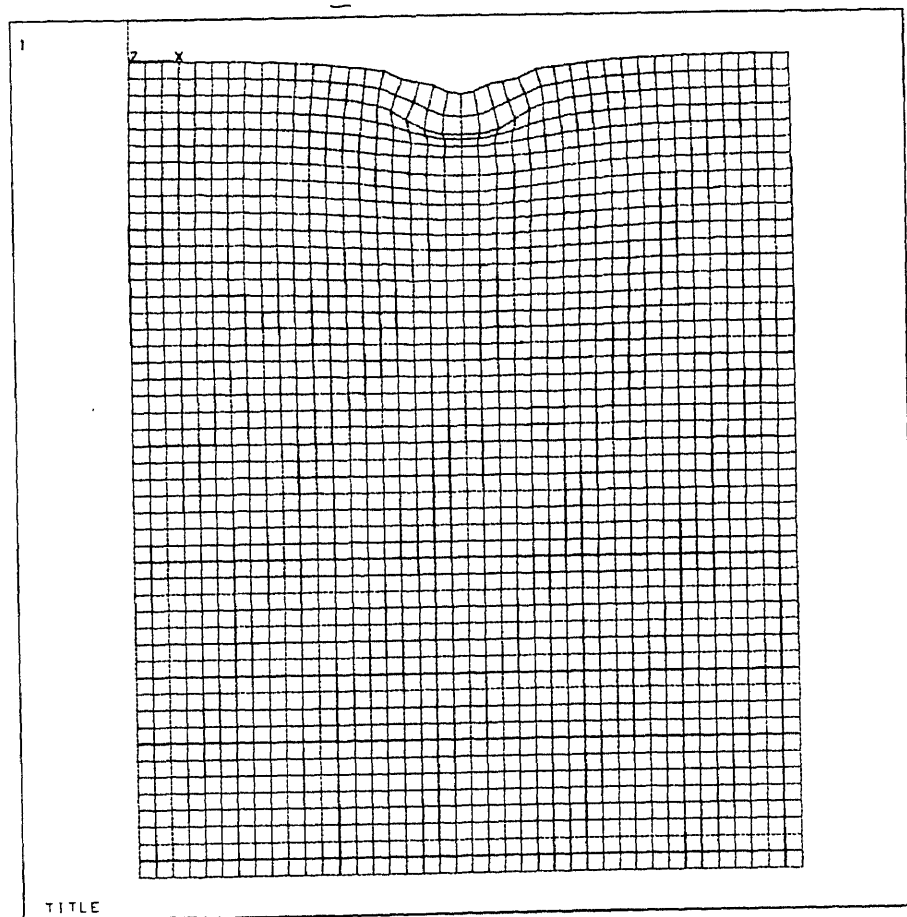
Figure 8.8. Displacement Plot at 1 micro-second.
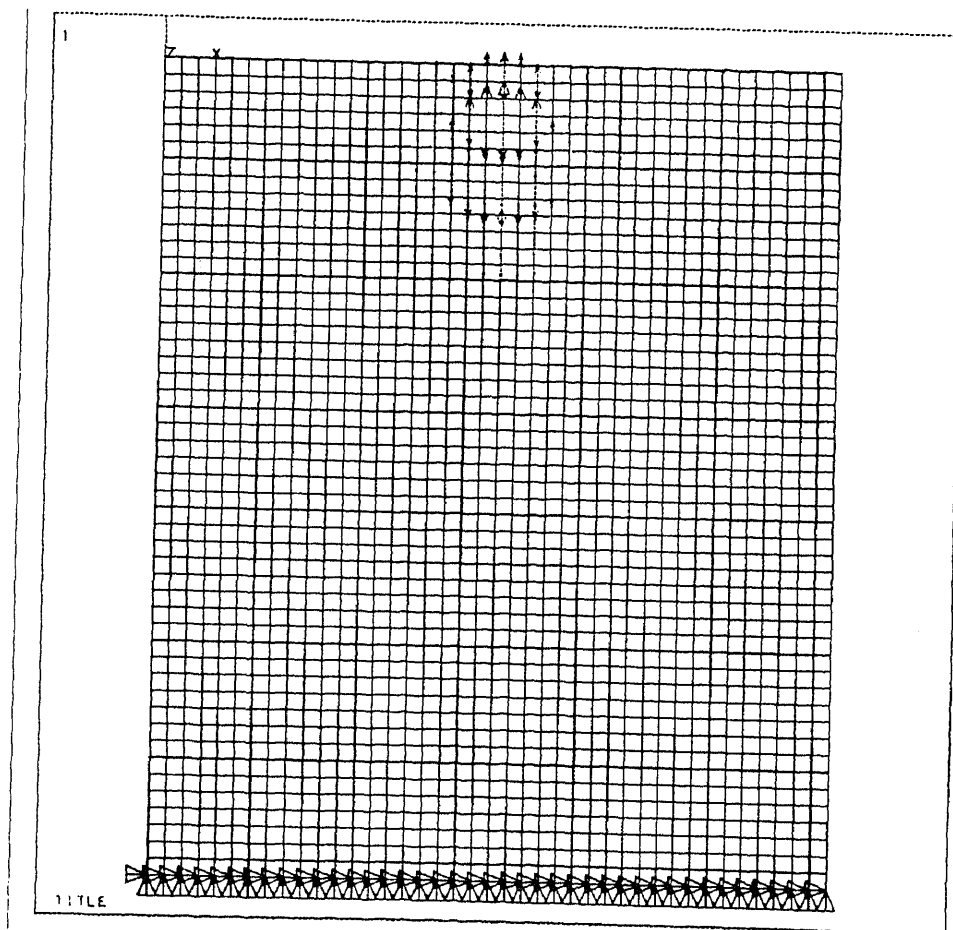
Figure 8.9. Boundary Conditions of Element Mesh at 2 micro-second.
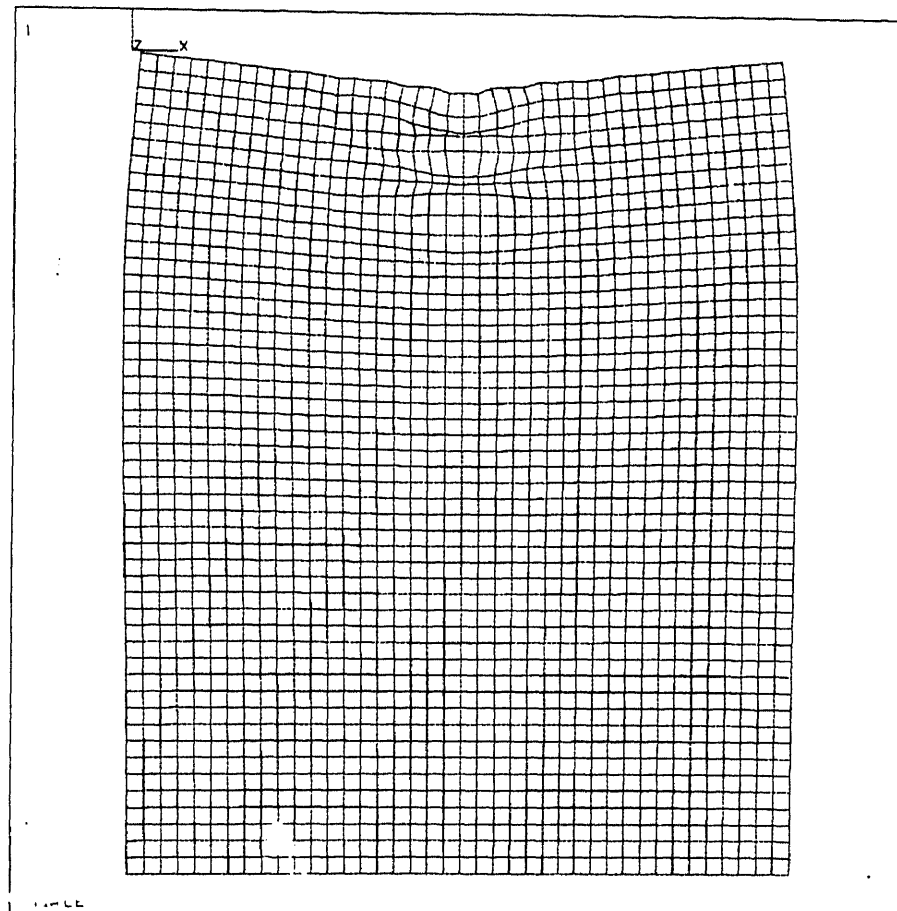
Figure 8.10. Displacement Plot at 2 micro-second.
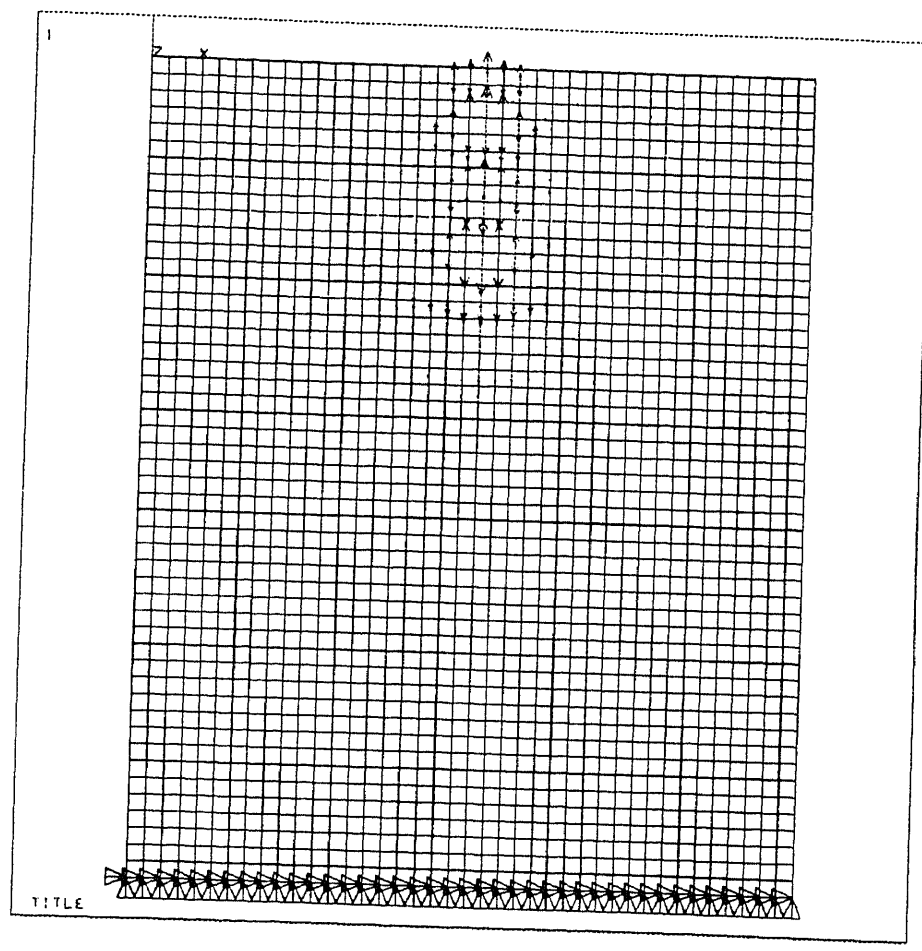
Figure 8.11. Boundary Conditions of Element Mesh at 3 micro-second.
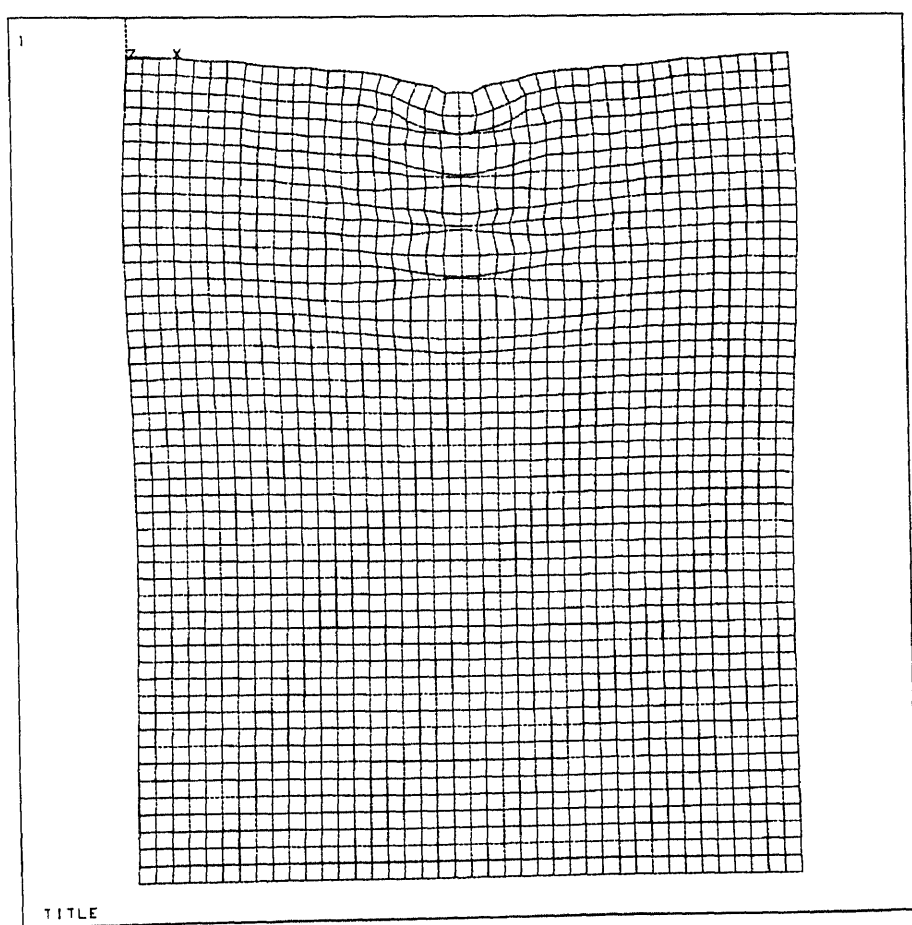
Figure 8.12. Displacement Plot at 3 micro-second.
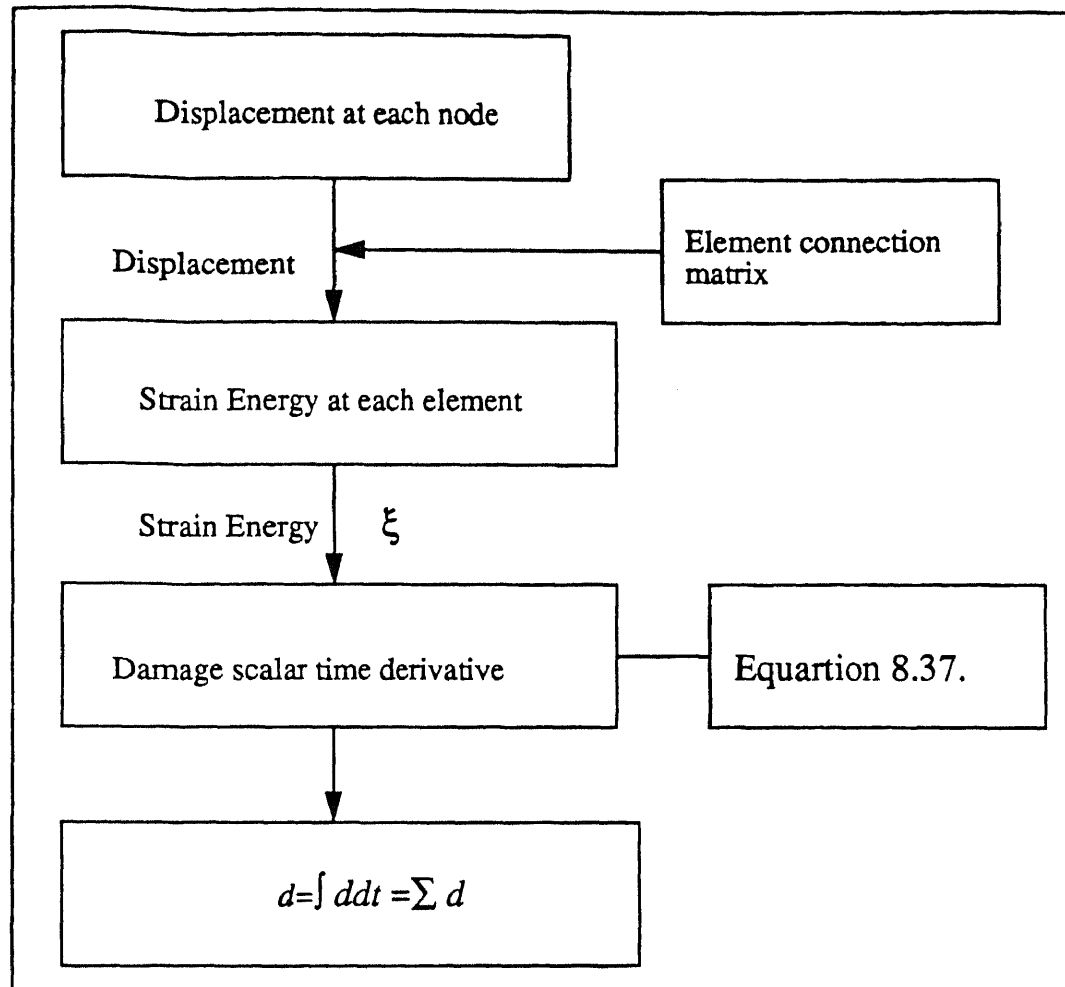
Figure 8.13 Flow Chart of the Implementation of Continuous Damage Model
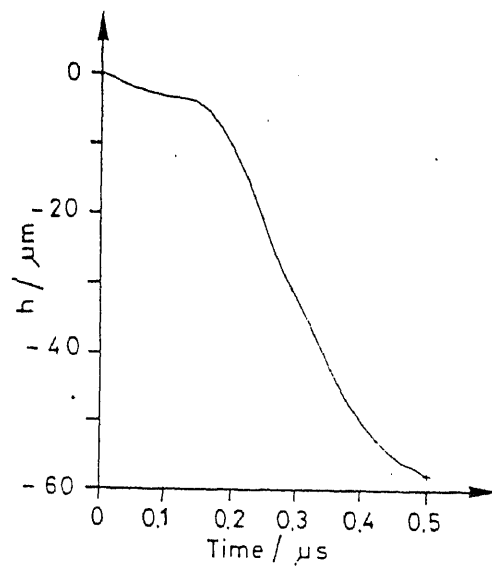
Figure 8.14. Result of Aluminum Plate Impinged by Water Jet [17]
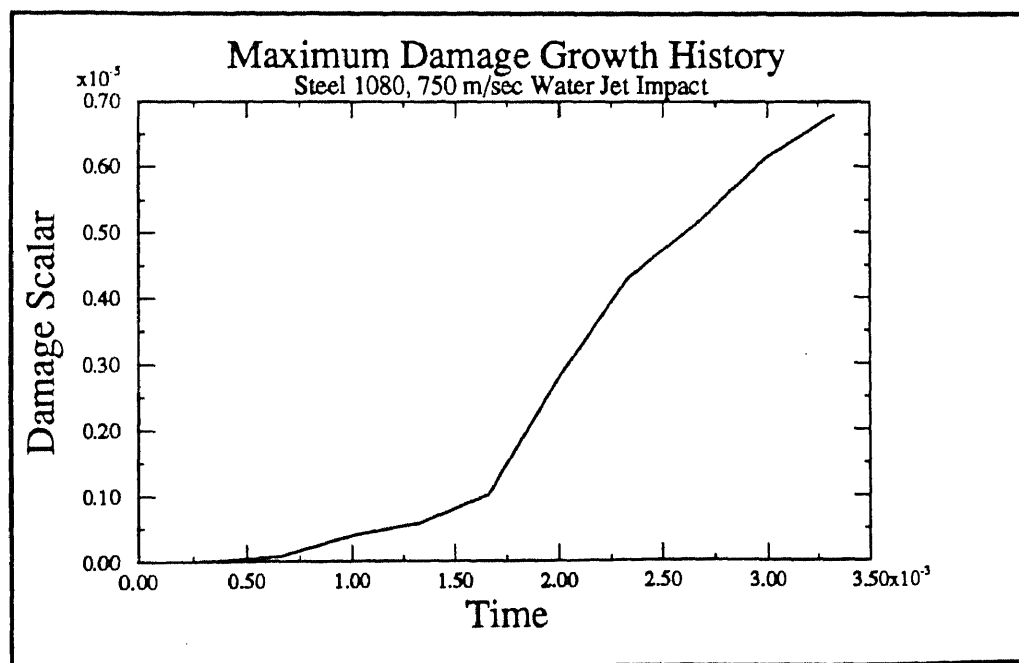
Figure 8.15. Damage scalar growth history in 3 micro-second.
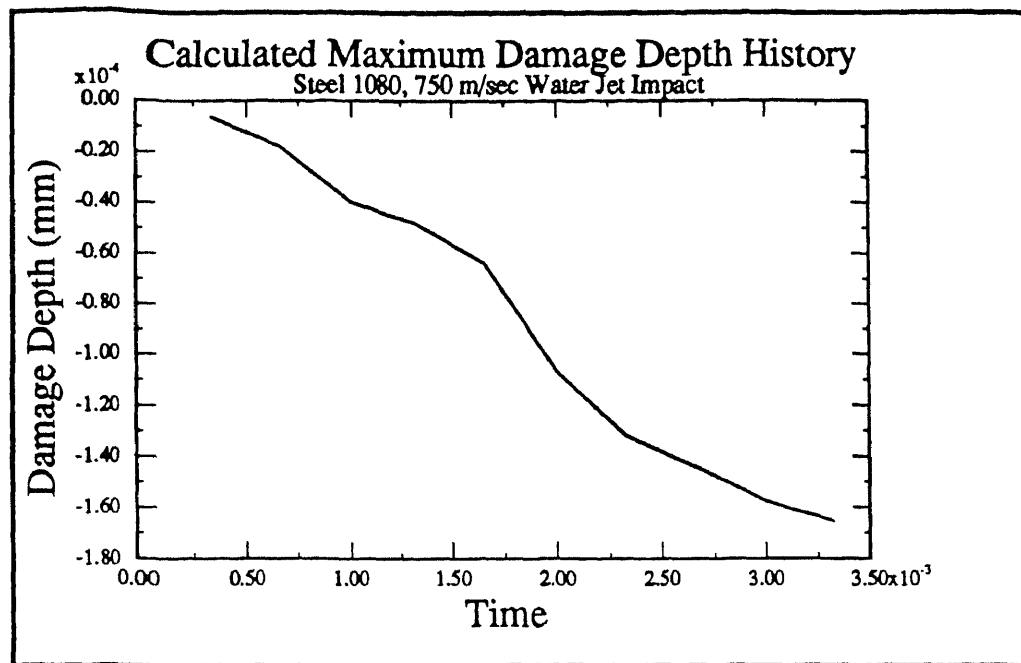
Figure 8.16. Actual damage depth in 3 microsecond.
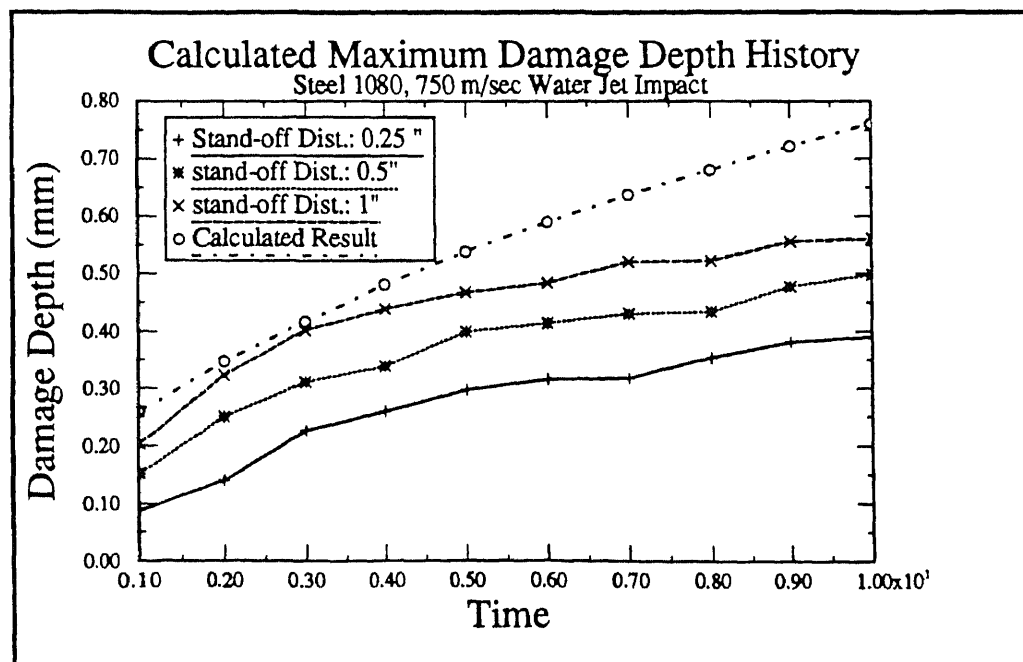
Figure 8.17. Comparison of calculate damage depth and experimental results.

CHAPTER 9

CONCLUSIONS

The objective of this study was to investigate the ductile material response in the course of pure water jet interaction and, hereby, on the basis of cavitation erosion, by means of numerical simulation techniques.

The damage mechanism on ductile material is observed to be the cavitation erosion with material fatigue playing a strong role in making erosion possible. It is also shown that excitation of a bulk, high frequency, (>> 1 MHz), ultrasonic wave in the material is an important part of the fatigue mechanism. This high frequency wave gradually reduces material endurance limit and enhances the fatigue effect. This excitation is produced by the microdroplets and small vapor/air cavities nature of of the impinging waterjet. It is also demonstrated experimentally that making the workpiece resonate to the ultrasonic wave to increase the oscillating stress substantially enhances the cutting rate. This phenomena has been validated and simulated by numerical analysis.

The axisymmetric impingement study of a pure water jet on a ductile material presented in this study can be summarized as followings.

Experimental results in this study reveal the average pressure applied on the ductile material surface is not sufficient to damage material, which identify this damage can not be simulated by solid-solid like penetration. Macrographic picture of material damage surfaces present a constant damage growth. An exceptive phenomenon was observed that the damage depth is affected by the thickness of workpiece. This observation combining with micro-fractographic pictures suggest that the damage mechanism is cavitation-erosion. Stress waves, generated by cavitation and erosion impact loadings, frequency measurement was carried out and a 3 KHz and a 5 MHz excitation was observed.

A numerical model to describe the material damage depth growth was developed

in the frame of Finite Element Method and Continuum Damage Mechanics. Continuum Damage Mechanics is based on the hypothesis that material damage is an irreversible process and can be attributed by the damage energy release rate. Computed results are in good agreement with experimental values.

The information gained in this study enables a better understanding of material destruction process upon waterjet interaction. By this knowledge, the cutting efficiency of waterjet machining can be increased by enhancing the cavitation erosion effect on material surface. The resulting model can also be used to optimize the conditions of jet generation and inprovement of nozzle design, integration of kinetic, chemical, and thermal energies for material shaping, and the use of high speed waterjet.

APPENDIX A

ANSYS Input File List

COM,ANSYS REVISION 4.4 UP437 A 24 12.1161 3/6/1992

SHOW,X11

CORE

/PREP7

ET,1,42

***************BEGIN NODE CONSTRUCTION********************

N,1

N,41,0.1

FILL

NGEN,50,41,1,41,1,,-2.5E-3

**************END NODE CONSTRUCTION**********************

*************BEGIN ELEMENT CONSTRUCTION*****************

E,42,43,2,1

EGEN,40,1,1,1,1

EGEN,49,41,1,40,1

************END ELEMENT CONSTRUCTION*******************

***********BEGIN MATERIAL PROPERTIES DEFINITION*************

DENS,1,0.78

EX,1,3E7

NUXY,1,0.3

NL,1,13,10

NL,1,19,50,60

NL,1,25,76000,76000

NL,1,31,2.82E7,2.82E7

KNL,1

**********END MATERIAL PROPERTIES DEFINITION***************

**********BEGIN BOUNDARY CONDITION********************

D,2010,ALL,0,0,2050,1

EP,20,3,1.632E5,,21,1

EP,19,3,1.52E5,,22,3

EP,18,3,1.3E5,,23,5

EPLIST

TIME,0.5E-7

**********END BOUNDARY CONDITION**************************

ITER,-3

KAN,4

KAY,5,2

KAY,6,1

KAY,8,1

KAY,9,1

KAY,10,1

KBC,1

KSE,1

MPPLOT,PLAS

36 NWRITE

37 EWRITE

38 AFWRITE

3FINISH

***********DEFINE LOAD STEPS******************************

/PREP6

NTABLE,6

NSTEP,38

FILL,1,1,,,5.5E-7

FILL,1,2,,,3.333E-4

FILL,1,3,,,3.338E-4

FILL,1,4,,,3.343E-4

FILL,1,5,,,3.3438E-4

FILL,1,6,,,6.666E-4

FILL,1,7,,,6.66717E-4

FILL,1,8,,,6.67217E-4

FILL,1,9,,,6.67267E-4

FILL,1,10,,,1E-3

FILL,1,11,,,1.00005E-3

FILL,1,12,,,1.00055E-3

FILL,1,13,,,1.0006E-3

FILL,1,14,,,1.3333E-3

FILL,1,15,,,1.33338E-3

FILL,1,16,,,1.33388E-3

FILL,1,17,,,1.33393E-3

FILL,1,18,,,1.6667E-3

FILL,1,19,,,1.66672E-3

FILL,1,20,,,1.66722E-3

FILL,1,21,,,1.66727E-3

FILL,1,22,,,2E-3

FILL,1,23,,,2.00005E-3

FILL,1,24,,,2.00055E-3

FILL,1,25,,,2.00060E-3

FILL,1,26,,,2.33333E-3

FILL,1,27,,,2.33338E-3

FILL,1,28,,,2.33388E-3

FILL,1,29,,,2.33393E-3

FILL,1,30,,,2.66667E-3

FILL,1,31,,,2.66672E-3

FILL,1,32,,,2.66722E-3

FILL,1,33,,,2.66727E-3

FILL,1,34,,,3E-3

FILL,1,35,,,3.00005E-3

FILL,1,36,,,3.00055E-3

FILL,1,37,,,3.00060E-3

FILL,1,38,,,3.33333E-3

FILL,2,1,2,1,4.08E4

FILL,2,3,4,1,1.632E5

FILL,2,5,6,1,4.08E4

FILL,2,7,8,1,1.632E5

FILL,2,9,10,1,4.08E4

FILL,2,11,12,1,1.632E5

FILL,2,13,14,1,4.08E4

FILL,2,15,16,1,1.632E5

FILL,2,17,18,1,4.08E4

FILL,2,19,20,1,1.632E5

FILL,2,21,22,1,4.08E4

FILL,2,23,24,1,1.632E5

FILL,2,25,26,1,4.08E4

FILL,2,27,28,1,1.632E5

FILL,2,29,30,1,4.08E4

FILL,2,31,32,1,1.632E5

FILL,2,33,34,1,4.08E4

FILL,2,35,36,1,1.632E5

FILL,2,37,38,1,4.08E4

FILL,5,1,2,1,3.55E4

FILL,5,3,4,1,1.52E5

FILL,5,5,6,1,3.55E4

FILL,5,7,8,1,1.52E5

FILL,5,9,10,1,3.55E4

FILL,5,11,12,1,1.52E5

FILL,5,13,14,1,3.55E4

FILL,5,15,16,1,1.52E5

FILL,5,17,18,1,3.55E4

FILL,5,19,20,1,1.52E5

FILL,5,21,22,1,3.55E4

```
FILL,5,23,24,1,1.52E5

FILL,5,25,26,1,3.55E4

FILL,5,27,28,1,1.52E5

FILL,5,29,30,1,3.55E4

FILL,5,31,32,1,1.52E5

FILL,5,33,34,1,3.55E4

FILL,5,35,36,1,1.52E5

FILL,5,37,38,1,3.55E4

FILL,6,1,2,1,2.61E4

FILL,6,3,4,1,1.3E5

FILL,6,5,6,1,2.61E4

FILL,6,7,8,1,1.3E5

FILL,6,9,10,1,2.61E4

FILL,6,11,12,1,1.3E5

FILL,6,13,14,1,2.61E4

FILL,6,15,16,1,1.3E5

FILL,6,17,18,1,2.61E4

FILL,6,19,20,1,1.3E5

FILL,6,21,22,1,2.61E4

FILL,6,23,24,1,1.3E5

FILL,6,25,26,1,2.61E4

FILL,6,27,28,1,1.3E5

FILL,6,29,30,1,2.61E4

FILL,6,31,32,1,1.3E5

FILL,6,33,34,1,2.61E4

FILL,6,35,36,1,1.3E5

FILL,6,37,38,1,2.61E4

FILL,3,1,38,1,-3

FILL,4,1,38,1,4

FILL,4,2,38,4,3

LGR1,TIME,1
```

```
LGR1,NITTER,3
LGR1,NPOST,4
EP,20,3,2,,21,1
EP,19,3,5,,22,3
EP,18,3,6,,23,5
LFWRITE
FINISH
*******************END LOAD STEP****************************
/INPUT,27
/INPUT,23
FINISH
/POST1
SET,39,3
FINISH
/EOF
```

APPENDIX B

ANSYS Output FIle

ANSYS - ENGINEERING ANALYSIS SYSTEM REVISION 4.4 A 16 PGH SUPER-COMPUT. MAY 1,1990

ANSYS(R) COPYRIGHT(C) 1971, 1978, 1982, 1983, 1985, 1987, 1989, 1990 SWANSON ANALYSIS SYSTEMS, INC. AS UNPUBLISHED WORK.

PROPRIETARY DATA - UNAUTHORIZED USE, DISTRIBUTION OR DUPLICATION IS PROHIBITED. ALL RIGHTS RESERVED.

FOR SUPPORT CALL PSC HOTLINE PHONE (412) 268-6350 TWX

TITLE 3.7622 APR 19,1992 CP= 1.552

UNIVERSITY VERSION FOR EDUCATIONAL PURPOSES ONLY

***** POST1 NODAL DISPLACEMENT LISTING *****

LOAD STEP 3 ITERATION= 3 SECTION= 1

TIME= 0.33330E-03 LOAD CASE= 1

THE FOLLOWING X,Y,Z DISPLACEMENTS ARE IN GLOBAL COORDINATES

NODE UX UY

1 0.50296397E-05 -0.10451121E-04

2 0.50315780E-05 -0.11462890E-04

3 0.50487992E-05 -0.12460067E-04

4 0.50994335E-05 -0.13450505E-04

5 0.51945983E-05 -0.14457030E-04

6 0.53388766E-05 -0.15506233E-04

7 0.55332161E-05 -0.16625312E-04

8 0.57764836E-05 -0.17842741E-04

9 0.60665110E-05 -0.19189098E-04

10 0.64005634E-05 -0.20699092E-04

11 0.67760118E-05 -0.22413355E-04

12 0.71895138E-05 -0.24385998E-04

13 0.76396314E-05 -0.26679145E-04

14 0.81237876E-05 -0.29416099E-04

15 0.86248609E-05 -0.32682751E-04

16 0.92325524E-05 -0.36876233E-04

17 0.96426642E-05 -0.42738196E-04

18 0.91744636E-05 -0.49119644E-04

19 0.73524153E-05 -0.55556725E-04

20 0.40613744E-05 -0.61017078E-04

21 -0.11476987E-13 -0.62979575E-04

22 -0.40613744E-05 -0.61017078E-04

23 -0.73524153E-05 -0.55556725E-04

24 -0.91744636E-05 -0.49119644E-04

25 -0.96426642E-05 -0.42738196E-04

26 -0.92325524E-05 -0.36876233E-04

27 -0.86248610E-05 -0.32682751E-04

28 -0.81237876E-05 -0.29416099E-04

29 -0.76396315E-05 -0.26679145E-04

30 -0.71895138E-05 -0.24385998E-04

31 -0.67760118E-05 -0.22413355E-04

32 -0.64005635E-05 -0.20699092E-04

33 -0.60665110E-05 -0.19189098E-04

34 -0.57764836E-05 -0.17842741E-04

35 -0.55332162E-05 -0.16625312E-04

36 -0.53388766E-05 -0.15506233E-04

37 -0.51945983E-05 -0.14457030E-04

38 -0.50994335E-05 -0.13450505E-04

39 -0.50487992E-05 -0.12460067E-04

40 -0.50315780E-05 -0.11462890E-04

41 -0.50296397E-05 -0.10451121E-04

42 0.40108378E-05 -0.10456172E-04

43 0.40121649E-05 -0.11469040E-04

44 0.40281414E-05 -0.12458025E-04

45 0.40656330E-05 -0.13437684E-04

46 0.41278640E-05 -0.14432578E-04

47 0.42160095E-05 -0.15470077E-04

48 0.43288419E-05 -0.16578086E-04

49 0.44629983E-05 -0.17785487E-04

50 0.46130193E-05 -0.19123254E-04

51 0.47712620E-05 -0.20626331E-04

52 0.49267334E-05 -0.22336309E-04

53 0.50651432E-05 -0.24306207E-04

54 0.51619642E-05 -0.26605155E-04

55 0.51832031E-05 -0.29340312E-04

56 0.50827028E-05 -0.32649273E-04

57 0.46025307E-05 -0.36851517E-04

58 0.39576965E-05 -0.42625331E-04

59 0.32028740E-05 -0.49160548E-04

60 0.19978873E-05 -0.55717571E-04

61 0.90788418E-06 -0.60927343E-04

62 -0.10740862E-13 -0.62727661E-04

63 -0.90788420E-06 -0.60927343E-04

64 -0.19978873E-05 -0.55717571E-04

65 -0.32028740E-05 -0.49160548E-04

66 -0.39576966E-05 -0.42625331E-04

67 -0.46025307E-05 -0.36851517E-04

68 -0.50827028E-05 -0.32649273E-04

69 -0.51832031E-05 -0.29340312E-04

70 -0.51619642E-05 -0.26605155E-04

71 -0.50651432E-05 -0.24306207E-04

72 -0.49267334E-05 -0.22336309E-04

73 -0.47712621E-05 -0.20626331E-04

74 -0.46130193E-05 -0.19123254E-04

75 -0.44629983E-05 -0.17785487E-04

76 -0.43288419E-05 -0.16578086E-04

77 -0.42160095E-05 -0.15470077E-04

78 -0.41278640E-05 -0.14432578E-04

79 -0.40656330E-05 -0.13437684E-04

80 -0.40281414E-05 -0.12458025E-04

81 -0.40121650E-05 -0.11469040E-04

82 -0.40108378E-05 -0.10456172E-04

83 0.29758686E-05 -0.10481426E-04

84 0.29664137E-05 -0.11496474E-04

85 0.29668242E-05 -0.12475254E-04

86 0.29805447E-05 -0.13444609E-04

87 0.30060340E-05 -0.14430877E-04

88 0.30402998E-05 -0.15461465E-04

89 0.30790746E-05 -0.16564472E-04

90 0.31162918E-05 -0.17768985E-04

91 0.31435843E-05 -0.19106341E-04

92 0.31494954E-05 -0.20611940E-04

93 0.31184405E-05 -0.22328306E-04

94 0.30285276E-05 -0.24308391E-04

95 0.28486448E-05 -0.26625557E-04

96 0.25367239E-05 -0.29375311E-04

97 0.20140755E-05 -0.32722409E-04

98 0.12484534E-05 -0.36907204E-04

99 0.21678219E-06 -0.42116409E-04

100 -0.69486279E-06 -0.48560827E-04

101 -0.90038228E-06 -0.54852507E-04

102 -0.55819637E-06 -0.59108496E-04

103 -0.10616276E-13 -0.60642141E-04

104 0.55819635E-06 -0.59108496E-04

105 0.90038226E-06 -0.54852507E-04

106 0.69486276E-06 -0.48560827E-04

107 -0.21678221E-06 -0.42116409E-04

108 -0.12484534E-05 -0.36907204E-04

109 -0.20140755E-05 -0.32722409E-04

110 -0.25367239E-05 -0.29375311E-04

111 -0.28486448E-05 -0.26625557E-04

112 -0.30285276E-05 -0.24308391E-04

113 -0.31184405E-05 -0.22328306E-04

114 -0.31494955E-05 -0.20611940E-04

115 -0.31435843E-05 -0.19106341E-04

116 -0.31162918E-05 -0.17768985E-04

117 -0.30790746E-05 -0.16564472E-04

118 -0.30402998E-05 -0.15461465E-04

119 -0.30060340E-05 -0.14430877E-04

120 -0.29805447E-05 -0.13444609E-04

121 -0.29668242E-05 -0.12475254E-04

122 -0.29664137E-05 -0.11496474E-04

123 -0.29758686E-05 -0.10481426E-04

124 0.19313102E-05 -0.10544068E-04

125 0.19088977E-05 -0.11551643E-04

126 0.18930188E-05 -0.12516281E-04

127 0.18825936E-05 -0.13472906E-04

128 0.18737297E-05 -0.14450034E-04

129 0.18609315E-05 -0.15475091E-04

130 0.18376915E-05 -0.16575712E-04

131 0.17961671E-05 -0.17780666E-04

132 0.17265604E-05 -0.19121050E-04

133 0.16164055E-05 -0.20632114E-04

134 0.14497997E-05 -0.22355565E-04

135 0.12064399E-05 -0.24343720E-04

136 0.86223636E-06 -0.26662572E-04

137 0.38807631E-06 -0.29403409E-04

138 -0.22808628E-06 -0.32680215E-04

139 -0.95228327E-06 -0.36612375E-04

140 -0.16055590E-05 -0.41214103E-04

141 -0.19280045E-05 -0.46032265E-04

142 -0.17503941E-05 -0.50413661E-04

143 -0.10388314E-05 -0.53563985E-04

144 -0.10519300E-13 -0.54694347E-04

145 0.10388313E-05 -0.53563985E-04

146 0.17503941E-05 -0.50413661E-04

147 0.19280045E-05 -0.46032265E-04

148 0.16055590E-05 -0.41214103E-04

149 0.95228325E-06 -0.36612375E-04

150 0.22808626E-06 -0.32680215E-04

151 -0.38807633E-06 -0.29403409E-04

152 -0.86223638E-06 -0.26662572E-04

153 -0.12064400E-05 -0.24343720E-04

154 -0.14497997E-05 -0.22355565E-04

155 -0.16164055E-05 -0.20632114E-04

156 -0.17265604E-05 -0.19121050E-04

157 -0.17961671E-05 -0.17780666E-04

158 -0.18376915E-05 -0.16575712E-04

159 -0.18609315E-05 -0.15475091E-04

160 -0.18737297E-05 -0.14450034E-04

161 -0.18825937E-05 -0.13472906E-04

162 -0.18930188E-05 -0.12516281E-04

163 -0.19088977E-05 -0.11551643E-04

164 -0.19313102E-05 -0.10544068E-04

165 0.89970449E-06 -0.10652496E-04

166 0.86427254E-06 -0.11635948E-04

167 0.83431300E-06 -0.12579447E-04

168 0.80418438E-06 -0.13519255E-04

169 0.76779932E-06 -0.14484693E-04

170 0.71845586E-06 -0.15502727E-04

171 0.64880124E-06 -0.16600018E-04

172 0.55067135E-06 -0.17804237E-04

173 0.41477842E-06 -0.19145270E-04

174 0.23048202E-06 -0.20656591E-04

175 -0.14170940E-07 -0.22377106E-04

176 -0.33133079E-06 -0.24352859E-04

177 -0.73100517E-06 -0.26639392E-04

178 -0.12116233E-05 -0.29299469E-04

179 -0.17448288E-05 -0.32393095E-04

180 -0.22438216E-05 -0.35930799E-04

181 -0.25612245E-05 -0.39783949E-04

182 -0.25362174E-05 -0.43657799E-04

183 -0.20630715E-05 -0.47045533E-04

184 -0.11638562E-05 -0.49372005E-04

185 -0.10306751E-13 -0.50206929E-04

186 0.11638562E-05 -0.49372005E-04

187 0.20630715E-05 -0.47045533E-04

188 0.25362174E-05 -0.43657799E-04

189 0.25612244E-05 -0.39783949E-04

190 0.22438216E-05 -0.35930799E-04

191 0.17448288E-05 -0.32393095E-04

192 0.12116233E-05 -0.29299469E-04

193 0.73100515E-06 -0.26639392E-04

194 0.33133077E-06 -0.24352859E-04

195 0.14170920E-07 -0.22377106E-04

196 -0.23048204E-06 -0.20656591E-04

197 -0.41477844E-06 -0.19145270E-04

198 -0.55067137E-06 -0.17804237E-04

199 -0.64880126E-06 -0.16600018E-04

200 -0.71845588E-06 -0.15502727E-04

201 -0.76779934E-06 -0.14484693E-04

202 -0.80418440E-06 -0.13519255E-04

203 -0.83431302E-06 -0.12579447E-04

204 -0.86427256E-06 -0.11635948E-04

205 -0.89970451E-06 -0.10652496E-04

206 -0.94697115E-07 -0.10805908E-04

207 -0.14139528E-06 -0.11747670E-04

208 -0.18224144E-06 -0.12660560E-04

209 -0.22647128E-06 -0.13577746E-04

210 -0.28174650E-06 -0.14527167E-04

------------------------------SKIP----------------------------

MAXIMUMS

NODE 25 21

VALUE -0.96426642E-05 -0.62979575E-04

LOAD STEP 7 ITERATION= 3 SECTION= 1

TIME= 0.66660E-03 LOAD CASE= 1

THE FOLLOWING X,Y,Z DISPLACEMENTS ARE IN GLOBAL COORDINATES

NODE UX UY

1 0.30241114E-05 -0.28445707E-04

2 0.30207193E-05 -0.29144812E-04

------------------------------SKIP----------------------------

195 0.10966033E-05 -0.63137792E-05

196 0.69236887E-06 -0.57753910E-05

197 0.98254090E-06 -0.46957007E-05

198 0.17969401E-05 -0.27066944E-05

199 0.18471969E-05 -0.20185178E-05

200 0.18599442E-05 -0.15232960E-05

201 0.22604955E-05 -0.72871263E-06

202 0.25636095E-05 -0.21274875E-06

203 0.25879559E-05 0.25826308E-06

204 0.24345925E-05 0.78604180E-06

205 0.23063015E-05 0.13397568E-05

206 -0.28477238E-05 0.11166251E-05

207 -0.29386238E-05 0.64243297E-06

208 -0.30654418E-05 0.16065551E-06

209 -0.31476955E-05 -0.32447854E-06

210 -0.29846760E-05 -0.75808960E-06

MAXIMUMS

NODE 24 103

VALUE -0.58319963E-05 -0.31430625E-04

***** ROUTINE COMPLETED ***** CP = 8.131

/EOF ENCOUNTERED ON FILE18

***** RUN COMPLETED ***** CP= 8.1361 TIME= 3.7653

Appendix C

Algorithm for Continuous Damage Mechanics

PROGRAM CALC

DOUBLE PRECISION SYSTEM DISP(2050,2),SI(1960)

DIMENSION IC(1960,4),SE(980),DT(1960)

INTPDP = 2 SYSTEM

NOUT = 6

NIA = 12

*******************MATERIAL PROPERTIES***************************

E=3E7

G=1.15E7

RO=0.78

A=0.85

B=4.924E-7

SIO=58

******************READ ELEMENT CONNECTION

MATRIX*****************

OPEN(20,FILE='ELEM.DAT')

DO 2 I=1,1960

READ(20,*)IC(I,1),IC(I,2),IC(I,3),IC(I,4)

CONTINUE

*****************READ DISPLACEMENT DATA***********************

READ(*,*)TIME

DO 3 I=1,1960

READ(*,*)TG,DISP(I,1),DISP(I,2)

CONTINUE

****************CALCULATION*******************************

DO 5 I=1,1960

EPX=(DISP(IC(I,4),1)-DISP(IC(I,3),1))/2.5E-3

EPY=(DISP(IC(I,4),2)-DISP(IC(I,1),2))/2.5E-3

```
RXY=(DISP(IC(I,4),2)-DISP(IC(I,3),2))/2.5E-3+(DISP(IC(I,4),1)-DISP(IC(I,1),1))/2.5E-
3
SE(I)=RO*(0.5*(EPX**2+EPY**2)*E+0.5*G*RXY**2)
SI(I)=SI0*(1-A)/(SE(I)**2)+A*B*EXP((SI0-SE(I))*B)
IF (SI0 .GT. SE(I)) THEN
DT(I)=SI(I)*SI0
ELSE
DT(I)=SI(I)*SE(I)
ENDIF
WRITE(*,*)I,EPX,EPY,RXY
WRITE(*,*)SE(I),SI(I),DT(I)
CONTINUE
STOP
END
```

Appendix D

Damage Scalar Output

Time: 0.001 second

Node	Damage Scalar
1	3.58530E-04
2	3.47691E-04
3	3.63072E-04
4	4.50563E-04
5	6.48070E-04
6	1.00339E-03
7	1.60777E-03
8	2.55942E-03
9	4.20161E-03
10	6.75091E-03
11	9.51870E-03
12	2.27460E-02
13	4.08473E-02
14	2.11722E-02
15	5.99878E-02
16	0.724906
17	0.238220
18	0.228834
19	2.46019
20	0.709158
21	0.312540
22	1.47447
23	1.08778
24	0.256899

25	1.18942
26	0.125795
27	2.47141E-02
28	3.91852E-02
29	3.11431E-02
30	1.24498E-02
31	7.82739E-03
32	5.27794E-03
33	3.10101E-03
34	1.93097E-03
35	1.19468E-03
36	7.50647E-04
37	5.03186E-04
38	3.83493E-04
39	3.51197E-04
40	3.57880E-04
41	3.81183E-04
42	3.66032E-04
43	3.87977E-04
44	4.69385E-04
45	6.39761E-04
46	9.38799E-04
47	1.45585E-03
48	2.27309E-03
49	3.57817E-03
50	6.15445E-03
51	8.08278E-03
52	1.57372E-02
53	3.81190E-02
54	2.61422E-02
55	4.45585E-02

56	0.179738
57	0.481734
58	0.934941
59	0.476899
60	4.13362E-02
61	1.46448E-02
62	0.131818
63	0.667235
64	0.889731
65	0.459219
66	5.54885E-02
67	2.51871E-02
68	4.03230E-02
69	2.06606E-02
70	1.03976E-02
71	7.51721E-03
72	4.43813E-03
73	2.80980E-03
74	1.77885E-03
75	1.13123E-03
76	7.54129E-04
77	5.35488E-04
78	4.26116E-04
79	3.87287E-04
80	3.91239E-04
81	4.13601E-04
82	3.82054E-04
83	3.97063E-04
84	4.68389E-04
85	6.17295E-04
86	8.83051E-04

87	1.32509E-03
88	2.06770E-03
89	3.20863E-03
90	5.18015E-03
91	8.30333E-03
92	1.16133E-02
93	2.50628E-02
94	4.09124E-02
95	5.06991E-02
96	8.07164E-02
97	0.132244
98	0.370655
99	1.66630
100	3.01967
101	2.96734
102	2.93418
103	2.13457
104	0.385613
105	6.59365E-02
106	3.00016E-02
107	3.33963E-02
108	3.32498E-02
109	1.41291E-02
110	9.58510E-03
111	6.33210E-03
112	3.88493E-03
113	2.52100E-03
114	1.61230E-03
115	1.06116E-03
116	7.28323E-04
117	5.36673E-04

118	4.38655E-04
119	4.06156E-04
120	4.28735E-04
121	4.30789E-04
122	3.85139E-04
123	3.92891E-04
124	4.56067E-04
125	5.91002E-04
126	8.31689E-04
127	1.23519E-03
128	1.89210E-03
129	2.94441E-03
130	4.57074E-03
131	7.37626E-03
132	1.08613E-02
133	1.46926E-02
134	2.82740E-02
135	4.56286E-02
136	6.18697E-02
137	6.59314E-02
138	0.131368
139	0.521646
140	1.05823
141	1.11106
142	1.17810
143	0.539074
144	0.132625
145	5.97352E-02
146	3.81149E-02
147	3.63755E-2

------------------------------SKIP----------------------------

Time: 0.002 second

Node	Damage Scalar
1	1.81825E-02
2	1.82185E-02
3	1.83842E-02
4	1.85383E-02
5	2.01076E-02
6	2.10955E-02
7	1.94866E-02
8	2.72146E-02
9	2.56230E-02
10	1.30192E-02
11	4.21775E-02
12	4.96967E-02
13	6.04432E-03
14	1.75838E-02
15	2.96446E-03
16	1.04385E-01
17	4.92578E-02
18	0.118952
19	1.79299
20	0.222578
21	0.447580
22	0.669030
23	0.613399
24	1.03153E-01
25	0.220573
26	1.81669E-02
27	1.13755E-02
28	6.52079E-03
29	3.74770E-02

30	4.38776E-02
31	1.74654E-02
32	2.17048E-02
33	2.83288E-02
34	2.04752E-02
35	2.08735E-02
36	2.08937E-02
37	1.89021E-02
38	1.84824E-02
39	1.83299E-02
40	1.82678E-02
41	1.82704E-02
42	1.83433E-02
43	1.85921E-02
44	1.89259E-02
45	1.99255E-02
46	2.08261E-02
47	2.11782E-02
48	2.60023E-02
49	2.12219E-02
50	1.27664E-02
51	4.18120E-02
52	4.15005E-02
53	3.63243E-03
54	1.84374E-02
55	4.18803E-02
56	4.87314E-02
57	2.53482E-02
58	7.10922E-02
59	4.68924E-02
60	2.03233E-02

61	3.91167E-04
62	4.81570E-02
63	4.04192E-02
64	5.94679E-02
65	4.48605E-02
66	2.02881E-02
67	2.76769E-02
68	8.48599E-03
69	2.67551E-02
70	3.89833E-02
71	1.49362E-02
72	2.26340E-02
73	2.50291E-02
74	2.08098E-02
75	2.13691E-02
76	2.01768E-02
77	1.90903E-02
78	1.87864E-02
79	1.85117E-02
80	1.84757E-02
81	1.81625E-02
82	1.81051E-02
83	1.83231E-02
84	1.87302E-02
85	1.93660E-02
86	2.02967E-02
87	2.09828E-02
88	2.34838E-02
89	2.15841E-02
90	1.37529E-02
91	2.63382E-02

92	4.70252E-02
93	2.01670E-02
94	3.81242E-03
95	2.66699E-02
96	7.10303E-02
97	8.44287E-02
98	0.114705
99	1.28206
100	3.85071
101	5.47553
102	4.08137
103	1.24263
104	0.157699
105	3.73570E-02
106	4.73399E-02
107	8.95227E-03
108	1.11870E-02
109	4.17852E-02
110	2.79858E-02
111	1.48035E-02
112	2.21482E-02
113	2.33542E-02
114	2.03511E-02
115	2.02170E-02
116	1.96074E-02
117	1.88005E-02
118	1.84168E-02
119	1.82431E-02
120	1.83360E-02
121	1.75767E-02
122	1.74256E-02

123	1.75887E-02
124	1.79804E-02
125	1.84327E-02
126	1.93726E-02
127	1.99583E-02
128	2.09925E-02
129	2.20667E-02
130	1.49335E-02
131	1.51228E-02
132	3.64114E-02
133	3.71525E-02
134	2.45092E-02
135	5.77814E-03
136	9.42526E-03
137	2.11669E-02
138	2.50809E-02
139	2.86345E-02
140	2.03460E-02
141	4.03216E-02
142	1.88382E-02
143	2.00063E-02
144	3.26400E-02
145	3.25170E-02
146	7.01351E-03
147	1.98308E-02
148	2.25209E-02
149	4.40083E-02
150	1.70392E-02
151	1.54085E-02
152	2.22664E-02

------------------------------SKIP----------------------------

Time : 0.003 second

Node	Damage Scalar
1	1.13328E-03
2	7.62473E-04
3	1.07056E-03
4	1.83990E-03
5	1.28232E-03
6	1.95576E-04
7	6.65559E-03
8	1.34270E-03
9	9.10329E-04
10	1.14305E-02
11	2.36982E-02
12	3.01943E-02
13	6.86050E-03
14	5.82363E-02
15	4.10417E-02
16	9.98804E-02
17	0.107731
18	0.120276
19	0.759598
20	9.77649E-02
21	0.113601
22	0.253902
23	0.262364
24	0.134078
25	0.165929
26	6.51828E-02
27	7.04350E-02
28	1.07654E-02

29	2.19795E-02
30	3.05461E-02
31	1.84644E-02
32	2.56152E-04
33	2.24379E-03
34	6.24620E-03
35	9.79512E-04
36	1.53134E-03
37	1.14745E-03
38	1.34732E-03
39	7.90465E-04
40	1.01160E-03
41	1.08609E-03
42	7.54697E-04
43	9.39243E-04
44	1.43208E-03
45	6.56549E-04
46	1.51535E-03
47	3.63250E-03
48	1.48759E-04
49	4.61499E-04
50	5.05131E-03
51	1.58092E-02
52	2.86880E-02
53	6.45378E-03
54	6.18725E-02
55	6.63739E-02
56	3.04663E-02
57	3.21770E-02
58	6.36642E-02
59	4.11117E-02

60	8.20109E-03
61	4.04799E-02
62	6.91104E-03
63	5.24836E-02
64	6.64678E-02
65	3.00605E-02
66	2.37872E-02
67	7.00000E-02
68	1.42381E-02
69	2.81420E-02
70	1.84375E-02
71	8.85403E-03
72	5.58788E-04
73	1.46251E-04
74	4.38527E-03
75	1.50731E-03
76	6.05036E-04
77	1.54781E-03
78	9.49830E-04
79	7.57053E-04
80	1.03844E-03
81	1.11625E-03
82	9.68964E-04
83	8.76085E-04
84	1.13489E-03
85	8.64638E-04
86	1.29012E-03
87	2.68959E-03
88	6.61959E-05
89	1.38575E-03
90	7.55590E-03

91	6.85619E-03
92	3.00096E-02
93	2.37936E-02
94	1.25786E-02
95	7.43463E-02
96	6.62833E-02
97	0.137710
98	0.230837
99	1.40737
100	3.49391
101	5.21225
102	3.33907
103	1.61885
104	0.346595
105	2.91682E-02
106	0.120922
107	2.98211E-02
108	1.13531E-02
109	3.23064E-02
110	1.22412E-02
111	8.42813E-03
112	1.06679E-03
113	8.15995E-04
114	2.93014E-03
115	1.34891E-03
116	8.19762E-04
117	1.19600E-03
118	8.19035E-04
119	9.65380E-04
120	1.15630E-03
121	1.21878E-03

BIBLIOGRAPHY

1. Maurer, W.C. "Advanced Drilling Techniques." *Tech. Report No: TR 79-1*. Maurer Eng. Inc., Houston, TX., 1979.

2. Godfrey, Jr. K.A. "Water Jets: Concrete Yes; Tunneling Maybe." *Civil Eng.* May 1987.

3. Martin, J.M. "Using Waterjet as a Cutting Tool." *American Mechanists* April 1980.

4. Lenoard, L. "Water Jet Cutting Article-Advanced Composites." *Advanced Composite* Oct. 1986.

5. Hashish, M. "The Applections of Abrasive Jets to Concrete Cutting." *Proceding of 5th Int. Sym. on Jet Cutting Technology* 1982.

6. Hashish, M. "Steel Cutting with Abrasive Waterjets." *Proceding of 5th Int. Sym. on Jet Cutting Technology* 1982.

7. Yie, G.G. "Cutting Hard Materials with Abrasive Entrained Water Jets." *Proceding of 6th Int. Sym. on Jet Cutting Technology* 1984.

8. Ostby, K. "Robotic Waterjet Cutting." *Proceding of 8th Robots Conference* June 1984.

9. Summers, D.A. "Historical Perspective of Fluid Jet Technique." *Proceding of 10th Int. Sym. on Jet Cutting Technology* 1991.

10. Hood, M. "Mechanicsms of Erosion." *Notes for Short Courses in 4th Water Jet Conference* Aug. 1987.

11. Hashish, M. "Theoretical and Experimental Investigation of Continuous Jet Penetration of Solid." *J. of Eng. for Industry, ASME Trans.* Feb. 1978.

12. Crow, S.C. "The UCLA HydraulicRock Cutting Program: Progress Report I." *UCLA-ENG-7389*, UCLA Nov. 1973.

13. Rehbinder, G. "Erosion Resistance of Rock." *Proc. of 4th Int. Sym. on Jet Cutting Technology* April 1978.

14. Rehbinder, G. "Some Aspects on The Mechanism of Erosion of Rock with A High Speed Water Jet." *Proc. of 3th Int. Sym. on Jet Cutting Technology* May 1976.

15. Erdmann, F. , Louis, H. , and Wiedmeier, J. "Material Behaviour, Material Stressing, Principle Aspects in the Application of High Speed Water Jets." *Proc. of 4th Int. Sym. on Jet Cutting Technology* April 1978.

16. Przyklenk K., and Schlatter, M. "Simulation of The Cutting Process in Water Jetting with Finite Element Method." *Proc. of 8th Int. Sym. on Jet Cutting Technology* Sep. 1986.

17. Curnier, A., and Ridah, S. *"Continuum Mechanics Simulation of The Basic Bubble Cavitation Erosion Process."* LMA-DME-EPFL, Lausanne, 1987.

18. Vijay, M.M., Zou, C., and Tavoularis, S. "Study of The Characteristics of Cavitating Water Jets By Photography and Erosion." *Proc. of 10th Int. Sym. on Jet Cutting Technology* Oct. 1990.

19. Yamaguchi, A., and S. Shimizu "Erosion Due To Impingement Of Cavitating Jet." *J. of Fluid Eng., ASME Trans.* Oct. 1987.

20. Hammit, F.G. *"Cavitation and Multiphase Flow Phenomena."* McGraw-Hill Press, 1980.

21. Holl, J.W. and Treaster, A.L. "Cavitation Hysteresis." *J. of Basic Eng., ASME Trans.* March 1986.

22. *"Metal Handbook Desk Edition."* ASM International, 1991.

23. Engel, P.A. *"Impact Wear of Materials."* Elsevier Press, NY., 1976.

24. Archard, J.F. "Study of Wear Mechanism." *J. of Applied Physics* V. 32 1961.

25 Palmgren, A. *"Ball and Roller Bearing Engineering."* 3rd Edition, SKF Int. Corp., Philadelphia, 1959.

26. Bayer, R.G., and Kuo, T.C. *"Analytical Design for Wear."* Plenum Press, N.Y. 1964.

27. Finnie, I., Walak, J., and Kabil, Y. "Erosion of Metals By Solid Particles." *J. of Materials Science* Sep. 1967.

28. Rao, P.V., and Buckley, D.H. "Effect of Surface Configuration During Solid Particle Impingement Erosion." *J. of Eng. for Gas Turbines and Power* July 1985.

29. Jones, M.H., and Lewis, R. "Solid Particle Erosion of A Selection of Alloy Steel." *Proc. Of 5th Int. Conf. On Erosion By Solid And Liquid Impact* 1979.

30. Bitter, J.G. "A Study Of Erosion Phenomena, Part I." *Wear* V. 6 1963.

31. Bitter, J.G. "A Study Of Erosion Phenomena, Part II." *Wear* V. 6 1963.

32. Christie, D.G., and Hayward, G.W. "Observation of Events Leading To The Formtion Of Water Drops Which Causes Turbine Erosion." *Trans. Phil. Trans. Roy. Soc. of London* V. 260 1966.

33. Smith, D.G., and Kinslow, R. "Pressure Due To High Velocity Impact Of a Water Jet." *Experimental Mechanics* Jan. 1976.

34. Murai, H., and Nishi, S. "Structure Of Water Jet And Erosion Of Material." *Proc. of 5th Americal Water Jet Conference* 1989.

35. Huang, Y.C., Hammit, F.G., and Yang, W.J. "Hydrodynamic Phenomena During High Speed Collision Between Liquid Droplets And Rigid Surface." *J. of Fluid Dynamics, ASME Trans.* June 1973.

36. Heymann, F.J. "High Spped Impact Between A Liquid Droplet And A Solid Surface." *J. of Applied Physics* Dec. 1969.

37. Field, J.E. "Stress Wave, Deformation and Fracture Caused By Liquid Impact." *Trans. Roy. Soc. Of London* 1967.

38. Engle, O.G. "Water Drop Collision With Solid Surface." *J. of Researches of The National Bureau of Standard* V. 54 1955.

39. Erdmann, F., Louis, H. and Wiedemeier, J. "The Action of High Speed Water Jets On Materials. Measurement Methods and The Practicle Application, A Critical Review." *Proc. of 5th Int. Sym. on Jet Cutting Technology* June 1980.

40. Vicker, G.W. and Johnson, W. "Transient Stress Distribution Caused By Water Jet Impact." *J. of Mech. Eng. Sci.* V. 15 1973.

41. Rochester, M.C. and Brunton, J.H. "Surface pressure Distribution During Drop Impingement." *Proc. of 4th Int. Conf. On Erosion By Solid And Liquid Impact* May 1974.

42. Leach, S.J. and Walker, G.L. "The Application of High Pressure Liquid Jets To Cutting." *Phy. Trans. Roc. Soc. Of London* V. 260 1966.

43. Springer, G.S. "Erosion By Liquid Impact." John-Wileyand Sons Press, 1976.

44. Eisenberg, P. "Cavitation and Impact Erosion-Concepts, Correlations, and Controoversies." *ASTM-STP 474* 1970

45. Hammit, F.G., Huang, Y.C., King, C.L., and Mitchell, C.L, "A Stastically Verified Model For Correlating Volume Loss Due To Cavitation or Liquid Impact." *ASTM*

STP 474 1970

46. Pouchot, W.D. "Hydrodynamic Model Of Correlation of Metal Removal Rates From Repetitive Drop Impact." ASTM-STP 474 1970

47. Erdmann, F., and Laschimke, R. "Investigation Into Hydromechanical Stress Caused By An Attack By Drops." Archive of Engineering V. 37 1966.

48. "Metal HandBook, Volume 12, Fractography." 9th Edition ASM International, 1987.

49. Champeney, D.C. "Fourier Transforms and Their Physical Applications." John-Wiley Press, 1985.

50. Cooley, J.W., and Tukey, J.W. "An algorithm for Tthe Machine Calculation of Complex Fourier Series." Math. of Computer V. 19 1965.

51. Thompson, W.T. "Theory of Vibration withj Applications." McGraw Hill, 1978.

52. Moran, B. "A Finite Element Formulation for Transient Analysis of Viscoplastic Solids with Application To Stress Wave Propagation Problems." Computers and Structures V. 27 1987.

53. Timonshenko, S.P. and Goodier, J.N. "Theory of Elasticity." McGraw-Hill, 1970.

54. Fung, Y.C. "Foundation of Solid Mechanics." Prentice Hall, 1965.

55. Bathe, K.J. "Finite Element Problems in Engineering Analysis." Prentice Hall, 1982.

56. Hughes, T.J.R. "The Finite Element Method." Prentice Hall, 1987.

57. Goudreau, G.L., and Hallquist, J.O. "Recent Developments in Large Scale Finite Element Lagrangian Hydrocode Technology." Computer Methods in Applied Mech. and Eng. V. 33 1982.

58. Zukas, J.A., Nicholas, T., and Curran, D.R. "Impact Dynamics." John Wiley Press, 1982.

59. Gurtin, M. "An Introduction to Damage Mechanics." Academic Press, 1981.

60. Kachanov, M.L. "Contiuum Model of Medium with Cracks." J. Engeng. Mech. V. 106.

61. Lemairtre, J. "Evaluation of Dissipation and Damage in Metals." Proc. of Dynamic Loading, I.C.M., 1971.

62. Lechie, F., and Hayhurst, D. "Creep Rupture of Structure." Proc. Roy. Soc. London

V. 240 1974.

63. Lemairtre, J., and Chaboche, J.C. "A Nonlinear Model of Creep Fatigue Damage Cumulation and Interaction." *Proc. IUTAM. Sym. of Mech. of Viscoelastic Media and Bodies* 1974.

64. Lemairtre, J. "How To Use Damage Mechanics." *Nuclear Eng. and Design* V. 80 1984.

65. Ju, J.W. "Energy Based Couples Elastoplastic Damage Models at Finite Strain." *J. of Eng. Mechanics* V. 115 Nov. 1989.

66. Simo, J.C., and Ju, J.W. "Strain and Stress Based Continuum Damage Models I-Formulation." *Int. J. Solid Structure* V. 23 1987.

67. Ju, J.W. "On Energy Based Coupled Elastoplastic Damage Theories: Constitution Modeling and Computational Aspects." *Int. J. Solid Structures* V. 25 1989.

68. Khan, M.E.H. *"Investigation of Dynamics of Abrasive Waterjet."* MS Thesis, NJIT May 1989.